

**ANNALS OF THE UNIVERSITY OF CRAIOVA
ANNALES DE L'UNIVERSITÉ DE CRAIOVA**

**ANALELE
UNIVERSITĂȚII
DIN CRAIOVA**

**SERIA: INGINERIE ELECTRICĂ
SERIE: ELECTRICAL ENGINEERING
SÉRIE: INGÉNIERIE ÉLECTRIQUE**

Anul/Year/Année 44

No. 44, Vol. 44, Issue 1, 2020

December 2020

ISSN 1842 - 4805

EDITURA UNIVERSITARIA

ANNALS OF THE UNIVERSITY OF CRAIOVA



13, A.I. Cuza Str., CRAIOVA 200585
ROMANIA



We exchange publications with similar
institutions of country and from abroad

ANNALES DE L'UNIVERSITÉ DE CRAIOVA

Rue A.I. Cuza, No. 13, CRAIOVA 200585
ROUMANIE

On fait des échanges des publications avec les
institutions similaires du pays et de l'étranger

This journal is published by the Faculty of Electrical Engineering from the University of Craiova.
The authors are fully responsible for the originality of their papers and for accuracy of their notes.

Editorial board

Prof.dr.ing. Ioan POPA editor in chief, University of Craiova, Romania
Conf.dr.ing. Mircea DRIGHICIU - editor in chief, University of Craiova, Romania
Prof.dr.ing. Dan MIHAI, University of Craiova, Romania
Prof.dr.ing. Marian CIONTU, University of Craiova, Romania
Prof.dr.ing. Sergiu IVANOV, University of Craiova, Romania
Prof.dr.ing. Lucian MANDACHE, University of Craiova, Romania
Prof.dr.sc. Ivan YATCHEV, Technical University of Sofia, Bulgaria
Prof.dr.ing. Leszek CZARNECKI, Life Fellow IEEE, Louisiana State University, USA
Prof.dr.ing. Slavoljub ALEKSIC, University of Nic, Serbia
Prof.dr.ing. Sergey RYVKIN, Control Sciences Institute "V.I.Trapeznikov", Russia
Prof.dr.ing. Mihai IORDACHE, University "Politehnica" of Bucharest, Romania
Prof.dr.ing. Victor ŞONTEA, Technical University of Moldova, Moldova
Prof.dr.ing. Iuliu DELEŞEGA, University "Politehnica" of Timişoara, Romania
Prof.dr.ing. Dumitru-Marcel ISTRATE, "Gh. Asachi" Technical University of Iaşi, Romania
Prof.dr.ing. Miroslav PRSA, University of Novisad, Serbia
Prof.dr.ing. Maria BROJBOIU, University of Craiova, Romania
Prof.dr.ing. Mihai GAVRILAŞ, "Gh. Asachi" Technical University of Iaşi, Romania
Prof.dr.ing. Daniela DANCIU, University of Craiova, Romania
Prof.dr.ing. Nicolae MUNTEAN, University "Politehnica" of Timişoara, Romania
Prof.dr.ing. Călin MUNTEANU, Technical University of Cluj-Napoca, Romania
Prof.dr.ing. Leonardo-Geo MĂNESCU, University of Craiova, Romania
Prof.dr.ing. Camelia PETRESCU, "Gh. Asachi" Technical University of Iaşi, Romania
S.I.dr.ing. Ioana Gabriela SÎRBU, University of Craiova, Romania

REVIEWERS COMMITTEE

Lia-Elena ACIU - *Transilvania University of Braşov, Romania*
Maricel ADAM – *"Gh. Asachi" Technical University of Iaşi, Romania*
Mihaela ALBU – *University "Politehnica" of Bucharest, Romania*
Slavoljub ALEKSIC – *University of Nis, Serbia*
Horia BĂLAN – *Technical University of Cluj-Napoca, Romania*
Gheorghe BĂLUȚĂ – *"Gh. Asachi" Technical University of Iaşi, Romania*
Alexandru BITOLEANU – *University of Craiova, Romania*
Maria BROJBOIU – *University of Craiova, Romania*
Emil CAZACU – *University "Politehnica" of Bucharest, Romania*
Aurel CÂMPEANU – *University of Craiova, Romania*
Mihai CERNAT – *Transilvania University of Braşov, Romania*
Marian CIONTU – *University of Craiova, Romania*
Daniel Cristian CISMARU – *University of Craiova, Romania*
Grigore CIVIDJIAN – *University of Craiova, Romania*
Zlata CVETCOVIC – *University of Nis, Serbia*
Leszek CZARNECKI - *Louisiana State University, USA*
Daniela DANCIU – *University of Craiova, Romania*
Sonia DEGERATU – *University of Craiova, Romania*
Iuliu DELEŞEĞA – *University "Politehnica" of Timișoara, Romania*
Silvia-Maria DIGĂ – *University of Craiova, Romania*
Peter DINEFF – *Technical University of Sofia, Bulgaria*
Radu DOBRESCU – *University "Politehnica" of Bucharest, Romania*
Mircea-Adrian DRIGHICIU – *University of Craiova, Romania*
Laurentiu Marius DUMITRAN – *University "Politehnica" of Bucharest, Romania*
Sorin ENACHE – *University of Craiova, Romania*
Virgiliu FIRETEANU – *University "Politehnica" of Bucharest, Romania*
Dan FLORICĂU – *University "Politehnica" of Bucharest, Romania*
Cristian FOŞALĂU – *"Gh. Asachi" Technical University of Iaşi, Romania*
Teodor Lucian GRIGORIE – *Military Technical Academy "Ferdinand I", Romania*
Micea-Dan GUSA – *"Gh. Asachi" Technical University of Iaşi, Romania*
Stefan HĂRĂGUŞ – *University "Politehnica" of Timișoara, Romania*
Elena HELEREA – *Transilvania University of Braşov, Romania*
Eugen HNATIUC – *"Gh. Asachi" Technical University of Iaşi, Romania*
Kemal HOT – *Polytechnic of Zagreb, Croatia*
Eugen IANCU – *University of Craiova, Romania*
Nathan IDA – *University of Akron, USA*
Maria IOANNIDES – *National Technical University of Athens, Greece*
Valentin IONIȚĂ – *University "Politehnica" of Bucharest, Romania*
Mihai IORDACHE – *University "Politehnica" of Bucharest, Romania*
Marcel ISTRATE – *"Gh. Asachi" Technical University of Iaşi, Romania*
Sergiu IVANOV – *University of Craiova, Romania*
Virginia IVANOV – *University of Craiova, Romania*
Wilhelm KAPPEL – *National Research and Development Institute for Electrical Engineering (ICPE – CA) Bucharest, Romania*
Liviu KREINDLER – *University "Politehnica" of Bucharest, Romania*
Gheorghe LIVINȚ – *"Gh. Asachi" Technical University of Iaşi, Romania*
Dumitru Dorin LUCHACHE – *"Gh. Asachi" Technical University of Iaşi, Romania*
Lucian MANDACHE – *University of Craiova, Romania*
Gheorghe MANOLEA – *University of Craiova, Romania*

Andrei MARINESCU – *Romanian Academy of Technical Science, Craiova Branch, Romania*
Iliana MARINOVA – *Technical University of Sofia, Bulgaria*
Claudia MARTIȘ – *Technical University of Cluj-Napoca, Romania*
Ernest MATAGNE – *Université Catholique de Louvain, Belgium*
Leonardo-Geo MĂNESCU – *University of Craiova, Romania*
Dan MIHAI – *University of Craiova, Romania*
Alexandru MOREGA – *University “Politehnica” of Bucharest, Romania*
Mihaela MOREGA – *University “Politehnica” of Bucharest, Romania*
Nazih MOUBAYED – *Lebanese University, Lebanon*
Călin MUNTEANU – *Technical University of Cluj-Napoca, Romania*
Florin MUNTEANU – *"Gh. Asachi" Technical University of Iași, Romania*
Valentin NĂVRĂPESCU – *University “Politehnica” of Bucharest, Romania*
Mitică Iustinian NEACĂ – *University of Craiova, Romania*
Ciprian NEMEȘ – *"Gh. Asachi" Technical University of Iași, Romania*
Petre-Marian NICOLAE – *University of Craiova, Romania*
Dragoș NICULAE - *University “Politehnica” of Bucharest, Romania*
Petru NOTINGHER – *University “Politehnica” of Bucharest, Romania*
Teodor PANĂ – *Technical University of Cluj-Napoca, Romania*
Camelia PETRESCU – *"Gh. Asachi" Technical University of Iași, Romania*
Ioan POPA – *University of Craiova, Romania*
Dan POPESCU – *University of Craiova, Romania*
Daniela POPESCU – *University of Craiova, Romania*
Mihaela POPESCU – *University of Craiova, Romania*
Miroslav PRSA – *University of Novi-Sad, Serbia*
Mircea M. RĂDULESCU – *Technical University of Cluj Napoca, Romania*
Victorița RĂDULESCU - *University “Politehnica” of Bucharest, Romania*
Benoit ROBYNS – *Ecole des Hautes Etude d'Ingénieur de Lille, France*
Constantin ROTARU – *Military Technical Academy "Ferdinand I", Romania*
Alex RUDERMAN – *Elmo Motion Control Ltd, USA*
Sergey RYVKIN – *Trapeznikov Institute of Control Sciences, Russia*
Alexandru SĂLCEANU – *"Gh. Asachi" Technical University of Iași, Romania*
Cristina Gabriela SĂRĂCIN – *University “Politehnica” of Bucharest, Romania*
Constantin SĂRMAȘANU – *"Gh. Asachi" Technical University of Iași, Romania*
Dan SELIȘTEANU – *University of Craiova, Romania*
Victor ȘONTEA – *Technical University of Moldova, Moldova*
Alexandru STANCU – *"A.I. Cuza" University of Iași, Romania*
Viorel STOIAN – *University of Craiova, Romania*
Ryszard STRZELECKI – *University of Technology Gdansk, Poland*
Flavius-Dan ȘURIANU – *University “Politehnica” of Timișoara, Romania*
Lorand SZABO – *Technical University of Cluj-Napoca, Romania*
Radu-Adrian TÎRNOVAN – *Technical University of Cluj-Napoca, Romania*
Raina TZENEVA – *Technical University of Sofia, Bulgaria*
Ioan VADAN – *Technical University of Cluj-Napoca, Romania*
Viorel VARVARA – *"Gh. Asachi" Technical University of Iași, Romania*
Ion VLAD – *University of Craiova, Romania*
Ivan YATCHEV – *Technical University of Sofia, Bulgaria*

CONTENTS

<i>The Use of Helmholtz Coils Designed for 50 Hz at Higher Frequencies</i> – Georgiana Roșu, Ionel Dumbravă, Ion Pătru, Aurelia Scornea, Octavian Baltag, Andrei Marinescu	1
<i>Wireless Remote Control for the Anti-Hail Missiles Launch Ramp Positioning System</i> – Sorin Stepan, Gheorghe Manolea	9
<i>Influence of Synchronized Measurement Errors on the Results of Identification of the Transmission Line Parameters</i> – Murdid Ecaterina, Boris Jingan, Dobrea Ina, Vasilos Elena	14
<i>Metamaterials – Current and Future Trends</i> – Elena Helerea, Lia- Elena Aciu	20
<i>Virtual Instrumentation for Study of Shape Memory Alloys Strip while Bending</i> – Gheorghe-Eugen Subțirelu, Sonia Degeratu	29
<i>Aspects Regarding the Impact of Electrical Vehicles' Charging on Power Quality</i> – Denisa Rușinaru, Gabriel Cosmin Buzatu, Leonardo Geo Mănescu, Claudiu Popirlan	36
<i>'Open Ended' Laboratory to Study the Influence of Unit's Weight on Axle Torque in Railway Traction</i> – Petropol Șerb Gabriela Dana, Petropol Șerb Ion	43
<i>Constructive Dimensions Optimization for Asynchronous Motors used in Coal Mills</i> – Raluca-Cristina Presură (Nicolae), Sorin Enache, Ion Vlad, Marian-Ștefan Nicolae	49
<i>Program for Monitoring Operation Regimes of Low-Power Electrical Machines</i> – Sorin Enache, Ion Vlad, Monica-Adela Enache	55
<i>Contributions Regarding the Monitoring in the Command Center of the Anti-Hail Launch Pads</i> – Sorin Stepan, Gheorghe Manolea	61
<i>Numerical Modeling of Thermal Comfort Parameters in Residential Buildings</i> – Radu-Cristian Dinu, Daniela Popescu, Ioana-Gabriela Sîrbu, Dan-Gabriel Stănescu	65
<i>Studies on the Command of Single-Phase Rectifiers Using the Scalar Control Technique</i> – Florin Alexandru Teodorescu	71

The Use of Helmholtz Coils Designed for 50 Hz at Higher Frequencies

Georgiana Roșu^{*}, Ionel Dumbravă[†], Ion Pătru[†], Aurelia Scornea[†], Octavian Baltag[§], Andrei Marinescu[#]

^{*} Military Technical Academy, George Cosbuc Blv. 39-49, Bucharest 050141, Romania, georgianamarin01@gmail.com

[†] R&D National Institute ICMET Craiova, Decebal Blv. 118A, Craiova 200746, Romania, icmet@icmet.ro

[§] Faculty of Medical Bioengineering – UMF, Iasi, Romania, octavian.baltag@bioinginerie.ro

[#] ASTR, Craiova Branch, 107 Decebal Av., Craiova 200440, Romania, ancor2005@gmail.com

Abstract - Helmholtz coils (HC) are used in order to generate and control uniform magnetic fields for a variety of research applications. They can be easily constructed and their fields can be easily calculated. This makes them especially useful in calibrating magnetic field sensors. Such a calibration system with large Helmholtz coils (1x1m) can be found in ICMET Institute, designed to operate only at a frequency of 50 Hz. There has recently been a request for the calibration of several measuring sensors operating at frequencies up to 10 kHz used in industrial applications such as induction hardening of metal parts. The paper aims to determine the conditions under which this low frequency HC system can be used at frequencies at least 100 times higher. The first part of the paper describes a theoretical analysis on the volume confining the space where the magnetic field components have a predetermined deviation (a 2% threshold) from the center of the HC system followed by a comparison with a 3D FEM simulation and measurement of HC field. The second part describes the identification of the HC parameters at higher frequencies and the resonant methods used to achieve the excitation power required at these frequencies.

Cuvinte cheie: bobine Helmholtz, parametri, sursă rezonantă, model FEM, volum de câmp uniform.

Keywords: Helmholtz coils, parameters, resonant supply, FEM model, uniform field volume.

I. INTRODUCTION

The precise measurement of the magnetic fields generated by electrical and electronic equipment is a requirement imposed by international standards. In some cases, it includes functional measurements; in other cases, there are safety measures imposed for the general public or operators. Periodic calibration of the equipment and sensors for the magnetic field measurement is imposed by the laboratory quality assurance system. However, the cost of such calibration is substantial due to the small number of laboratories accredited for this type of measurements.

Such a calibration system with Helmholtz coils can be found in ICMET Institute, operating at a frequency of 50 Hz and the respective measurement was accredited in 2007 by DKD (Deutscher Kalibrierdienst) [1].

ICMET Institute has recently received several requests for the calibration of certain sensors operating at frequencies up to 10 kHz, needed for example, for magnetic measurements in industrial applications such as induction hardening of metal parts.

The paper aims to answer the question of whether the existing HC system can operate at frequencies at least 100 times higher than 50 Hz and under what conditions.

First the paper presents a theoretical analysis of the HC system which determines the region confined by a predetermined deviation of the magnetic field components related to the magnetic field value in the centre of the Helmholtz system. Also related to the theoretical elements, the paper determines the dependence of the “field uniformity volume” (with predetermined deviation of field values) to the distance between the two coils of the Helmholtz system.

The Helmholtz system analysis [2 - 4] is extended to the use of simulation software based on the finite element method. By implementing the three-dimensional geometric model of the Helmholtz system in the Ansys Maxwell virtual environment, there are obtained the magnetic field values, computed in the space area confined by the rectangular HC system. The dimensions of the field uniformity volume characterising the Helmholtz coils system located at ICMET [5] are determined based on the results of the numerical simulation.

Then the paper describes the HC parameters identification at higher frequencies (self resonance, AC resistance, parasitic capacitance of the coils etc), necessary to obtain an equivalent diagram of HC system. The circuit simulation with LT Spice software confirms the possibility of using the existing HC system at high frequencies below the resonant frequency of the system. The power supply of the system is presented in a series resonance circuit and the simulation of this circuit is compared with the experimental results.

II. THEORETICAL ASPECTS OF HELMHOLTZ SYSTEMS

In order to determine the magnetic field generated by the Helmholtz system, the contributions of the eight current segments constituting the sides of the two coils composing the HC model were considered. The well-known conditions for gradient annulment in the system’s geometric centre were imposed, to achieve the uniformity condition. The following parameters were taken into account: the coils sides are considered segments of length a , carrying an electric current of intensity I , and the coils located at distance $d/2$. Thus, the following relationship is obtained for determining the magnetic field induction generated by one coil [6 - 8]:

$$B(z) = \frac{2\mu_0}{\pi} I a^2 \left(\frac{1}{\sqrt{a^2 + (z-d/2)^2} \sqrt{2a^2 + (z-d/2)^2}} + \frac{1}{\sqrt{a^2 + (z+d/2)^2} \sqrt{2a^2 + (z+d/2)^2}} \right) \quad (1)$$

For the considered Helmholtz system, the length of the coil side is $a = 1$ m. In order to calculate the deviation of the magnetic flux density from the geometric centre on the $-z \dots 0 \dots +z$ axis of the coordinate system, an electric current $I = 1$ A was considered and the magnetic induction results in a dependence on just two parameters z and d :

$$B(z, d) = \frac{2\mu_0}{\pi} F(z, d) \quad (2)$$

Fig. 1 shows the plotting the above mentioned function, which determines the relative deviation of the magnetic flux density values $B(z, d)$, considering as standard value the magnetic induction B_H in the geometric centre of a system fulfilling the Helmholtz condition for square coils:

$$\frac{d}{2} = 0.5445a \quad (3)$$

$$\Delta B = \frac{B_H - B(z, d)}{B_H} = \frac{F_H - F(z, d)}{F_H} = 1 - \frac{F(z, d)}{F_H} \quad (4)$$

Fig. 2 illustrates the deviation of the $F(z, d)$ function compared to its value in the geometric centre $z = 0$, considering the distance $d/2$ as function parameter:

$$F(z, d) - F(z = 0, d) \quad (5)$$

These representations are useful when a particular workspace is concerned, considering a pre-set deviation value in the magnetic field relative to its central value.

Fig. 3 illustrates a detailed view of the previous representation. It is obvious that for smaller distances between the two HC, the magnetic field representation displays a bulge, whereas for larger distances between coils – there are two bulges, indicating larger field gradients. Also, it is noted that the highest precision is achieved while fulfilling the Helmholtz condition – the distance between coils being 0.5445 times the coil side 1 m which corresponds to the HC system analyzed in the paper.

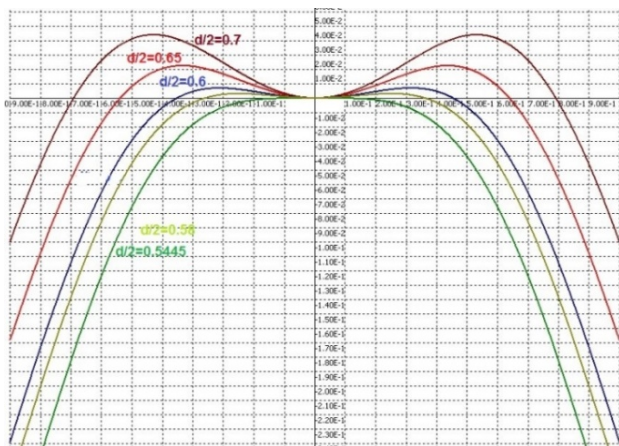


Fig. 1. The magnetic field deviation relative to its value in the geometric center for the Helmholtz coils system.

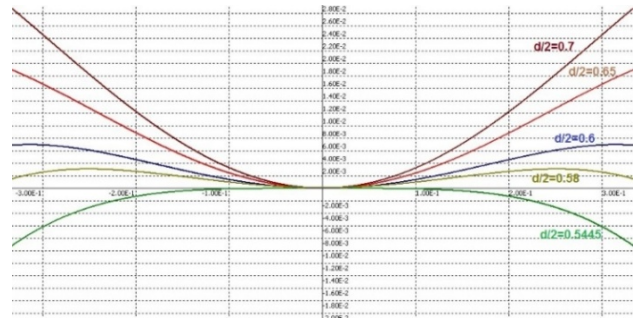


Fig. 2. Deviation of the $F(z, d)$ function relative to its value in the geometric center.

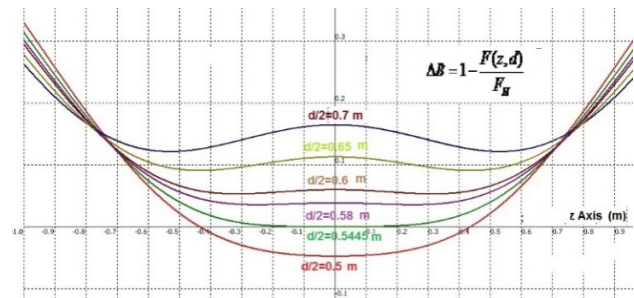


Fig. 3. Detailed view of the deviation of the $F(z, d)$ function relative to its value in the geometric center.

Therefore, as illustrated in the detailed view in Fig. 3, the longitudinal distance for which the field uniformity is achieved is approximately 200 mm, for the Helmholtz condition.

III. NUMERICAL SIMULATION RESULTS

The Helmholtz system analysis is extended to the use of simulation software based on the finite element method [9 - 12]. The geometric model of the HC system was implemented in the virtual environment, each coil being comprised of a single turn. The system geometry is illustrated in Fig. 4 where the coil side is $a = 1$ m, and the distance between coils is 0.5445 m. The coils are marked in purple, and the current excitation – entering and exiting the coils, is marked with red arrows.

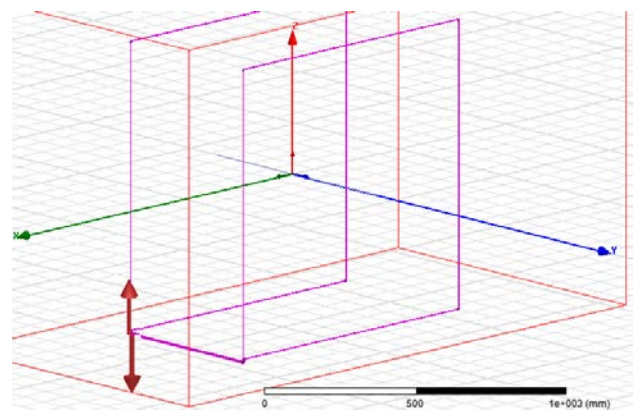


Fig. 4. Geometry of the Helmholtz rectangular coil system.

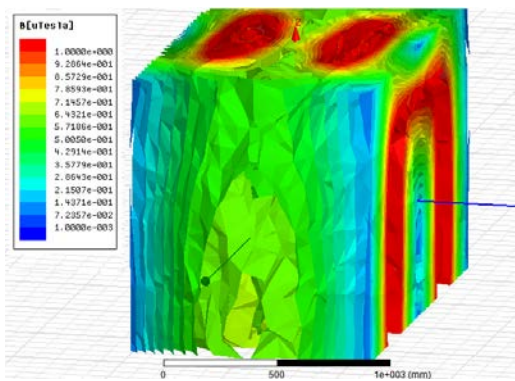


Fig. 5. The magnetic induction generated by the Helmholtz system in the analyzed region.

In order to minimize the impact on the field uniformity of the wire connecting the two rectangular coils, two parallel wires are drawn – one wire connecting the coils and the other returning wire, at a distance of 5 mm.

This small distance between the wires causes a variation between the tangential components of the magnetic field generated by the electric current passing through the wires in opposite directions, which further determines a lower vertical dimension of the volume of the field uniformity [13].

The analysed region is delimited by a rectangular box surrounding the coils. Fig. 5 shows the magnetic field generated by the pair of rectangular coils in Helmholtz configuration carrying an electric current $I = 1$ A. The electric current excitation is applied at the edges of the coil pair, located on the left side of the system, as detailed in Fig. 4.

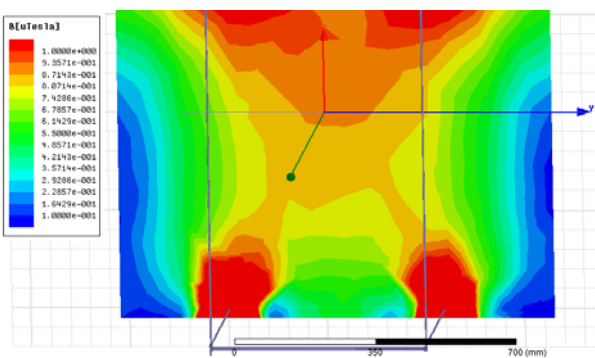


Fig. 6. The longitudinal plane section of the HC field domain.

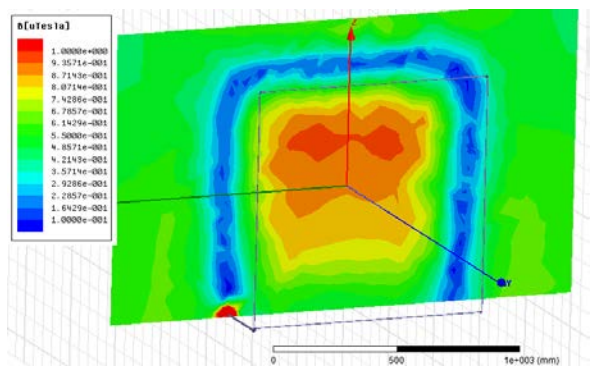


Fig. 7. The transversal plane section of the HC field domain.

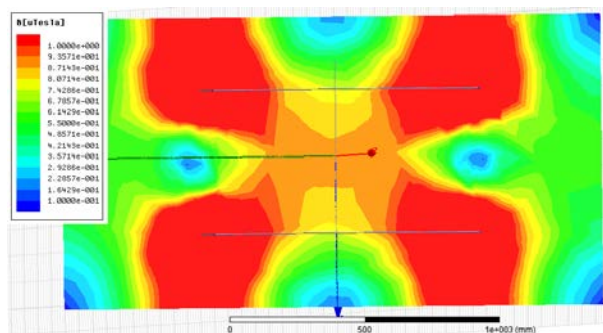


Fig. 8. The horizontal plane section of the HC field domain.

In order to obtain a better view of the magnetic field distribution in the analysed region, and to determine the uniformity region, Figs. 6 - 8, show sections of the region in the longitudinal plane (on the axis of the coils), the transversal plane and the horizontal plane, respectively.

Since the area of interest is located on the axis of the coils – passing through the center of the two coils, the magnetic induction is computed on the above mentioned axis. Fig. 9 illustrates such a representation. Thus, a zone of field uniformity around 200 mm is achieved on the longitudinal axis, corresponding to the theoretical calculations.

By extending the view and achieving better accuracy in expressing the field uniformity, the region of interest is the one determined by the uniform magnetic field relative to the field value in the geometric centre of the HC system.

The normalized difference of the magnetic induction values relative to the standard value of the magnetic induction in the geometric centre is computed, in order to determine the respective region [14, 15].

The deviation of the magnetic field relative to the value in the centre of the HC system (also considered as the centre of the coordinate system) is determined based on the magnetic field values obtained in Figs. 6 - 8. The magnetic field in the centre of the HC system is $B_0 = 0.888 \mu\text{T}$.

The relative deviation is computed with relationship:

$$B_{rel}(x, y, z) = \frac{|B(x, y, z) - B_0(0,0,0)|}{B_0(0,0,0)} * 100 [\%] \quad (6)$$

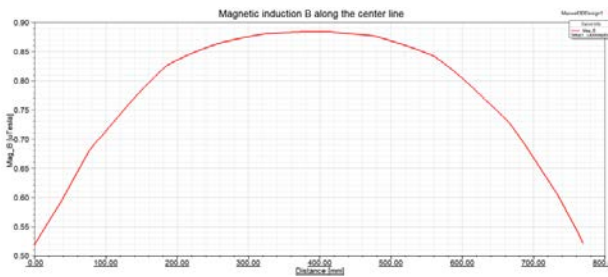


Fig. 9. The magnetic induction computed along the centerline of the Helmholtz system.

The purpose is to determine the region where the magnetic field deviation relative to the centre value is less than 2%. In order to obtain a better view of the field distribution in the analysed region, and to determine the uniform field region, Figs. 10 - 12 show sections of the region in

the longitudinal plane (on the coil pair axis), in the transversal plane and in the horizontal plane, respectively.

Therefore, the illustrations describe the space defined by field uniformity – a deviation less than 2 % relative to the centre field value. As noticed in Fig. 10, on the longitudinal axis (OY), field uniformity is obtained on a distance of 180 mm, slightly shorter than the distance of uniformity of 200 mm obtained based on the analytical calculations and illustrated in Fig. 3.

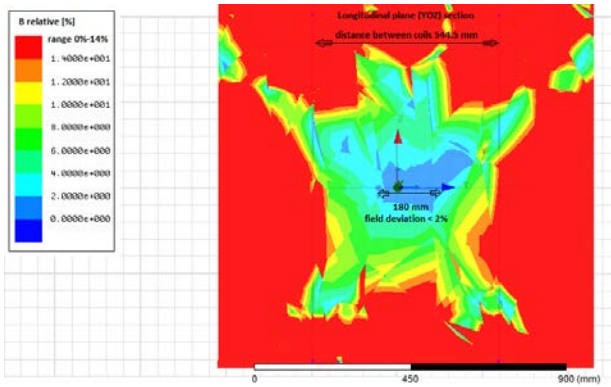


Fig. 10. Field uniformity in the longitudinal plane HC section.

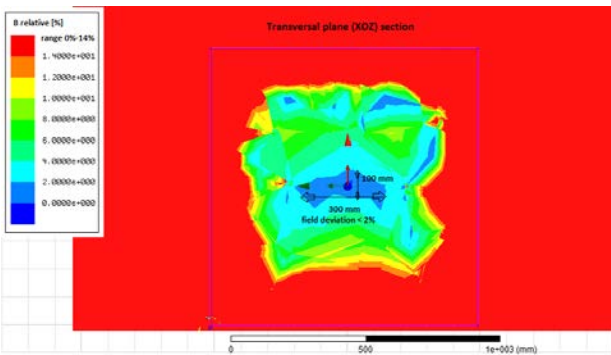


Fig. 11. Field uniformity in the transversal plane HC section.

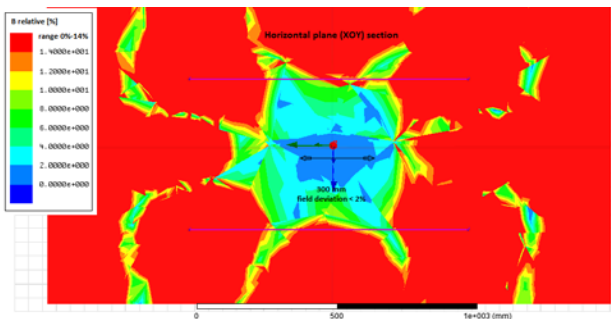


Fig. 12. Field uniformity in the horizontal plane HC section.

TABLE I.
FIELD UNIFORMITY VOLUMES

Field deviation percentage	Uniform field volume dimensions OX , OY , OZ
1 %	260 mm x 150 mm x 80 mm
2 %	300 mm x 180 mm x 100 mm
5 %	600 mm x 340 mm x 280 mm

Table 1 comprises the dimensions of the uniform field volume for several threshold levels for field deviation to the centre: 1 %, 2 %, and 5 %, respectively.

It is worth mentioning that the simulation model comprised of 1 turn per each coil of the HC system has an inductance of 7.9941 μH , as computed by the Maxwell software.

IV. ANALYSIS OF HC SYSTEM

The construction and installation of the HC system with rectangular geometry (Fig. 13), designed initially for the calibration of industrial magnetic probes at frequencies of only 50 Hz, was very convenient. A rectangular HC system generates a volume of nearly uniform magnetic field greater than a circular HC of comparable dimensions [2]. The performance is maintained up to a certain frequency limit. The frequency limitation is a function of the coil's parameters (wire size and type-solid or litz wire-, number of turns and layers), type of connection (series or parallel) of the two coils and finally the supply configuration (balanced or unbalanced with respect to ground).

A Vector Network Analyzer (VNA) device was used for the identification of all circuit parameters (Fig. 14) by impedance and frequency characteristics measurements [16]. The parasitic capacitance C_p is determined from the first resonance frequency of the coils system. Table 2 contains L , C_p , f_r values, and Table 3 contains the AC resistance of the coils for different frequencies. The significant increase of AC resistance is the result of skin and proximity effects in the original solid wire multilayer coils.

The frequency characteristic of the HC is illustrated in Fig. 15. The resonant frequency is $f_r = 15.6$ kHz, which shows that the maximum working frequency of the HC calibration system must be less than the 10 kHz until the system remains inductive.

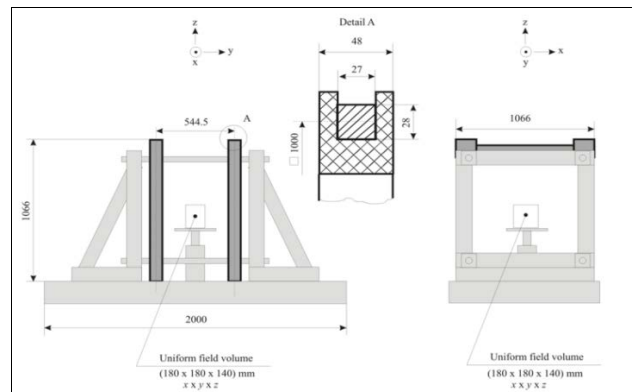


Fig. 13. Design of the Helmholtz coil system.



Fig. 14. HC equivalent circuit.

TABLE II.
MEASURED PARAMETERS OF THE HC SYSTEM.

Parameter	Value
f_r	15.6 kHz
L	2 x 77 mH/coil
C_p	0.675

TABLE III.
AC RESISTANCE AND QUALITY FACTOR
DEPENDING ON THE FREQUENCY.

Frequency (Hz)	Rac (Ω)	Q
50.44	4.15	5.85
502.95	4.85	50.01
994.13	7.37	65.15
5014	55	44.08

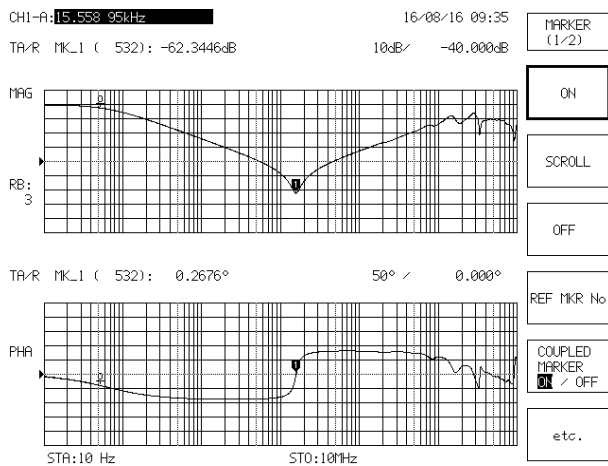


Fig. 15. Frequency characteristic of HC system.

In order to compare the FEM data with the experimental data, it is necessary to perform a review of the HC model in Maxwell software. As specified above, the total inductance of the HC system determined by Maxwell software is 7.9941 μ H; dividing it by 2, we get the inductance per turn of approximately 4 μ H. The total number of turns of the actual HC system is 276, meaning there are approximately 138 turns per each coil. By multiplying the inductance of one coil in the Maxwell model by squared number of turns ($N = 138$), we get a total inductance per coil of approximately $L = 76$ mH, which is close to the experimentally determined value of 77 mH.

V. THE DRIVE OF THE HIGH FREQUENCY HELMHOLTZ COILS USING THE RESONANCE TECHNIQUE

The direct drive is used only for 50 Hz. In order to obtain the extension of the frequency range in which this large HC system is operating, the resonance method is used, which is advantageous at higher frequencies in order to obtain the lowest driving power [5].

Basically, series, parallel or series-parallel resonance can be used, with both series and parallel connection of HC coils. Fig. 16 describes all possible configurations that can be used to achieve resonance at higher frequencies. The choice of one or the other depends on the parameters of the HC system.

Next, some of these configurations are simulated in the LT Spice software to determine the resonance frequency and the current passing through the HC which corresponds to that frequency.

The electrical parameters of the HC electrical circuit are the ones determined experimentally, and the HC equivalent circuit at high frequency (Fig. 14) was used.

Figs. 17 and 18 represent two examples of the HC system modeling by the resonance technique. The electrical circuits are illustrated in the top left side, and the other sides illustrate the current passing through the source (and through the series connected capacitor) I_{C_s} , the current passing through the inductance I_{L_1} , and the one through the equivalent parasitic capacitance I_{C_p} , respectively. The maximum coil current at 500 Hz and 5 kHz, respectively is noted for both circuits.

The advantage of series connection for HC coils is that they are crossed by the same current.

A different C_s capacitor connected in series with the HC equivalent circuit was used in order to achieve the desired resonance frequency.

Another result of the simulations is the calculation of the rated power of the used amplifier at different resonant frequencies: e.g. 15 W at 500 Hz and only 5 W at 5 kHz (depending on the magnetic induction required in the calibration process). Thus a 25 W power amplifier fully covers the needs for the usual calibrations made with this HC system.

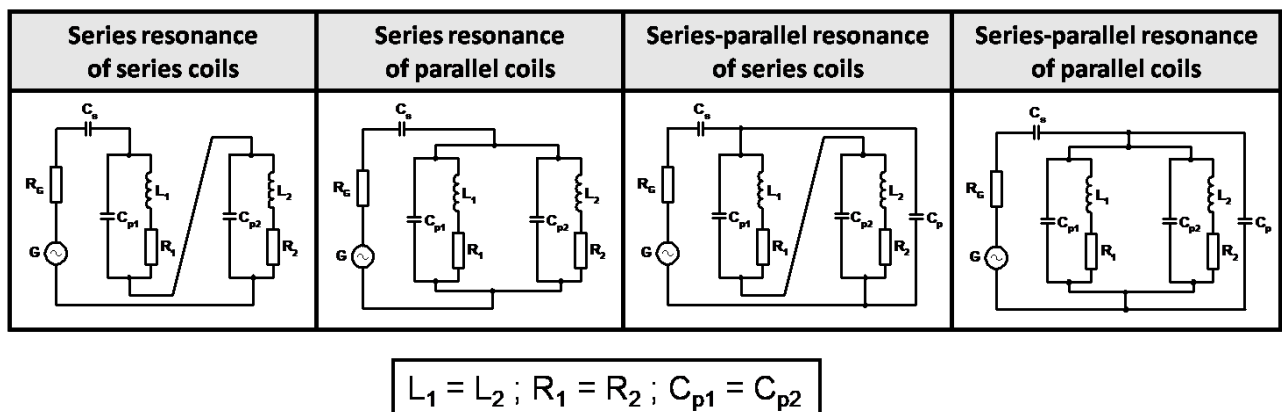


Fig. 16. Resonant configuration to supply HC Coils.

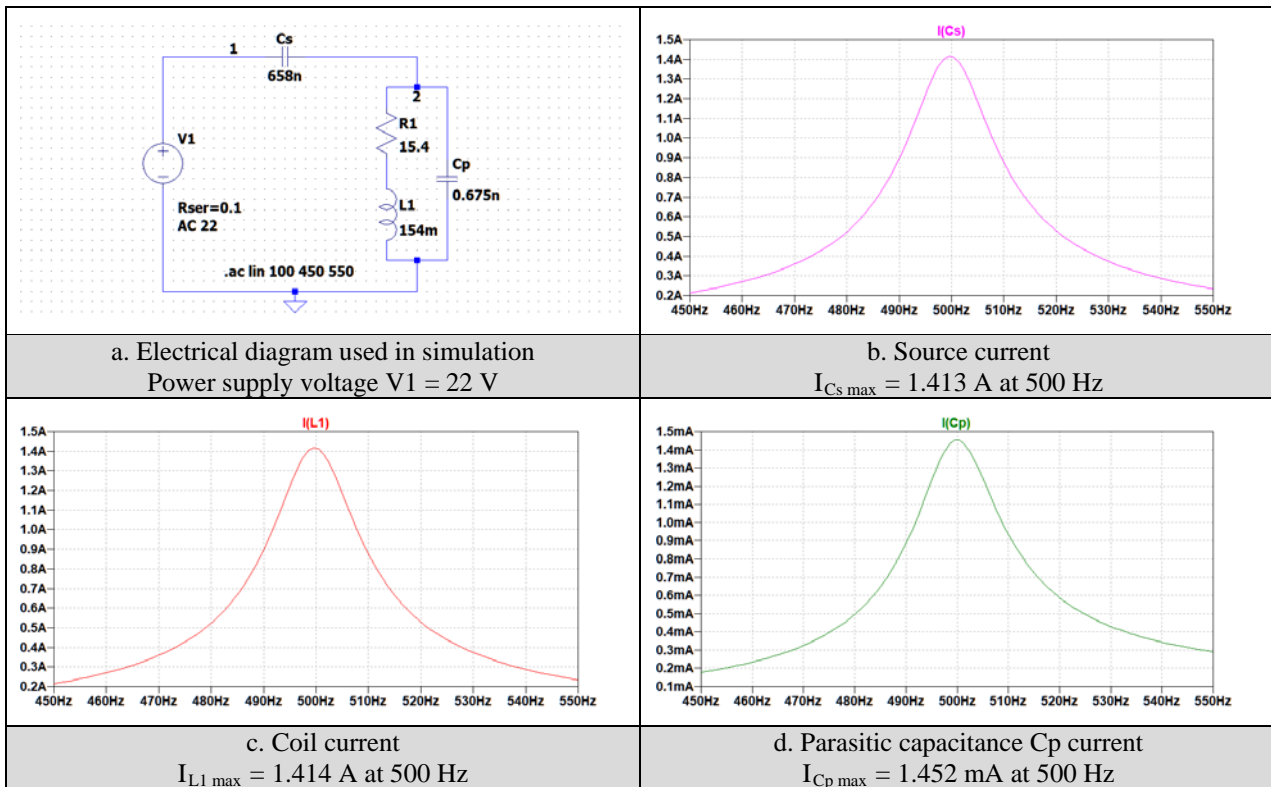


Fig. 17. Simulation of 500 Hz series resonance applied to the HC:
a) electrical circuit; b) the source current; c) the coil current; d) the parasitic capacitance current.

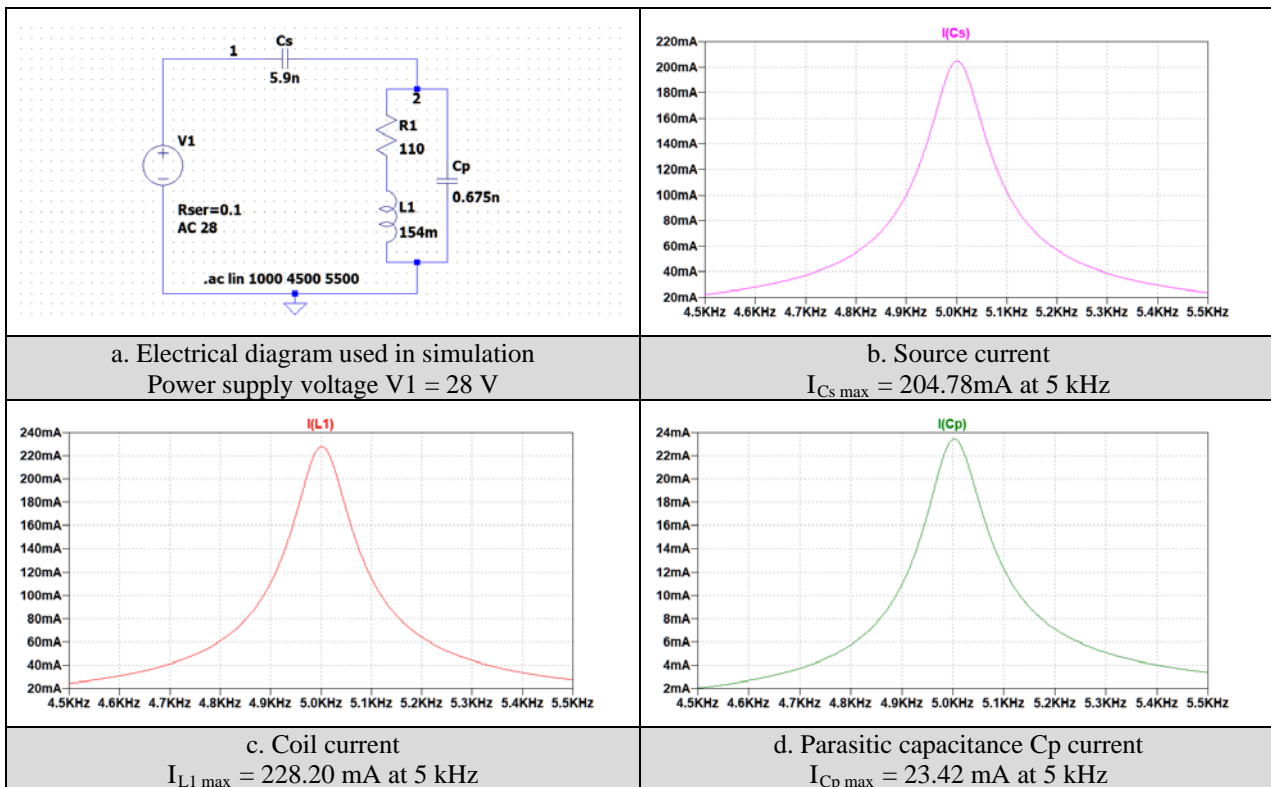


Fig. 18. Simulation of 5 kHz series resonance applied to the HC:
a) electrical circuit; b) the source current; c) the coil current; d) the parasitic capacitance current.

VI. EXPERIMENTS AND CALIBRATIONS

The measuring instrument used for calibration is the EFA-1 transfer standard [17] - a magnetic field analyser with internal three-axis B sensor that was previously calibrated at PTB Germany. This device performs measurements in the range from 5 Hz to 32 kHz (3 dB).

EFA-1 was arranged so that the field sensor was placed at the origin of the HC coordinate system. In order to determine the precise positioning of the field sensor, the anti-HC mounting is used. An anti-HC is the same HC, except the current in the two coils flows in opposite directions, similar to a gradiometer configuration (differential connection). At the centre point ($x = 0, y = 0, z = 0$), the magnetic field must be equal to zero. In our experiment for $I_L = 0.4$ A, the correction is $5 \mu\text{T}$.

Self-developed software [18] is used to check the uniformity of the magnetic field generated by the HC using the transfer standard. The magnetic induction is measured with the EFA-1 transfer standard and the electric current passing through the Helmholtz coils is determined by measuring the voltage drop across a shunt, with a Keythley 2000 multimeter. In order to increase the measurement accuracy, ten readings were performed on both devices, and the average value and the standard deviation are computed. The graphical interface of the employed software is illustrated in Fig. 19, while the result of the calibration of a magnetic field probe (EFA 300) is shown in Fig. 20.

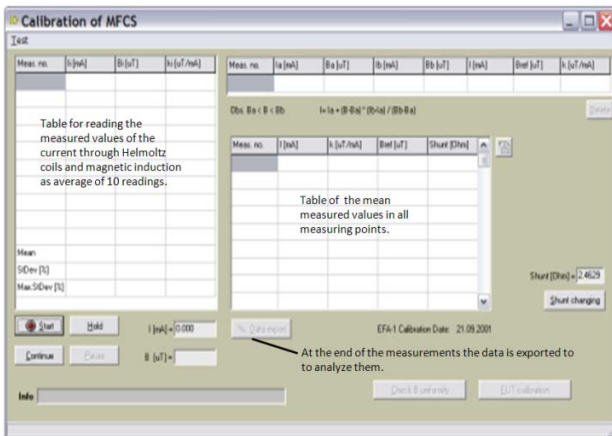


Fig. 19. Graphical user interface of the software for used checking the magnetic field uniformity.

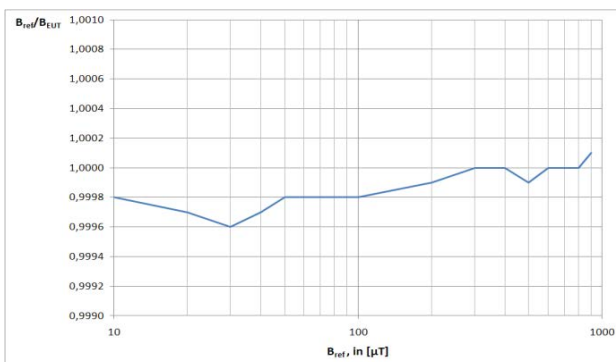


Fig. 20. Calibration result: ratio EFA-1/EFA-300.

The measurements included in Table 4, corresponding to the series resonant circuit were performed in order to verify the simulation results. As it can be noticed, the voltage drop across the coils U_L , at higher frequencies represent an important limiting factor (e.g. 4 V/turn at 5 kHz for a total applied voltage of 1100 V).

TABLE IV.
THE MEASURED VALUES IN THE SERIES RESONANCE CIRCUIT.

f [Hz]	50	673	1213	2460	5230
I_L [A]	0.4	0.4	0.4	0.4	0.2
B [μT]	103	103	103	103	52
U_L [V]	21	281	515	1004	1100

VII. CONCLUSIONS

A request from industry customers to calibrate magnetic field sensors for operating frequencies up to 10 kHz led the authors to verify the extent to which the existing Helmholtz coil system at ICMET Institute could be used for this purpose. This system with 1×1 m rectangular coils and multilayer solid copper wire winding was built and certified only for the working frequency of 50 Hz.

The paper demonstrates that the original HC system can operate without any modification at frequencies at least 100 times higher than the frequency for which it was built.

It determines the magnetic field generated by a HC system fulfilling the Helmholtz condition and its uniformity. The analytical calculation of the field uniformity results in a longitudinal zone of approximately 200 mm on the coils axis. By using numerical calculations based on FEM Maxwell software determines a field uniformity volume for a relative deviation of 1, 2 and 3 %. For a relative deviation of 2 % taken as a reference, the working volume is: 180 mm on the coils axis (longitudinal axis OY) \times 300 mm on the transversal axis (OX), \times 100 mm on the vertical axis (OZ), an acceptable volume for the calibration of many magnetic field sensors.

It can be noted that the vertical dimension of the field uniformity volume is smaller than the other dimensions – this is due the wires connecting the two HC coils, which were carrying currents of opposite directions.

By knowing the spatial distribution of the field deviation relative to the centre value, a field correction can be applied for sensors exceeding the uniformity volume. The experimenter can apply the correction by performing the field integration from the system centre to the longitudinal extremity.

The performed experiments aimed on the one hand to confirm the analytical and numerical results for the structure of the magnetic field and on the other hand to identify the parameters of the HC system in the extended frequency range initially proposed.

Some of the important results presented in the paper are:

- the comparison of the HC coils self inductance: FEM method vs measurement (76 vs 77 mH);
- the measurement in the frequency domain of all system parameters with an unique device of the Vector Network Analyzer type;

- the determination of the resonant frequency (15.6 kHz) of the HC system which makes possible measurements up to about 10 kHz;
- the application of the series resonance method that ensures equal currents through the two coils and reduces the necessary excitation power;
- the exact determination of the true magnetic midpoint of the HC system taking into account its inherent constructive imperfections.

Source of research funding in this article: Research program of the Military Technical Academy, George Cosbuc, Bucharest, Romania.

Contribution of authors:

First author – 50%

First co-author – 10%

Second co-author – 10%

The third co-author – 10%

The fourth co-author – 10%

The fifth co-author - 10%

Received on July 10, 2020

Editorial Approval on November 17, 2020

REFERENCES

- [1] DKD (Deutsche Kalibrierdienst) Calibration Certificate DKD-K-18701,1997, Renewed 2009.
- [2] W. M. Frix, G. G. Karady, and B. A. Venetz, "Comparison of calibration systems for magnetic field measurement equipment", *IEEE Trans. Power Del.*, vol. 9, pp. 100–108, Jan. 1994.
- [3] H. Zijlstra, *Experimental Methods in Magnetism*, vol 2. Measurement of magnetic quantities, North-Holland Publishing Company- Amsterdam, 1967.
- [4] G. Crotti, M. Chiampi, and D. Giordano, "Estimation of Stray Parameters of Coils for Reference Magnetic Field Generation", *IEEE Trans on Magnetics*, Vol. 42, No. 4, pp. 1439-1442, April 2006.
- [5] A. Marinescu, I. Dumbravă, I. Pătru, A. Scornea, "Resonant power supply for Helmholtz coil system for the calibration of magnetic field sensors to frequencies of up to 10 kHz", CEM Workshop, Craiova, 2016.
- [6] T. Tsz-Ka Li, Tri-axial Square Helmholtz Coil for Neutron EDM Experiment, The Chinese University of Hong Kong, Hong Kong, China, Aug. 2004.
- [7] O. Baltag, D. Costandache, and M. Rau, Bioelectromagnetism laboratory - case study, 4th Int. Symp. on Electrical and Electronics Engineering (ISEEE), Galati, Oct. 2013.
- [8] D. Costandache, A. Banarescu, O. Baltag, I. Rau, M. Rau, and S. Ojica, "Dynamic Shielding in Biomagnetism", International Conference on Advancements of Medicine and Health Care Through Technology - IFBME Proc., vol. 26, pp. 121-124, Cluj Napoca, Sept. 2009.
- [9] R. Bargallo, *Finite Elements for Electrical Engineering*. Barcelona, Spain: Universitat Politecnica de Catalunya, 2006.
- [10] S. Humphries, *Finite-element Methods for Electromagnetics*, Albuquerque, SUA, New Mexico, 2010.
- [11] C. Racasan, A. Racasan, V. Topa, and C. Munteanu, *Numerical Modeling of the Electromagnetic Field (in Romanian)*, Casa Cartii de Stiinta, Cluj-Napoca, 2007.
- [12] F. Enache, Gh. Gavrilă, and E. Cazacu, "Study of the uniform magnetic field domains (3D) in the case of the Helmholtz coils", *Rev. Roum. Sci. Techn. – Électrotechn. et Énerg.*, vol. 53, no. 2, pp. 189–197, 2008.
- [13] O. Baltag, G. Rosu, and M. Rau, "Magnetic field of parallel and twisted wire pairs," the 10th Int. Sympos.on Advanced Topics in Electrical Engineering, Bucharest, Romania, 2017, pp. 324-329. doi: 10.1109/ATEE.2017.7905020.
- [14] N. Nouri and B. Plaster, "Comparison of magnetic field uniformities for discretized and finite-sized standard, solenoidal, and spherical coils," *Nuclear Instruments and Methods in Physics Research Section A: Accelerators, Spectrometers, Detectors and Associated Equipment*, vol. 723, pp. 30–35, 2013.
- [15] P. Koss, C. Crawford, G. Bison, E. Wursten, M. Kasprzak, and N. Severijns, "PCB Coil Design Producing a Uniform Confined Magnetic Field", *IEEE Mag. Let.*, vol. 8, 2017. doi: 10.1109/LMAG.2017.2701771.
- [16] A. Marinescu, I. Dumbravă, „Using VNA for IPT Coupling Factor Measurement”, in *IEEE – PEMC, Varna*, 2016.
- [17] EFA1 User Manual [Online]. Available: <http://www.narda-sts.us>
- [18] I. Dumbravă, A. Marinescu, G. Mihai, A. Scornea, "Laboratory for Magnetic Field Probes Calibration", SICEM Symposium, Bucharest, 2002.

Wireless Remote Control for the Anti-Hail Missiles Launch Ramp Positioning System

Sorin Stepan, Gheorghe Manolea*

Conestoga College, Ontario, Canada, e-mail: sostepan@yahoo.com

* University of Craiova / Department of Electromechanical, Environmental and Applied Informatics, Craiova, Romania
e-mail: ghmanolea@gmail.com

Abstract – This paper describes a wireless remote control designed for the positioning system of the launching pad of anti-hail missiles used by the Romanian Anti-Hail System. The remote control operates in the ISM band of 2,4 GHz and was successfully tested on a simplified, small size, experimental model of the actual launch ramp. The remote control allows the operator to position the launch ramp on two axes, azimuth, and elevation, and fire the missiles, using momentary push buttons. A 16x2 characters LCD display indicates the current position of the ramp, and the presence and the type of the anti-hail missiles loaded on the ramp. The remote control was built using Arduino microcontrollers and radio frequency transceivers and uses two separate one-way transmitter-receiver radio channels. The simplified experimental model of the launch ramp features the main functional characteristics of the actual ramp and was designed and built for the purpose of testing the remote control, due to no access to the actual ramp, along with the intention of using it to train the Local Unit operating personnel during the off-season time. When designing and building the remote control and the experimental model of the ramp it was taken into consideration an easy implementation on the actual ramp, with minimal modifications.

Cuvinte cheie: *telecomandă, antigrindină, microcontroler, modul de emisie-recepție, lansator de rachete, sistem de poziționare*

Keywords: *remote control, anti-hail, microcontroller, transceiver, missiles launch ramp, positioning system.*

I. INTRODUCTION

As a result of a research documentation and a visit to an anti-hail Zonal Command Center and an anti-hail Local Unit, it has been found that from an operational point of view, the anti-hail system in Romania uses launching ramps which can be positioned manually or by using temporary cables [1], [2], [3].

The wireless remote control described in this paper speeds up the process of ramp positioning, eliminates the inconvenience of placing and removing the temporary cables every season, and reduces the cost of the equipment by avoiding the cables.

II. THE REAL MISSILES LAUNCH RAMP AND THE EXPERIMENTAL MODEL

A. Description and parameters of the real ramp

The missiles launch ramps used by the Romanian Anti-Hail System are manufactured by SC

Electromecanica Ploiesti and are intended to ensure the launching of eight RAG-96 or RAG-96S type missiles (Fig. 1) [1]. Azimuth and elevation positioning with a precision of 1.5° is possible between 0 and 360° for the azimuth, and between 20° and 85° for the elevation respectively. The ramp uses synchronous motors with permanent magnets for azimuth and elevation positioning directions, driven by intelligent drives. The connection between the motors and the mechanical structure of the ramp is accomplished with worm gears and worm-wheel transmission which ensures one-way movement and mechanical locking [4].



Fig. 1. The missiles launch ramp used by the Romanian Anti-Hail System

B. Description of the experimental model of the ramp

A simplified, small size, experimental model of the real ramp was built to test the remote control (Fig. 2) [5].

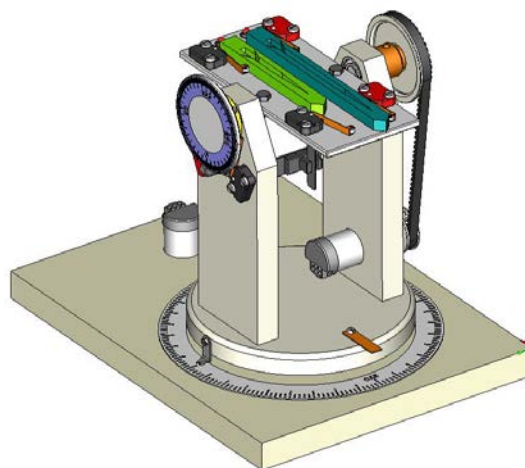


Fig. 2. The experimental model of the missiles launch ramp.

The experimental model features the two axes positioning of the actual ramp using two DC geared motors with encoders, controlled by a dual H-Bridge motor driver. The connection between the motors and the mechanical structure of the experimental model is achieved by gears and timing belts transmission. Feedback regarding azimuth and elevation coordinates is obtained from the pulses generated by the motor encoders. Optical sensors are used to set the home position on the two axes, and limit switches to indicate the presence and type of two missiles. A 20° to 85° interval for the elevation is set by two limit switches. The missiles firing is not possible outside this interval, and are simulated by two LEDs. The experimental model is electrically connected to the remote control receiver by six cables provided with DB9 connectors (Fig. 3).

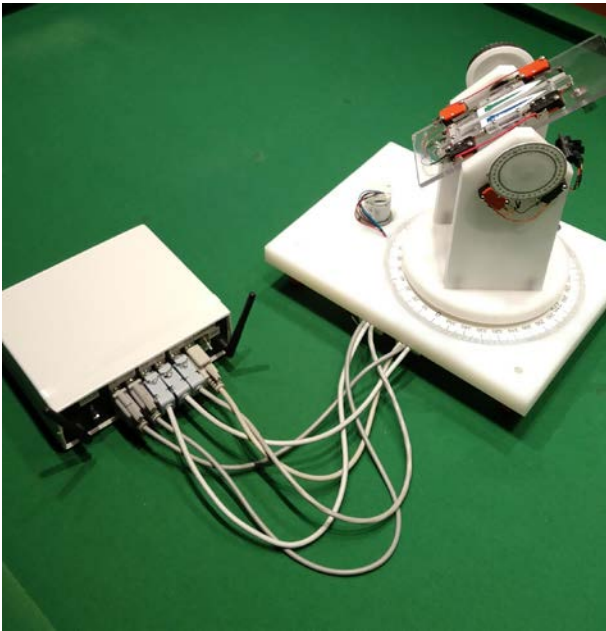


Fig. 3. The experimental model connected to the remote control receiver.

A 5V voltage from the remote control receiver box provides the power supply for the driver, motors, sensors, and LEDs on the experimental model.

When making the experimental model, it was taken into account that it retains the functional characteristics of the real ramp, so that after testing the remote control on the model, it can be implemented on the real ramp with minimal changes and the experimental model can be used for staff training in the active off-season.

The electrical schematic of the experimental model is shown in Fig. 4.

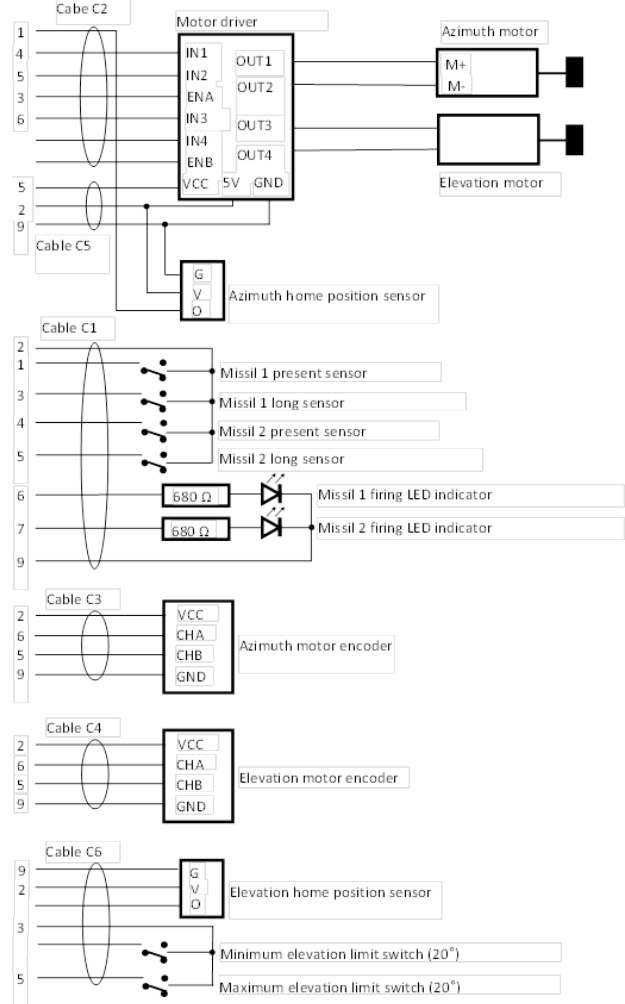


Fig. 4. Electrical schematic of the experimental model

III. THE REMOTE CONTROL

A. Description and electrical diagram

The remote control uses two unilateral radio communication channels (transmitter-receiver) between Arduino type microcontrollers [6], [7], by using the NRF24L01 transmit-receive modules [8].

The first communication channel is sending commands from the operator to the ramp (move the ramp up, down, left or right, and fire the missiles), the second channel transmits data on the ramp to the operator (position, presence and type of missiles).

The block diagram of the first communication channel is that of Fig. 5.

This radio communication channel uses an Arduino Nano microcontroller at the transmitter and an Arduino Mega microcontroller at the receiver.

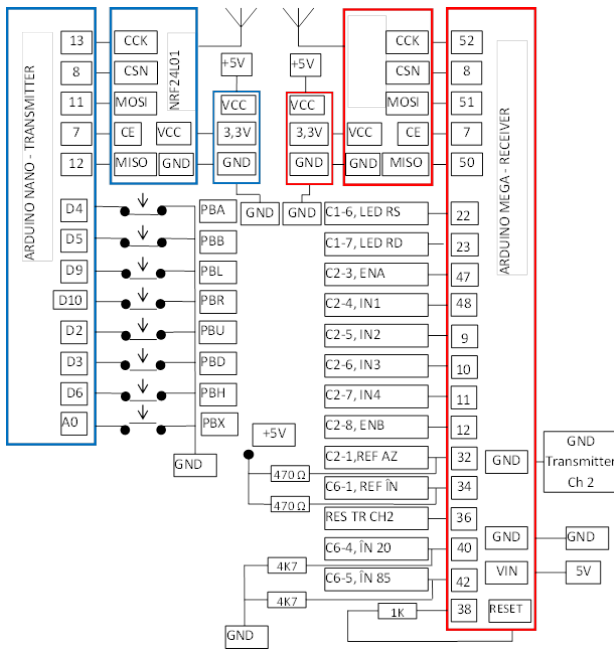


Fig. 5. Electrical schematic of the first radio channel

When the operator presses or releases any of the momentary pushbuttons on the remote control, a short message containing one character is sent from the remote control to the receiver box. The Arduino Mega microcontroller on the receiver side interprets the message and modifies the corresponding output pins accordingly. For example, when the PBL button is pressed, the Arduino Nano microcontroller from the transmitter sends the "L" character, at the reception of which the Arduino Mega microcontroller from the receiver switches the ENA and IN1 outputs (pins 47 and 48) to logic one, and the IN2 output (pin 9) to logic level zero. The three mentioned outputs of the microcontroller from the receiver are connected to the driver module which will control the clockwise rotation of the motor used to move the model in the azimuth direction. When releasing the PBL button, the character "I" is transmitted. This has as an effect at the reception the passage of pins 47, 48, and 9 at zero logic level and implicitly the azimuth motor stops.

It should be noted that, as a courtesy to other radio channel users, although to move the ramp in one direction, the corresponding push-button must be kept pressed until the desired position is reached, the command is transmitted on the radio channel only when the button is pressed, then the radio channel is not used. A second signal, the stop command, is sent when the button is released.

The second radio communication channel of the remote control uses two Arduino Mega 2560 and two RF transmitter modules NRF24L01 like those of the first channel. The second radio communication channel operates on a different frequency than the first channel; the frequencies are software selectable by the user.

The block diagram of the second radio communication channel of the remote control is shown in Fig. 6.

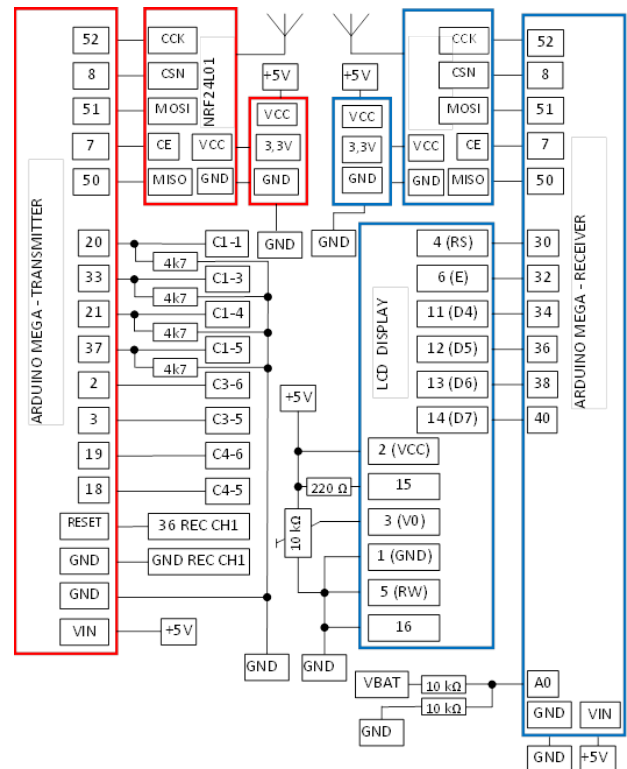


Fig. 6. Electrical schematic of the second radio channel

The microcontroller from the second radio channel transmitter receives on inputs 2 and 3 the quadrature pulses generated by the azimuth motor encoder; the elevation motor encoder is connected to inputs 18 and 19. All these inputs allow interrupts in the program execution, which eliminates the possibility of losing pulses from the encoders.

The pulses coming from the two encoders are counted by the microcontroller in two reversible counters. Because when moving the ramp model by one degree in either direction (azimuth or elevation) the encoder in that direction generates 21 pulses, the two counters are reset when the limits of 21 or -21 are reached, simultaneously with the signaling of the produced event. Thus, when moving the model one degree to the right in the azimuth direction, the second radio channel transmitter microcontroller sends the character "Z" to the receiver, and when moving one degree to the left, the character "z" is transmitted. For moving the model by one degree on elevation, the characters "E" and "e" are transmitted. The receiver microcontroller interprets messages received from the transmitter and displays the position of the ramp on a 16x2 characters LCD display, with one-degree accuracy.

Fig. 7 shows the remote control, which contains the transmitter of the first radio communication channel and the receiver of the second channel.

The remote control can be powered up from a 12V / 500 mA DC power supply or from a 6V / 1.3 Ah internal battery.



Fig. 7. The operator remote control

B. RF measurements

The operating distance has been determined in an urban environment, with the remote control powered by the internal battery. The transmitters power was set to 12 dBm (15.85 mW). The distance between the remote control and the receiver connected to the model has been progressively increased, while operating the remote control and monitoring the LCD. The remote control worked correctly up to a distance of about 70m, when the radio connection was lost. The radio connection was resumed at a distance of 55 m (Fig. 8).

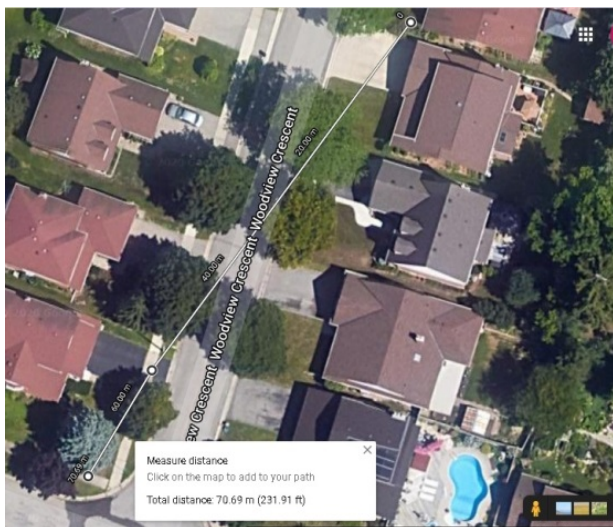


Fig. 8. Operating distance measurement for the remote control

The transmitter power, the received power at different distances, and the frequency spectrum measurements for the first radio communication channel of the remote control (2499-2500 MHz) were performed on Rohde &

Schwarz CMU200 and CMW500 radio communications testers [9].

When connecting the remote control via 1.5 m RF cable to the CMU200 radio frequency tester used as a spectrum analyzer, a maximum emission power inside the 2499-2500 MHz frequency channel of approximately 10 dBm was measured. This confirms the set power of 12 dBm if we consider the power losses on the cable and connectors. It can be seen from Fig. 9 that the radiated power outside of the 1 MHz channel is at least 20 dB lower than the maximum power, which means that the radiated power outside the allocated frequency channel is less than 1% of the total radiated power (Fig. 9).

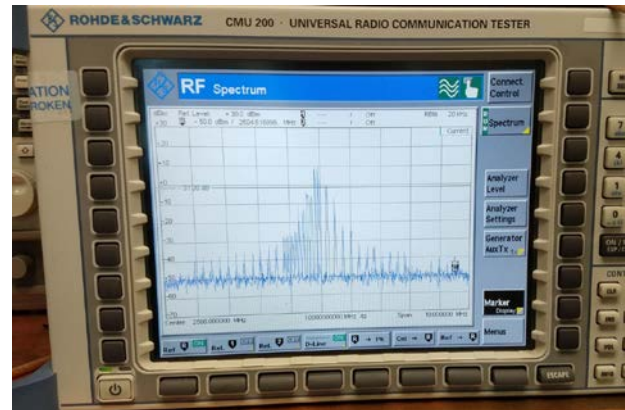


Fig. 9. The frequency spectrum measurement for a 1.5m cable connection to the test equipment

The received power at different distances was measured inside a building, with interior walls. The measured received power at 30 m was -80 dBm (10 pW). At this distance, the remote control worked properly in the presence of a disturbing signal from a mobile phone that has been placed besides the receiver antenna and connected to the Wi-Fi network. The disturbing signal had a -50 dBm power (10 nW) at a 2 MHz higher frequency than the central channel frequency of the remote control (Fig. 10).

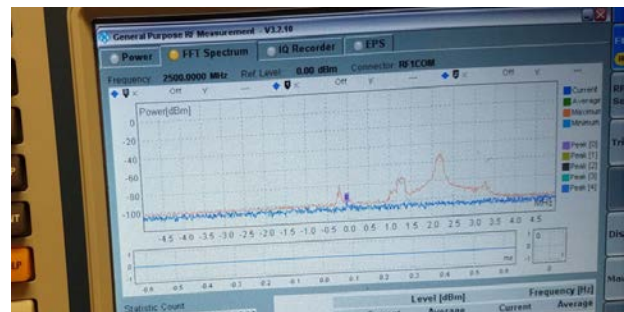


Fig. 10. The emission spectrum measured at 30 m from the remote control in the presence of a Wi-Fi signal from a mobile phone located near the receiver antenna.

V. CONCLUSION

The remote control operating in the 2.4 GHz frequency band, built with Arduino family microcontrollers and NRF 24L01 transceiver modules is a functional and inexpensive technical solution for operating the anti-hail rocket launch

pad. The testing of the remote control, both outdoors and with laboratory equipment, confirmed its functionality, the accuracy of the ramp positioning was one degree. The implementation of this technical solution on the real ramp requires minimal modifications of the equipment used, to adapt the voltage levels from the output of the remote control receiver to the voltage levels necessary for the intelligent drivers who control the motors of the real ramp.

ACKNOWLEDGMENT

The research was carried out during the elaboration of the doctoral thesis of the first author. The CITT models and experience in the field of hail systems were used for the doctoral research. Experimental measurements have been done in the Telecommunication Laboratory of Conestoga College, Ontario, Canada. The ramp model and the remote control were built from own funds.

Contribution of authors:

First author – 90%

First coauthor – 10%

Received on June 10, 2020

Editorial Approval on November 5, 2020

REFERENCES

- [1] G. Manolea, L. Alboteanu, S. Stepan "Contributions to the Development of Complementary Equipment for the Romanian Anti-Hail System," 11th International Conference on Electromechanical and Power Systems, 12-13 October 2017, Chişinău.
- [2] G.Manolea, L.I.Alboteanu, S. Stepan, "An algorithm for the adaptive control of anti hail missile launch ramps," IASI POLYTECHNIC INSTITUTE BULLETIN Published by "Gheorghe Asachi" Technical University of Iaşi Vol 64, Nr .2, year 2018 Section ELECTROTECHNICS. ENERGETICS. ELECTRONICS , ISSN 1223-8139, <http://www.bulipi-eee.tuiasi.ro>
- [3] G.Manolea, L.I. Alboteanu, A.Novac, C.Şulea-Iorgulescu, S. Stepan, "Contributions Regarding the Modernization of the Anti-Hail Rocket Launcher Monitoring System" Annals of the University of Craiova, 2019, <https://ieeexplore.ieee.org/document/8905892>
- [4] M.Ş.Nicolae," Research on the realization of a system of automatic positioning of the launching ramps of the units for combating hail falls" - Doctoral thesis, Craiova, 2015
- [5] S. Stepan, "Research on the radio remote control of anti-hail rocket launcher positioning systems"- Doctoral thesis, Craiova, 2020
- [6] <https://www.arduino.cc/en/Guide/Introduction>
- [7] <https://store.arduino.cc/usa/mega-2560-r3>
- [8] <https://www.nordicsemi.com/Products/Low-power-short-range-wireless/nRF24-series>
https://www.rohde-schwarz.com/us/products/test-and-measurement/wireless-communications-testers-systems/wireless-communication-testers-systems/wireless-device-testers_86475.html

Influence of Synchronized Measurement Errors on the Results of Identification of the Transmission Line Parameters

Murdid Ecaterina*, Boris Jingan†, Dobrea Ina*, Vasilos Elena‡,

* Department of Power Engineering, Technical University of Moldova, Chişinău, Moldova, e-murdid@yandex.ru

† Department of Power Engineering, Technical University of Moldova, Moldova, boris.jingan93@gmail.com

* Department of Power Engineering, Technical University of Moldova, Chişinău, Moldova, ina.dobrea@ee.utm.md

‡ Department of Power Engineering, Technical University of Moldova, Moldova, elena.vasilos@ee.ut.md

Abstract - The parameters of transmission lines, as a rule, are determined by reference data, but during the operation, it might vary essentially from the actual data. There are noted the reasons for the parameters' modification. This paper explains the opportunity of parameter identification based on the synchronized measurements during the operation of the transmission line. The methods of parameter identification can be classified by various criteria. The diagram of classification was elaborated for the first time. Transmission lines can be represented in the form of quadripole and the T- and II-forms equivalent schemes, so, applying only the current and voltage synchronized measurement on both ends it is possible to obtain passive parameters of the line. There are presented final formula of six most effective methods for parameter identification of the transmission lines. All analyzed methods were verified with the models of real transmission line. There were compared the results of all proposed methods: the relative errors of calculation for all mentioned methods are less than 1%. The obtained results show the high accuracy of parameter identification for the proposed methods. The influence of measurement errors upon the values of parameters' results was analyzed in this work. The main contribution of this paper lies in the classification of the methods of transmission line parameters identification and in the research of influence of measurement errors on the results of the parameter identification for transmission lines.

Cuvinte cheie: *linie electrică, măsurări sincronizate, parametrii schemelor echivalente în forma de II, coeficienții cuadripolului, bilanțul curenților, bilanțul puterilor.*

Keywords: *transmission line, synchronized measurements, parameters of equivalent circuit in II-form, quadripole coefficients, currents balance, powers balance.*

I. INTRODUCTION

Transformers and transmission lines (TL) being the most used elements of transmission and distribution power systems have their own specific mathematical models, that take the form of equivalent schemes.

Solving the problems of the management of the different regimes of the electric power systems is performed with using mathematical models. Mathematical models are used for calculation permanent regime of the electric power systems, optimization regimes, static state estimation, reliability evaluation to small disturbances and short current calculation.

Basis of mathematical models is equivalent scheme of power system which is composed from equivalent circuits of basic elements connected between them according to real circuit of power system. Basic elements are electric line, two or three winding transformer, branch transformer (transformer with split winding), autotransformer, power sources, consumers, inductor, capacitor batteries. Parameters of equivalent schemes are determined from catalogue and are named catalogue data. This methodology is enough exact, but it doesn't consider all real circumstances as weather conditions, loading of basic elements and other factors. The difference between real values and those calculated with catalogue data might be considerable [1, 2].

Errors can take following values [3]:

- for active resistance $\Delta R = \pm 18-20\%$
- for reactance $\Delta X = \pm 10\%$
- for conductance ΔG and capacitive susceptance $\Delta B = \pm 25\%$.

Numerous applications in electrical power systems require the exact knowledge of the parameters of the equivalent schemes of transmission lines. These parameters are active resistance R, reactance X, conductance G and capacitive susceptance B, length of electric line. It is generally known, that some parameters for example active resistance varies due to both line's length and temperature; reactance varies only from function of line's length, but susceptance varies from function of line's length and ice accretions. In turn length of electric line is influenced not

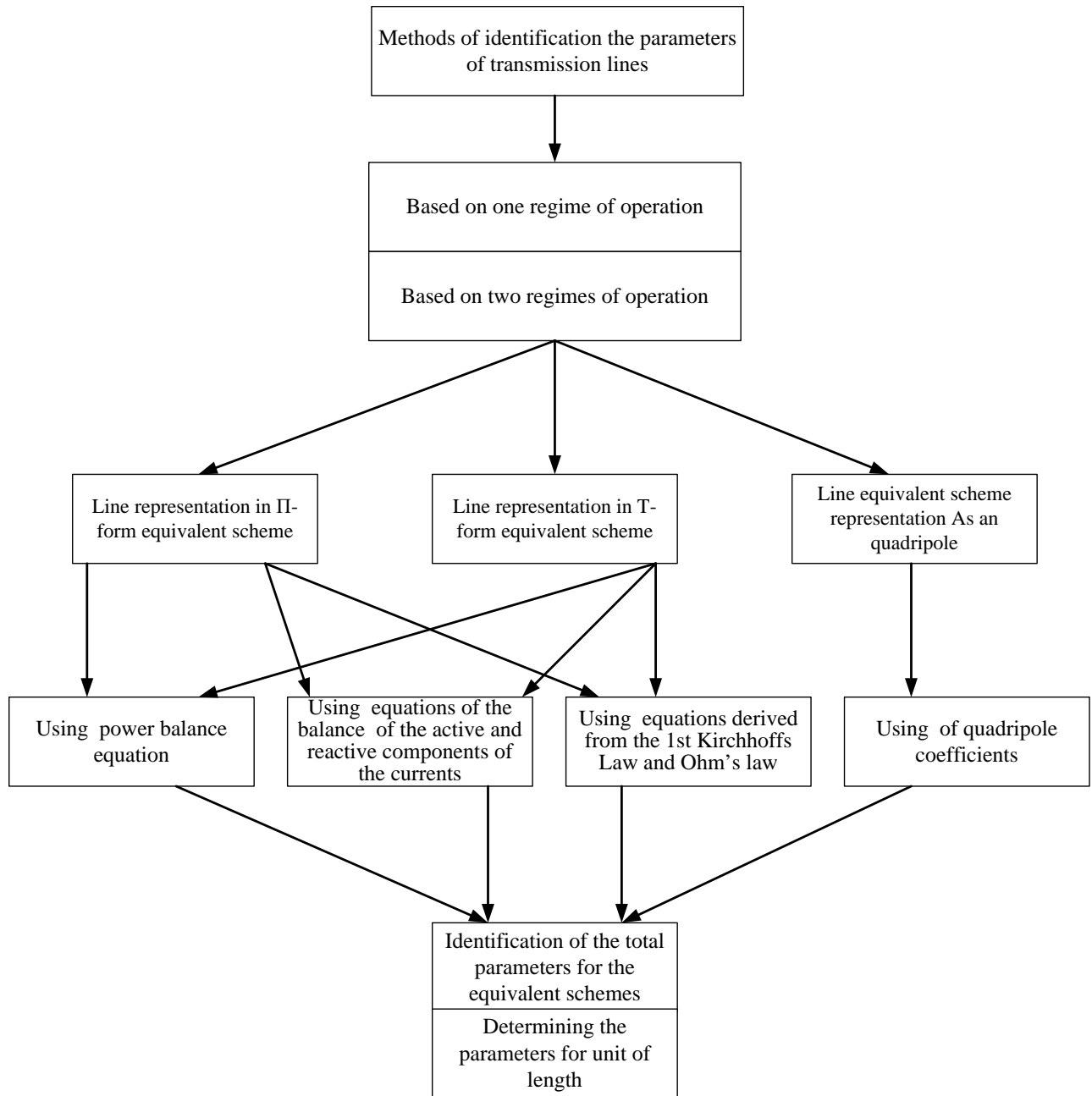


Fig. 1 Classification of the methods of parameter identification for transmission lines based on synchronized measurements.

only by weather conditions (temperature of environment, speed and direction of wind, presence of ice accretion), but also by power losses caused by effect Joule-Lenz.

Thus it is current to identify parameters of electric line using information about parameters of some regimes obtained from measurement systems' information. This information is provided by:

- data recorder of disturbances;
- phase measuring unit synchronized in time - PMU.

The resulting errors of the measured parameters are estimated at least [5]:

- ±0,1 for phase angle;
- ± 0,2 for voltages;
- ± 0,3 for currents;
- ± 0,4 for power.

II. CLASSIFICATION OF METHODS FOR IDENTIFYING PARAMETERS OF EQUIVALENT CIRCUITS

Till now, there have been proposed in the literature various methods to identify the parameters of equivalent circuits of transmission line. Some methods are based on the set of measured phasors (the voltages \underline{U}_1 and \underline{U}_2 and currents \underline{I}_1 and \underline{I}_2 in nodes 1 and 2), obtained from PMU and other methods are based on the arrays of instantaneous values $(U_1(t_j), I_1(t_j), U_2(t_j), I_2(t_j))$ obtained from fault (disturbances) recorder, that are located on the both sides of the power line. The publication of the results of these works ensured the large volume of information, which is contained in magazines,

articles, reports presented at scientific conferences and monographs. The study of the various suggestion, included in these publications, as well as their critical analysis can be made easier if a classification of these methods was established. Fig.1 shows a diagram, which illustrates a possible classification of methods for identification of the parameters of equivalent schemes of power lines. Classification is based on the following technical criteria:

- number of used regimes;
- type of the used informational measurement system;
- transmission line presentation models;
- the systems of equations used to describe the power line regime.

The methods of identification by the number of used regimes are divided into:

- methods with one set of measured values;
- methods with two sets of measured values.

Depending on the used measurement system information are divided into:

- methods based on the arrays of instantaneous values ($U_1(t_j)$, $I_1(t_j)$, $U_2(t_j)$, $I_2(t_j)$), obtained from fault recorder, that are located on the both sides of the power line;
- methods based on the sets of synchronized measured phasors (\underline{U}_1 , \underline{U}_2 and \underline{I}_1 , \underline{I}_2), obtained from PMU, placed on the both sides of the power line.

There are used various mathematical models of transmission lines:

- bipole line representation;
- quadripole line representation;
- line representation in T-form equivalent scheme;
- line representation in Π -form equivalent scheme.

Also it might be mentioned that there are used various modes of regimes' description:

- equations derived from the 1st Kirchhoff's law;
- equations derived from the Ohm's law;
- different forms of equations derived from nodal analysis (balance of power in nodes, balance of active and reactive components of currents in nodes).

III. SHORT METHOD DESCRIPTION

There are described below the final formulas of the methods that in previous studies [6] gave the best results. The below mentioned methods are performed with the use of equivalent scheme of transmission line in Π -form or quadripole form (Fig.2).

A. Method 1: based on the equations derived from the 1st Kirchhoff's law with one set of measured values

The final formula of the method will be presented on the example of the Π -form equivalent circuit (Fig. 2 a). The measured values for this circuit are the voltages \underline{U}_1 and \underline{U}_2 and currents \underline{I}_1 and \underline{I}_2 in nodes 1 and 2.

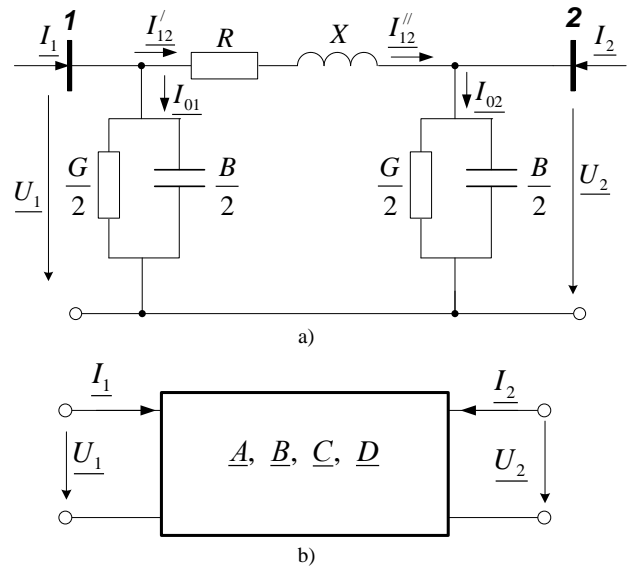


Fig. 2 Equivalent scheme of the transmission line a) in Π -form and b) in quadripole form.

For node 1 it is obtained:

$$\underline{Z}_{12} = \frac{\underline{U}_1^2 - \underline{U}_2^2}{(\underline{I}_1 \underline{U}_2 + \underline{I}_2 \underline{U}_1)} \quad (1)$$

$$\underline{Y} = \frac{2 \cdot (\underline{I}_1 - \underline{I}_2)}{\underline{U}_2 + \underline{U}_1} \quad (2)$$

B. Method 2: powers balance method with one set of measured values

According to this method it is necessary to use measurements of currents and voltages in the single regime at the both ends of transmission line - \underline{U}_1 , \underline{I}_1 and \underline{U}_2 , \underline{I}_2 (otherwise set \underline{U}_1 , \underline{S}_1 and \underline{U}_2 , \underline{S}_2).

$$\begin{cases} P_1 = \underline{U}_1^2 G_t - (\underline{U}_1^2 - \underline{U}_1 \underline{U}_2 \cos \delta_{12}) \cdot G_{12} + \\ \quad + \underline{U}_1 \underline{U}_2 \sin \delta_{12} B_{12} \\ Q_1 = -\underline{U}_1 \underline{U}_2 \cos \delta_{12} G_{12} - \underline{U}_1^2 B_t + \\ \quad + (\underline{U}_1^2 - \underline{U}_1 \underline{U}_2 \cos \delta_{12}) \cdot B_{12} \\ P_2 = -\underline{U}_2^2 G_t + (\underline{U}_1 \underline{U}_2 \cos \delta_2 - \underline{U}_2^2) \cdot G_{12} - \\ \quad - \underline{U}_1 \underline{U}_2 \sin \delta_2 B_{12} \\ Q_2 = \underline{U}_1 \underline{U}_2 \sin \delta_2 G_{12} + \underline{U}_2^2 B_t + \\ \quad + (\underline{U}_1 \underline{U}_2 \cos \delta_2 - \underline{U}_2^2) \cdot B_{12} \end{cases} \quad (3)$$

By solving linear system of equations (3) the values of longitudinal (G_{12} , B_{12}) and transversal (G_t , B_t) admittances are obtained. Thus, the transmission line parameters are calculated by following formula:

$$\underline{Z}_{12} = R_{12} + jX_{12} = \frac{G_{12}}{G_{12}^2 + B_{12}^2} + j \frac{B_{12}}{G_{12}^2 + B_{12}^2} \quad (4)$$

and

$$\underline{Y} = G_t + jB_t \quad (5)$$

C. Method 3: powers balance method with two sets of measured values

There are used measurements of currents and voltages in two operating regimes at the both ends of transmission line. Values $\underline{U}_1^{(1)}$, $\underline{I}_1^{(1)}$ and $\underline{U}_2^{(1)}$, $\underline{I}_2^{(1)}$ (otherwise set $\underline{U}_1^{(1)}$, $\underline{S}_1^{(1)}$ and $\underline{U}_2^{(1)}$, $\underline{S}_2^{(1)}$) are obtained from the 1st set of measurement parameters, and $\underline{U}_1^{(2)}$, $\underline{I}_1^{(2)}$ and $\underline{U}_2^{(2)}$, $\underline{I}_2^{(2)}$ (otherwise set $\underline{U}_1^{(2)}$, $\underline{S}_1^{(2)}$ and $\underline{U}_2^{(2)}$, $\underline{S}_2^{(2)}$) – from the 2nd one.

$$\begin{cases} P_2^{(1)} = -U_2^{(1)}G_t + (U_1^{(1)}U_2^{(1)} \cos \delta_2 - U_2^{(1)}) \cdot G_{12} - \\ -U_1^{(1)}U_2^{(1)} \sin \delta_2^{(1)} B_{12} \\ Q_2^{(1)} = U_1^{(1)}U_2^{(1)} \sin \delta_2^{(1)} G_{12} + U_2^{(1)}B_t + \\ + (U_1^{(1)}U_2^{(1)} \cos \delta_2^{(1)} - U_2^{(1)}) \cdot B_{12} \\ P_2^{(2)} = -U_2^{(2)}G_t + (U_1^{(2)}U_2^{(2)} \cos \delta_2^{(2)} - U_2^{(2)}) \cdot G_{12} - \\ -U_1^{(2)}U_2^{(2)} \sin \delta_2^{(2)} B_{12} \\ Q_2^{(2)} = U_1^{(2)}U_2^{(2)} \sin \delta_2^{(2)} G_{12} + U_2^{(2)}B_t + \\ + (U_1^{(2)}U_2^{(2)} \cos \delta_2^{(2)} - U_2^{(2)}) \cdot B_{12} \end{cases} \quad (6)$$

Passive parameters of the transmission line are found with the help of expressions (4) and (5).

D. Method 4: currents balance method with one set of measured values

There is derived the balance of active and reactive currents for the nodes 1 and 2 of transmission line equivalent scheme:

$$\begin{cases} I_{1a} = U_1 G_t - (U_1 - U_2 \cos \delta_{12}) \cdot G_{12} + U_2 \sin \delta_{12} B_{12} \\ I_{1r} = -U_2 \cos \delta_{12} G_{12} - U_1 B_t + (U_1 - U_2 \cos \delta_{12}) \cdot B_{12} \\ I_{2a} = -U_2 G_t + (U_1 \cos \delta_2 - U_2) \cdot G_{12} - U_1 \sin \delta_2 B_{12} \\ I_{2r} = U_1 \sin \delta_2 G_{12} + U_2 B_t + (U_1 \cos \delta_2 - U_2) \cdot B_{12} \end{cases} \quad (7)$$

By solving linear system of equations (7) the values of longitudinal (G_{12} , B_{12}) and transversal (G_t , B_t) admittances are obtained. Then, the transmission line parameters are determined by expressions (4) and (5).

E. Method 5: currents balance method with two sets of measured values

This method applies values from two sets of measured parameters.

Passive parameters of the transmission line are found with the help of expressions (4) and (5).

$$\begin{cases} I_{2a}^{(1)} = -U_2^{(1)}G_t + (U_2^{(1)} \cos \delta_2 - U_2^{(1)}) \cdot G_{12} - \\ -U_2^{(1)} \sin \delta_2^{(1)} B_{12} \\ I_{2r}^{(1)} = U_2^{(1)} \sin \delta_2^{(1)} G_{12} + U_2^{(1)} B_t + \\ + (U_2^{(1)} \cos \delta_2^{(1)} - U_2^{(1)}) \cdot B_{12} \\ I_{2a}^{(2)} = -U_2^{(2)}G_t + (U_1^{(2)} \cos \delta_2^{(2)} - U_2^{(2)}) \cdot G_{12} - \\ -U_1^{(2)} \sin \delta_2^{(2)} B_{12} \\ I_{2r}^{(2)} = U_1^{(2)} \sin \delta_2^{(2)} G_{12} + U_2^{(2)} B_t + \\ + (U_1^{(2)} \cos \delta_2^{(2)} - U_2^{(2)}) \cdot B_{12} \end{cases} \quad (8)$$

F. Method 6: quadripole coefficients

Due to the fact that transmission line is represented as passive quadripole ($\underline{A} = \underline{D}$), there are obtained coefficients from one set of measured values.

$$\underline{A} = \frac{U_1 \cdot I_1 + U_2 \cdot I_2}{I_2 \cdot \underline{U}_1 + \underline{U}_2 \cdot I_1} \quad (9)$$

$$\underline{B} = \frac{U_1^2 - U_2^2}{I_2 \cdot \underline{U}_1 + I_1 \cdot \underline{U}_2} \quad (10)$$

$$\underline{C} = \frac{I_1^2 - I_2^2}{I_2 \cdot \underline{U}_1 + I_1 \cdot \underline{U}_2} \quad (11)$$

So, the transmission line parameters are determined from the expressions:

$$\underline{Z}_{12} = \underline{B} \quad (12)$$

$$\underline{Y} = \frac{2(\underline{A} - 1)}{\underline{B}} \quad (13)$$

In order to compare the results of the proposed methods with the passive parameters obtained from catalogue data it is necessary to evaluate the measurement errors which appear during parameter identification. There are known random and systemic measurement errors. The random errors as a rule are not considerable, and the nature of their appearance cannot be predicted. Instead, the systemic errors are caused by instrumental current and voltage transformers, has permanent nature. Development of Smart Grid networks and digital substations leads to the replacement of analogue measuring systems (CT and VT) with digital ones, combined in a WAMS type system. In such a system, PMUs are connected to optical current and voltage transformers (OCT, OVT) [7]. The main advantages of optical transformers are high accuracy class (0.2, 0.2s) and high resistance to weather conditions. Thus in this paper there was analyzed the influence of measurement errors upon the results of parameter identification methods for the range of errors 0.04-0.2%.

IV. CASE STUDIES

In this section there are represented some case studies to demonstrate accuracy of the obtained results and the effectiveness of proposed methods. The calculations were performed with the help of software complex RastrWin, which ensured the measured values of currents and voltages at both ends of transmission line. For verifying the accuracy of results obtained by the above proposed methods it was used the equivalent scheme of real power line Chishinau-Strasheni 330 kV with the following parameters: conductor 2xACO-300/39, pylon's type – II-330-26 length 41 km.

The parameters calculated from catalogue data of studied line are:

$$R = 2.214 \text{ Ohms}, X = 13.079 \text{ Ohms},$$

$$G = 1.242 \text{ } \mu\text{Sm}, B = 141.04 \text{ } \mu\text{Sm}.$$

There are obtained the results of high accuracy, when transmission line parameters are calculated in accordance

with the formula shown in the section "Short methods description". The percent relative errors are shown in the TABLE I.

TABLE I.

RELATIVE ERROR OF THE RESULTS OBTAINED BY THE METHODS M1-M6

Method	Relative error of			
	$\mathcal{E}_R, \%$	$\mathcal{E}_X, \%$	$\mathcal{E}_G, \%$	$\mathcal{E}_B, \%$
M1	0.017	0.002	0.201	0.106
M2	0.017	0.002	0.193	0.099
M3	0.001	0.003	0.193	0.071
M4	0.017	0.002	0.193	0.099
M5	0.001	0.003	0.193	0.071
M6	0.017	0.002	0.201	0.106

TABLE II shows the percentage change in relative error versus measurement uncertainty.

TABLE II.

RELATIVE ERRORS OF THE RESULTS UPON THE INFLUENCE OF THE MEASUREMENT ERRORS

Method		$\Delta\epsilon\%$							
		+0,04	+0,1	+0,16	+0,2	-0,04	-0,1	-0,16	-0,2
M1	R	2,98	7,44	11,89	14,87	2,98	7,44	11,91	14,89
	X	1,01	2,52	4,04	5,06	1,01	2,52	4,03	5,03
	G	0,07	0,18	0,29	0,36	0,07	0,18	0,29	0,36
	B	0,01	0,04	0,06	0,07	0,01	0,04	0,06	0,07
M2	R	3,11	7,79	12,48	15,61	3,11	7,76	12,4	15,48
	X	1,05	2,64	4,23	5,29	1,05	2,63	4,2	5,25
	G	0,82	2,06	3,29	4,11	0,83	2,07	3,31	4,14
	B	1,36	3,39	5,42	6,77	1,37	3,41	5,46	6,83
M3	R	3,2	7,99	12,76	15,94	3,2	8,02	12,85	16,07
	X	1,05	2,63	4,21	5,27	1,05	2,61	4,18	5,22
	G	0,84	2,11	3,36	4,19	0,84	2,12	3,41	4,28
	B	1,33	3,34	5,34	6,68	1,33	3,34	5,34	6,68
M4	R	3,15	7,88	12,62	15,78	3,15	7,87	12,58	15,71
	X	1,01	2,54	4,06	5,08	1,01	2,53	4,05	5,06
	G	0,86	2,15	3,45	4,31	0,87	2,16	3,46	4,33
	B	1,40	3,49	5,59	6,98	1,40	3,51	5,61	7,02
M5	R	3,24	8,08	12,90	16,11	3,24	8,13	13,03	16,31
	X	1,01	2,52	4,04	5,06	1,01	2,52	4,02	5,03
	G	0,88	2,21	3,52	4,40	0,88	2,22	3,57	4,46
	B	1,38	3,44	5,51	6,89	1,38	3,43	5,49	6,87
M6	R	2,98	7,44	11,89	14,87	2,98	7,44	11,91	14,89
	X	1,01	2,52	4,04	5,06	1,01	2,52	4,03	5,03
	G	0,07	0,18	0,29	0,36	0,07	0,18	0,29	0,36
	B	0,01	0,04	0,06	0,07	0,01	0,04	0,06	0,07

Note: relative errors are calculated in relation to the initial value of the result for each method

In order to compensate errors from current and voltage transformers it is necessary to introduce into the methods of parameter identification the error compensation factor.

V. CONCLUSIONS

This paper demonstrates the classification of the methods of parameter identification for transmission lines based on synchronized measurements obtained in the operation mode. There were represented the most reliable

methods with high accuracy results. Although all methods ensure the percent relative errors less than 1%, methods based on the powers and currents balances are more accurate both in impedance and admittance results of transmission line. Analysis of the change in the calculation results under the influence of the measuring error shows that current and voltage transformers errors can affect considerably the results of calculation. For all methods the active resistance is the most sensitive parameter to measurement errors. The most accurate results are obtained for line admittance when the method of quadripole is used. For the future development and

application of the proposed methods it is necessary to introduce in the calculations the compensation factor of measurement error.

Source of research funding in this article: Research program of the Technical University of Moldova, Chişinău, Republic of Moldova.

Contribution of authors:

First author – 60%

First co-author – 10%

Second co-author – 20%

The third co-author – 10%

Received on July 12, 2020

Editorial Approval on November 25, 2020

REFERENCES

- [1] T.B. Zaslavskaya, M.Y. Irlahman, A.A. Suvorov, V.F. Lovyagin "Limits of variation of electrical parameters of a symmetrical power line," (in Russian), collection of scientific works SibNIE, edition 17, Moscow, RF, , pp. 13-26, 1970
- [2] V.I. Idelchik, A.S. Novikov, S.I. Palamarchuk, "Errors for setting the parameters of equivalent schemes when calculating the regimes of electrical systems", collection "Statistical processing of operational information in electric power systems" Irkutsk, RF, pp. 145-152, 1979.
- [3] A.S. Berdin, P.A. Kryuchkov, A.A. Suvorov, S.N. Sheliug, "Methods of operational identification of parameters of equivalent circuits of electric power systems," (in Russian), proceedings of the Conference of young specialists in power engineering, Moscow, RF, pp. 153-155, 2000.
- [4] I. Stratan, "Characteristics, parameters and equivalent schemes of the elements of the electrical networks," (in Romanian), UTM Edition, Chishinau, Moldova, 2016.-140 p.
- [5] P.I. Bartolomei, A.A. Golikov, A.A. Suvorov, "Determination of the parameters of the equivalent circuit of the electrical network by means of vector registration measurements," (in Russian), Proceedings of the Conference "Power engineering through the eyes of youth". Stavropoli, RF, 2014.
- [6] E. Murdid, I. Stratan, "Parameter Identification of Transformers and Transmission Lines Based on Synchronized Measurements". ANALELE UNIVERSITATII DIN CRAIOVA - Seria Inginerie electrica 2019; 43 (43), pp. 114-121, 2019. ISSN: 1842-4805.
- [7] M.V. Hohlov, "Error in determining the parameters of the power transmission line equivalent circuit using synchronized vector measurements," (in Russian), Proceedings of the Conference "Power engineering through the eyes of youth". Novocheerkassk, RF, 2013.

Metamaterials – Current and Future Trends

Elena Helerea*, Lia-Elena Aciu†

* Transilvania University of Braşov, Braşov, Romania, helerea@unitbv.ro

† Transilvania University of Braşov, Braşov, Romania, lia_aciu@unitbv.ro

Abstract - Recently, metamaterials have attracted considerable attention due to their feasibility and multiple applications. As man-made artificial structures, metamaterials possess properties that are not yet highlighted in the natural world, such as perfect lensing, negative refraction, and backward propagation. These properties are obtained by the proper design of the structure of metamaterials, with the periodic arrangement of unit cells, "meta-atoms", which have dimensions below the order of magnitude of the incident wavelength, at which resonance processes can be established. Thus, the electric and magnetic response of the metamaterial can be flexibly tailored to meet the desired macroscopic properties, in terms of effective electric permittivity and magnetic permeability. In this paper, a review of the state of research and development of metamaterials is made, highlighting the new challenges and ways to improve and to apply these new synthetic structures in electromagnetics and optics. There are analyzed the processes and structures of metamaterials used in various applications. Based on the actual researches, new classification of metamaterials with the criterion of the capabilities and flexibilities in controlling electromagnetic waves is described and analyzed.

Cuvinte cheie: *metamateriale, structuri, proprietăți electromagnetice, clasificări, tendințe.*

Keywords: *metamaterials, structures, electromagnetic properties, classifications, trends.*

I. INTRODUCTION

In the last twenty years, as a result of technological development and the knowledge advancement, new category of synthetic materials has been developed, designed to obtain new, unconventional properties that are not normally found in nature.

Metamaterials provide unusual characteristics, such as negative refraction, perfect absorption or perfect transmission of electromagnetic waves, sub-wavelength resolution imaging, inverse Doppler effect, and backwards propagation [1]-[4].

These characteristics are obtained through the periodic arrangement of unit cells, called "meta-atoms", which have the size smaller than the incident electromagnetic wavelength. Thus, through the flexible and intentional engineering of the structures, dimensions, and arrangement of constituent meta-atoms, electromagnetic metamaterials are able to function as efficient electromagnetic devices to control the amplitude and phase of the electromagnetic (EM) waves so that the response regarding scattering, absorption and dispersion of EM waves can be easily manipulated [2], [5], [6].

Consequently, they have been studied and applied in many areas, as: optics, electromagnetism, electronics, machinery, wireless power transfer systems, acoustics, and communications [7]-[11].

Due to these particular characteristics, metamaterials can be applied in different fields such as: perfect lenses, optical coating, and microwave antenna. Perfect absorber metamaterials that absorb electromagnetic waves can be applied to plasmon sensors, solar cells, photo-detectors, thermal emitters or thermal imagers. By blocking the electromagnetic wave generated in Wi-Fi, mobile phones and home appliances, the absorber metamaterials can protect the body against harmful electromagnetic waves [12]-[16].

Researches in the field of metamaterials have mobilized a wide range of scientific communities, including physics, electrical engineering, materials science, chemistry and mathematics, and have now expanded into the communications society to advance the Internet of Things.

In this paper, a review of the state of research and development of metamaterials is made, highlighting the new challenges and ways to improve and to apply these new synthetic structures in electromagnetics and optics.

The paper provides a more comprehensive understanding of how to design and make metamaterials, highlighting new trends in applications with this category of synthetic materials.

II. METAMATERIAL HISTORY AND TRADITIONAL CLASSIFICATION

The beginning of artificial electromagnetic media can be considered the year 1898, when Sir J. C. Bose published his work on the rotation of the polarization plane through twisted structures created by man.

Then, in the first half of the twentieth century, there were some investigations on obtaining new properties with electromagnetic artificial environments.

In the years 1950s and 1960s, artificial dielectrics were explored for light-weight microwave antenna applications.

Metamaterial structures were first predicted by Veselago in 1968 [17], and the interest in metamaterials was resurrected in the years 1980s and 1990s, with new investigations of microwave radar absorbers for stealth applications.

Since Sir John Pendry proposed to realize negative permittivity using periodic structure of thin wires in 1996 [18], modern metamaterials have received great progress in the past 20 years and are still in the frontiers of physics, chemistry, material, and information societies.

But investigations intensified in the early 2000s when there have been highlighted the opportunities offered by metamaterials for manipulating electromagnetic waves using controlled wave-matter interactions, which sparked a new revolution in materials science and engineering [6]-[8].

Landy in 2008, introduced a new function for metamaterials. He proposed a perfect absorber by utilizing the loss characteristic of the metamaterial substrate. Light weight, low profile and easy fabrication compared to traditional absorbers caused the rapid development of metamaterial perfect absorber, and different applications have been exploited for metamaterial absorbers in various frequency ranges from microwave to terahertz [19]-[21].

Metamaterials consist of ordered repetitive structures called “periodic unit cell” or “cell”. The cell structure, differing in the shape, arrangement, and geometry, manipulates the electromagnetic wave propagation inside the metamaterials. Just like atoms or molecules of natural materials, the structure of the repetitive unit cells determines the properties of the metamaterials [13], [21].

In most cases, the metamaterial consists of a periodic network of identical meta-atoms, analogous to the crystalline structure. Random or irregular arrangements are less often considered and are analogous to the structure of amorphous substances. Consequently, metamaterials represent the second level of structural organization and hence the name of meta (beyond) - materials.

The behaviour of the metamaterial to the action of the incident electromagnetic wave can be described by the material parameters: electric permittivity, respectively magnetic permeability.

But the material parameters depend on the scale on which they are considered [13]:

- If the incident wavelength is much larger than the atomic dimensions and inter-atomic distances, then the atomic behaviour is collective and average material parameters can be introduced, replacing a huge number of separate contributions of the components. In this case, the metamaterials are quite analogous to the conventional ones and the same methods of analysis can be applied;
- When the incident wavelength is comparable to the scale of the dimensions of the structure, complex diffraction and scattering phenomena occur and there is no way to establish the average material parameters. Consequently, in this case, metamaterials can hardly be treated as continuous media;
- For waves with a much smaller length than the size of the constituent elements, the material characteristics are determined by the nature and density of the constituent atoms, with which the electromagnetic quanta interact in a completely independent way. Thus, the concept of metamaterials loses its meaning and can no longer be applied.

Thus, a traditional definition of metamaterials is related to the existence of meta-atoms with dimensions and arrangements of the structure smaller than the incident electromagnetic wavelengths. In this case, the behaviour of the metamaterial can be described mathematically by the effective characteristics of the proposed structure:

$$B_{av} = \mu_0 \mu_{reff} H_{av} \quad (1)$$

$$D_{av} = \varepsilon_0 \varepsilon_{reff} E_{av} \quad (2)$$

where B_{av} is the average magnetic flux density, μ_{reff} is the effective magnetic permeability of the medium, μ_0 is the free space permeability, H_{av} is the average magnetic field

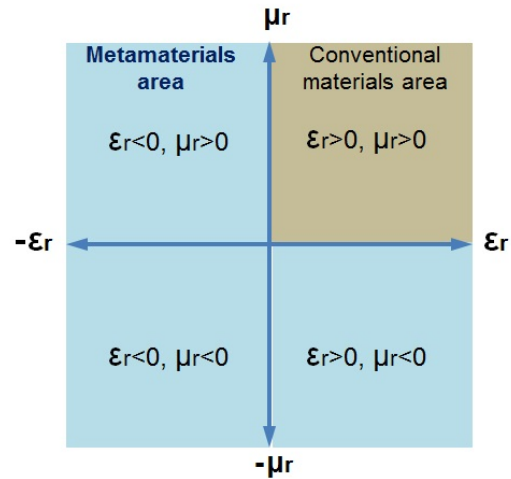


Fig. 1. Traditional classification of electromagnetic materials (after [21])

intensity, D_{av} is the average electric flux density, ε_{reff} is the effective permittivity of the medium, ε_0 is the free space permittivity, and E_{av} is the average electric field intensity.

In general, because H and B , respectively, E and D , are asymmetric and inhomogeneous quantities along the propagation of the resulting electromagnetic wave, the parameters permittivity and permeability will be altered [16].

The concept of simultaneous negative permittivity and permeability was postulated by Veselago in 1968 [7] but it came into existence in 2000 when there was proposed a composite medium based on a periodic array of interspaced conducting nonmagnetic split ring resonators and continuous wires that exhibits a frequency region in the microwave regime with simultaneously negative values of effective permittivity and permeability [9], [22], [23].

Thus, in function of different structure and excitation frequencies, the metamaterials can be with one negative parameter (Fig. 1) or with double negative parameters [21]. In Fig. 1, a conventional classification of the metamaterials is shown, where permittivity and permeability are both positive, this area represents conventional materials area; the other areas, where either one of parameter - permittivity or permeability are negative, or where permittivity and permeability are both negative, represent metamaterial area [21], [24].

The earlier study of metamaterials has focused on homogeneous situations with extreme effective medium parameters (e.g. negative permittivity, negative permeability, and zero index of refraction).

Metamaterials with negative permittivity and negative permeability can be made by properly artificial structures designing, typical being two structures:

- the negative permittivity was achieved by using a periodic thin rod structure;
- the negative permeability was achieved using a periodic split ring resonator structure.

Metamaterials are generally comprised of nano-resonators, scatterers and meta-molecules of different size, shape, geometry, orientation, and arrangement.

In the next section the typical investigations on the structure of metamaterials are reviewed.

III. SPECIFIC CONFIGURATIONS OF METAMATERIALS

Through flexible and intentional engineering of the structures, dimensions, and arrangement of constituent meta-atoms, electromagnetic metamaterials, obtained by structuring natural materials (metals, semiconductors and insulators), are able to function as efficient electromagnetic devices to control the amplitude and phase of the EM wave.

Different configurations of metamaterials have been proposed to meet lots of applications, for wavefront control, and/or for obtaining perfect absorption.

A. Split Ring Resonator Structures

Current research, inspired by Pendry's proposal in the 2000s to make a material with a negative index, has led to the creation of metamaterials with split-ring resonant (SRR) structures [23].

An image of the split ring resonator (SRR) type structure is shown in Fig. 2(a). This is a planar array with a periodic configuration of the unit cells.

The unit cell of the structure consists of a SRR core, made of gold, considered as a perfect electrical conductor in the THz range, provided with a gap-size S . This SRR core is repeatedly arranged on a film fabricated on polyethylene naphthalate with thickness of 100 μm .

The split-ring resonator SRR subwavelength structure acts as an LC resonator circuit with resonance frequency:

$$\omega = \frac{1}{\sqrt{LC}} \quad (3)$$

where inductance L is mainly related to the effective enclosed area of the SRR, and capacitance C is largely determined by the gap size and the surrounding medium.

It can predict that the increase in the gap size g will decrease the capacitance C of the resonator, thus leading to the resonance frequency blue shift. This is observed in Fig. 2(b), in which are simulated the wave transmission in metamaterial samples, with a core size of 40 μm and gap size changing from 4, 6, 8 to 10 μm (SRR 1, 2, 3, and 4).

The authors also propose a SRR hybrid structure consisting of four SRR cells with uniform core length and width, but with different dimensions for the gap antenna. The simulation of wave transmission is shown in Fig. 2(c) and Table I.

TABLE I.
RESONANCE FREQUENCY AND TRANSMISSION

Characteristics	Uniform SRR structure	Hybrid SRR structure
Resonance frequency [THz]	0.83	0.79
Transmission [dB]	-11.1	-39.8

It is observed that the hybrid SRRs structure has a broader and stronger resonance peak as compared with that of the uniform SRR structure. The simulation shows that the increase of the resonator density in each unit cell will determine a broader bandwidth with resonance enhancement.

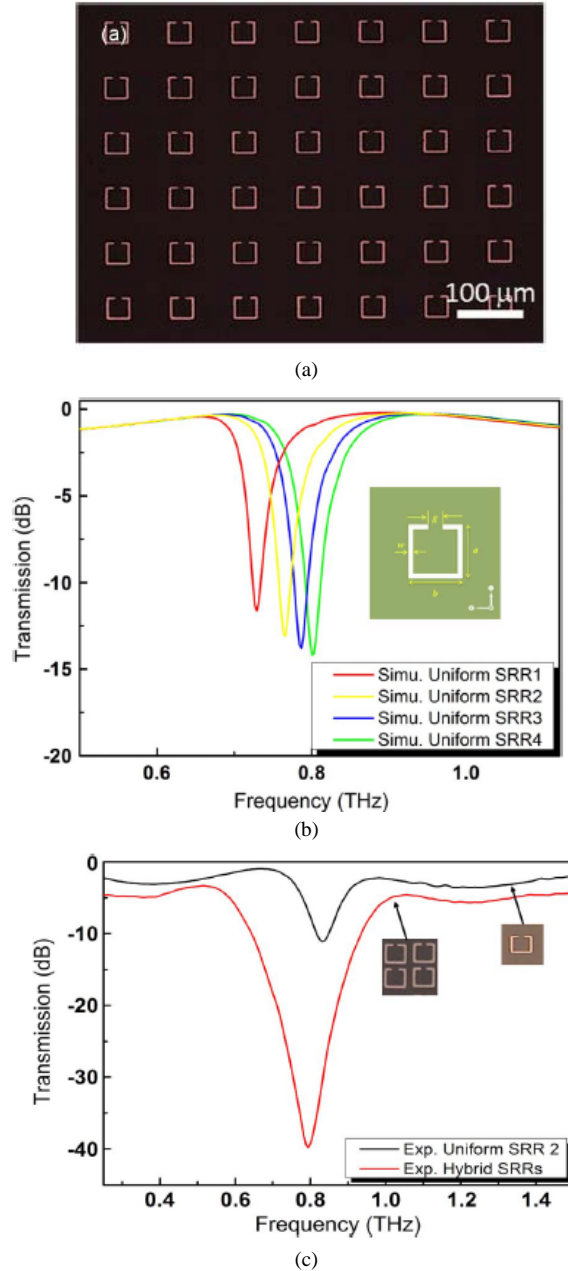


Fig. 2. Microscopic image of the planar array structure (a), simulation of transmission spectra for uniform SRR structures (b), simulation of transmission spectra for the hybrid SRRs sample as compared with uniform SRR structures (after [23])

B. Single and Multi-Layer Structures

Many metamaterial structures have been proposed with strongly multilayer coupled unit cells.

By drastically increasing the effective permittivity by means of intense capacitive coupling and reducing the diamagnetic effect using a thin metamaterial structure, a peak refractive index of 70-80 at the resonance was obtained for a single-layer thin ring terahertz metamaterial.

Thus, in [25] different brick shape metallic patch symmetrically embedded in a dielectric material have been proposed.

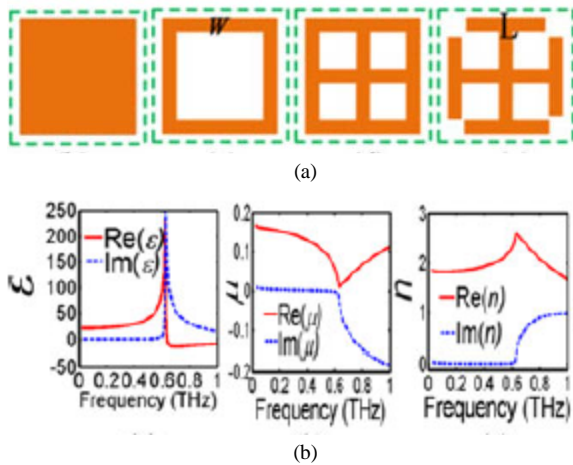


Fig. 3. Unit cell configuration for uniform single layer metamaterial (a), permittivity, permeability and refraction index obtained in THz domain (b) (after [25])

In Fig. 3(a) is shown a top view of the cells of uniform single layer metamaterial, with different cell configurations: thin brick shape metallic patch; thin ring shaped patch; thin window-type; and crossed I-shaped patch, which are symmetrically embedded in a dielectric material. By experimental and theoretical investigations, the authors demonstrated a polarization-dependent and anisotropic extremely high index of refraction in the terahertz region.

The case analyzed by the authors is that of a simple cubic array structure of metal cubes with the period of array about $p = 60 \mu\text{m}$, which is much smaller than the wavelength of electromagnetic waves in THz (which is about $\lambda = 300 \mu\text{m}$). Thus, the repetition period of the array is sub-wavelength relative to the incident electromagnetic wave. Because these cubic arrays have bulk properties when the distance between the elements is much less than the incident wavelength, it is possible to extract their effective constitutive parameters. Different methods are applied to retrieve the constitutive parameters of metamaterial: by numerically calculating the ratios of the electromagnetic fields, by some approximate analytical models or by using the reflection and transmission coefficients (S parameters).

In Fig. 3(b) for this simple cubic array, the dependence of the real and imaginary parts of permittivity ϵ_r , permeability μ_r and index of refraction n on the frequency in the THz domain, extract with method of transmission coefficients, is shown.

Having in view that the electromagnetic properties of this structure is isotropic permittivity and permeability are scalar quantity and have been extracted with relationships:

$$\epsilon_r = n \cdot \frac{z_0}{z(\omega)} \quad (4)$$

$$\mu_r = n \cdot \frac{z(\omega)}{z_0} \quad (5)$$

$$n(\omega) = \sqrt{\epsilon_r(\omega) \cdot \mu_r(\omega)} \quad (6)$$

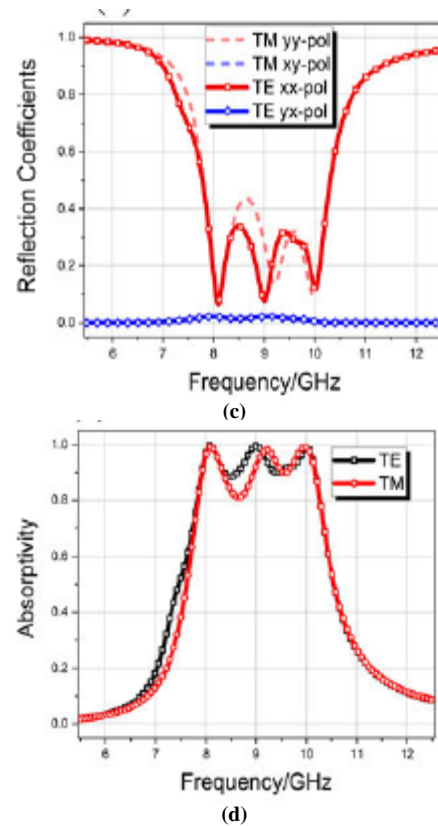
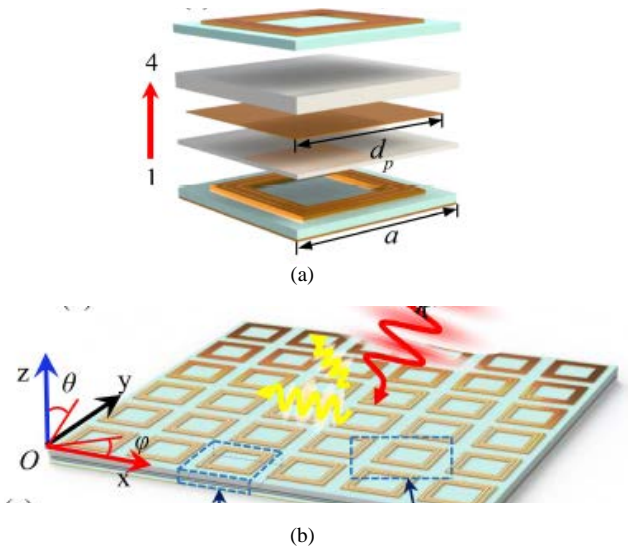


Fig. 4. The structure of unit cell for multilayer hybrid metamaterial structure (a), sample view of multilayer hybrid metamaterial structure (b), numerically simulation of the reflection coefficient (c) and absorption (d) of the metamaterial in Te and TM excitations (after [24]).

where $z(\omega)$ is structure impedance and z_0 is the impedance of free space. The specific values obtained and shown in Fig. 3(b) are: $\epsilon_{\text{max}} = 250$; $\mu < 0.16$ and $n < 2.5$ for resonance frequency $f_{\text{rez}} = 0.6 \text{ THz}$.

To increase the performances of EM wave control, many multilayer hybrid structures have been proposed [24]. In Fig. 4(a), spatial detailed cell geometry in a vertical expanded view of a multilayer hybrid structure is shown. Unit cell is comprised of a back metal layer of full copper foil, an insulator layer of Rogers 5880, a five-metal resonant square-loop, a flexible adhesive layer of

PDMS, a sputtered aluminium layer, another PDMS layer, and a flame-retardant FR4 layer.

The overall prototype consists of 15 x 15 cells of elements, with a 12 x 12 cm² area, as shown in Fig. 4(b).

For this multi-layer metamaterials, the authors [24] considered the correlations between layer thicknesses, bandwidths, absorptions, and the composite-substrate thickness in determination of the device flexibility.

The absorption level of the metamaterial can be represented as:

$$A(\omega) = 1 - R(\omega) - T(\omega) \quad (7)$$

where $R(\omega)$ and $T(\omega)$ are the reflectivity and transmittance of the EM wave, respectively. $T(\omega)$ is close to zero when the back of the metamaterial is metallic foil, so the absorption is related only to the reflection coefficients.

The proposed structure presents many bandwidth and absorptivity advantages.

As observed in the reflection-coefficient characteristics at a working band range of 5.5-12.5 GHz, shown in Fig. 4(c), the trends are in connection with the absorbing energy transformation. The anisotropy of different materials at high frequencies leads to tight deviations, and reflection-coefficient in the cross-polarization direction converge nearly to zero, which indicates that the EM wave was absorbed by the proposed structure, rather than the wave transformation.

The absorptivity of the proposed metamaterial is shown in Fig. 4(d), when TE (transversal electric mode of excitation) and TM (transversal magnetic mode of excitation) waves normally propagate to the proposed structure. The absorption in the TE and TM incident waves is almost uniform, and only a slight discrepancy is observed at 8.8 GHz because the electric-dipole absorption is stronger than the magnetic absorption of the multi-layer structure.

C. Multi-Layer Metamaterials with Graphene

Recent, different configurations of absorbers are proposed using the advantages of graphene, to have the band gap of greater than 0.5 eV, which facilitate the applications with tunable sub-wavelength devices [26]-[29].

Thus, in [26] there are proposed dual band absorbent structures, insensitive to polarization, in the THz domain, which are based on the unit cell of the graphene / SiO₂ / Au.

The structures shown in Figs. 5(a) are composed of a graphene layer, of different shapes (cross-shaped, disk or combined shape), which is placed on top of a gold layer, separated by a thick layer of SiO₂. The bottom Si substrate is used to protect the entire structure against mechanical damage.

For Structure I, in Fig. 5(b) it can be seen that for wavelength range from 30 to 100 μm, at normal incidence of EM wave, there are two higher absorption peaks in the considered wavelength range, but they cannot reach nearly unity at the same time. With the increasing of the wing length S , the long wavelength absorption peak is firstly blue-shifted and then red-shifted, and the change trend of the short wavelength absorption peak is just opposite.

For the case of Structure II shown in Fig. 5(c), one can see that there is only one absorption peak, and the spectral line has an obvious red-shift with the increasing of radius r .

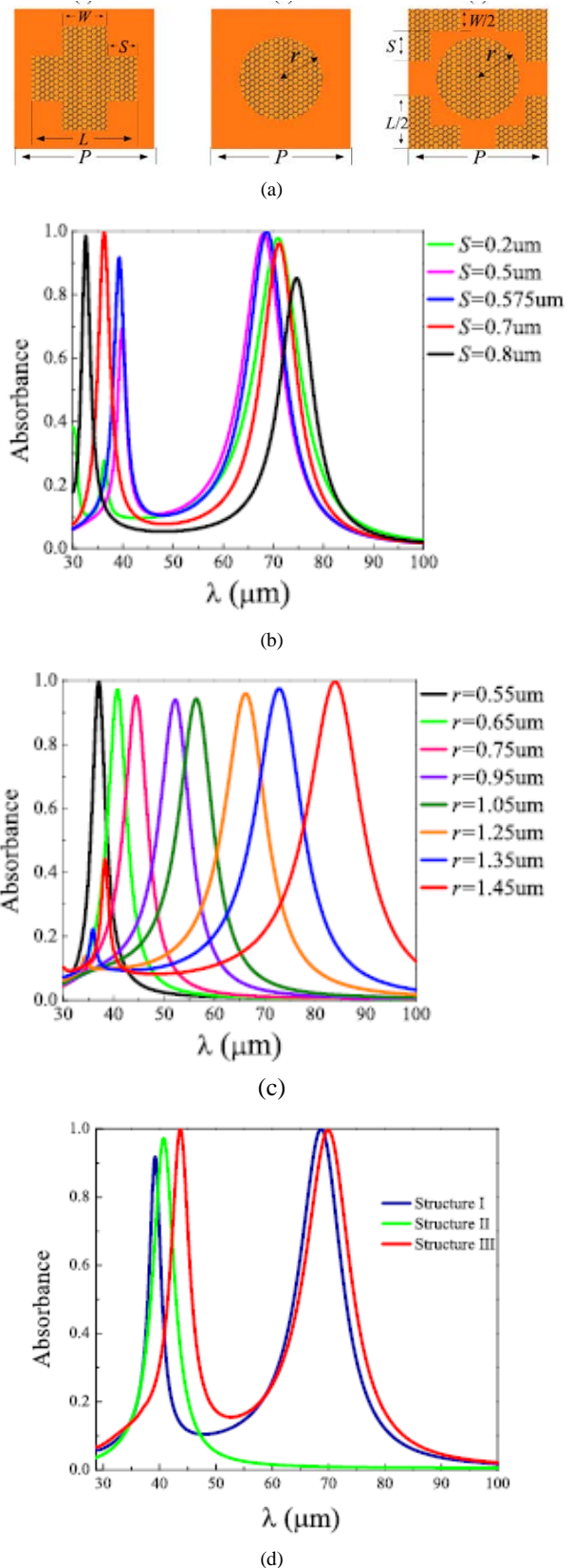


Fig. 5. Proposed multi-layer structures with cross-shaped graphene (Structure I), disk-shaped graphene (Structure II), and both cross- and disks shaped graphene (Structure III) (a), Absorption spectra of Structure I for the different wing length S (b), Absorption spectra of Structure II for different radius r (c), Absorption spectra in the wavelength range from 30 to 100 μm at normal incidence, for the Structures I, II and III (after [26])

The authors proved that by combination of these structures, one can obtain two absorption peaks occurring at $\lambda = 69.94$ and $43.747\mu\text{m}$ in the absorption spectrum, with the absorbance of the two peaks close to 100%. The optimal geometry parameters are $L = 2.35\ \mu\text{m}$, $S = 0.575\ \mu\text{m}$, and $r = 0.65\ \mu\text{m}$, and other parameters are the same as those in the figures above.

D. Multi-Layer Multi-Functional Metamaterials

A lot of investigations proposed the composite multi-layer structures of metamaterials which have two operation functions, for instance, to assure the transparency to visible light and absorbance [20], [30] or application as absorber and polarization converter [5], [21].

Many papers proposed multi-layer structures which include vanadium dioxide (VO_2) which undergoes a structural transformation from a monoclinic phase to a tetragonal phase around 340 K. Through the phase transition, the conductivity and permittivity of VO_2 vary significantly, which can be applied to control the electromagnetic properties of metamaterial structures.

Phase transition in VO_2 can be caused by external electrical, optical, or thermal excitation.

In [5], the proposed structure of the layers includes: VO_2 disks, silica (SiO_2) layer, VO_2 film, metallic strip, SiO_2 layer, and a metallic film (Fig. 6(a)). The dimensions are of order of micrometers, and repetition period is $P = 40\ \mu\text{m}$.

In this case, the thermal excitation is used.

- When VO_2 is in the metallic state (at the room temperature of 20°C), the designed configuration behaves as a perfect single-band absorber based on two-dimensional arrays of VO_2 disk on a VO_2 film. The performance of absorption is polarization-insensitive and angle-independent (Fig. 6(b));
- When VO_2 is in the insulating state (over the phase transition point of 68°C), the designed configuration behaves as an efficient cross polarization converter working in the reflective mode at terahertz frequencies. It can convert a linear-polarized wave to its orthogonal direction. Because of the subwavelength size of the unit cell, the efficiency of cross polarization is higher than 90% from 2.0 THz to 3.0 THz under normal incidence (Fig. 6(c)).

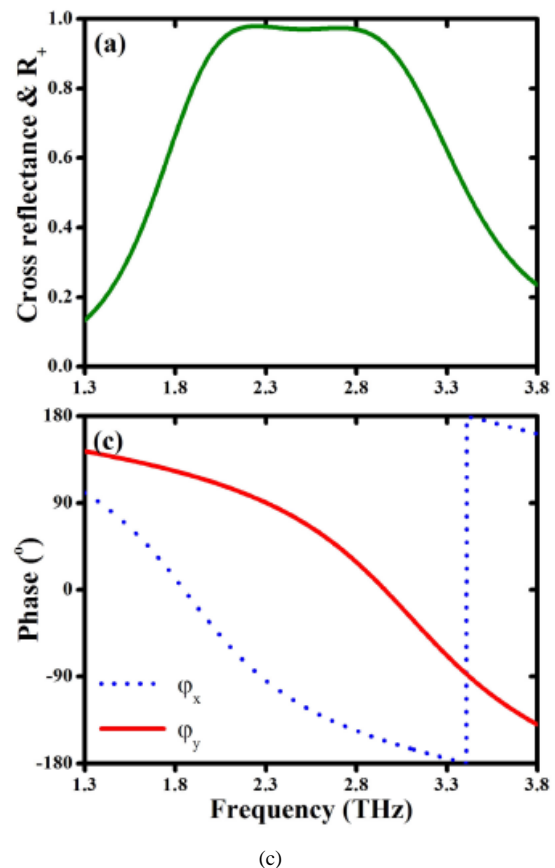
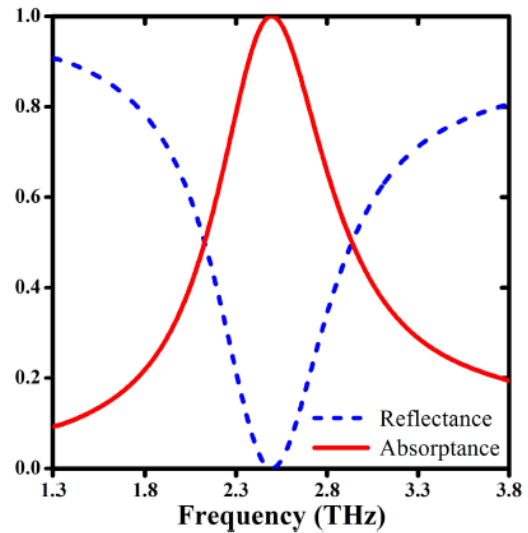
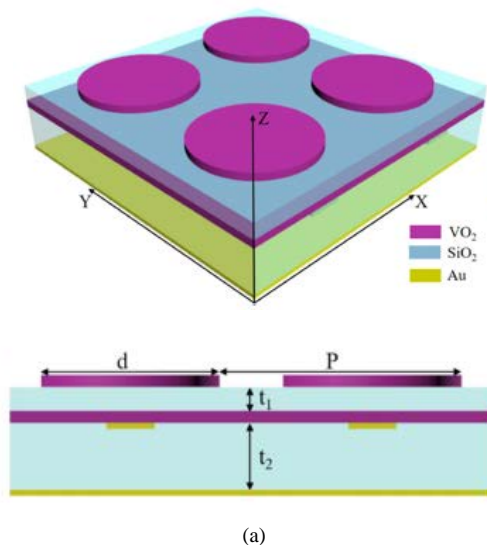


Fig. 6. Geometric parameters of the structure with VO_2 (a); Simulated reflectance and absorbance under normal incidence at normal temperature (b); Reflectance of cross-polarized wave and phases for x and y-polarized waves. The incident electric field is decomposed into two orthogonal components along the x- and y-axes and reflected electric field is rotated by 90° (c) (after [5]).

Another two-functional structure of metamaterial based on VO_2 is proposed in [21], which allow obtaining a broadband switchable absorber.

The composite resonant structure consists of a criss-cross structure and four square patches of tantalum nitride (TN), with thickness of $21\ \mu\text{m}$, a multi-layer dielectric plate (foam layer, VO_2 layer, SiO_2 layer), and a gold ground plane.

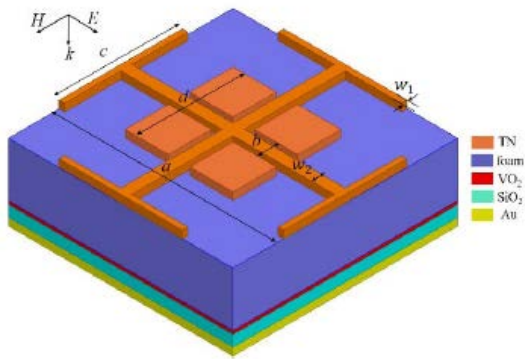


Fig. 7. Schematic of unit cell of the switchable broadband absorber (after [21])

The switch function is realized by controlling the operation temperature, and the absorber can be switched in a broadband ranging from 0.32 THz to 0.56 THz to another broadband ranging from 0.356 THz to 0.682 THz with an absorptivity of over 90%.

IV. NEW STEPS IN METAMATERIAL DEVELOPMENT

Research to date has shown that metamaterials have great capability and flexibility in controlling electromagnetic waves, because their subwavelength meta-atoms can be designed and customized in the desired ways.

But, for the metamaterials presented so far, it is characteristic that once manufactured, these metamaterials will have fixed functions, i.e. they are passive metamaterials [31].

In order to dynamically control the EM waves, several ways have been proposed, among which, the integration in meta-atoms of different active devices, so that active metamaterials have been obtained.

Recently, a special kind of active metamaterials - digital coding and programmable metamaterials - has been proposed, which can realize a large number of distinct functionalities and switch them in real time with the aid of field programmable gate array (FPGA).

In Fig. 8 the steps of metamaterial development are pointed, having in view the capabilities and flexibilities in controlling electromagnetic waves.

From the perspective of achievable functions, the first step was the development of passive metamaterials, composed of structures specially designed in periodic or non-periodic arrays of sub-wavelength unit cells, to obtain homogeneous or inhomogeneous material parameters that do not exist in nature or are difficult to achieve in practice. Numerous structures of passive metamaterials have been proposed, in the 3D version and in the 2D version, with applications in microwave and optical frequency bands. But, the disadvantage of passive metamaterials is that, once these structures are manufactured, their functionality will be fixed, without being able to react dynamically to the action of incident waves.

The second step in the development of metamaterials to achieve dynamic control of electromagnetic waves was the fabrication of the active metamaterials, by integrating active devices.

In the active metamaterials, the unit cells consist of meta-atoms and active devices (e.g. PIN diodes, varactors, amplifiers, semiconductors, micro-fluids, and VO₂) to their EM responses under the external excitations.

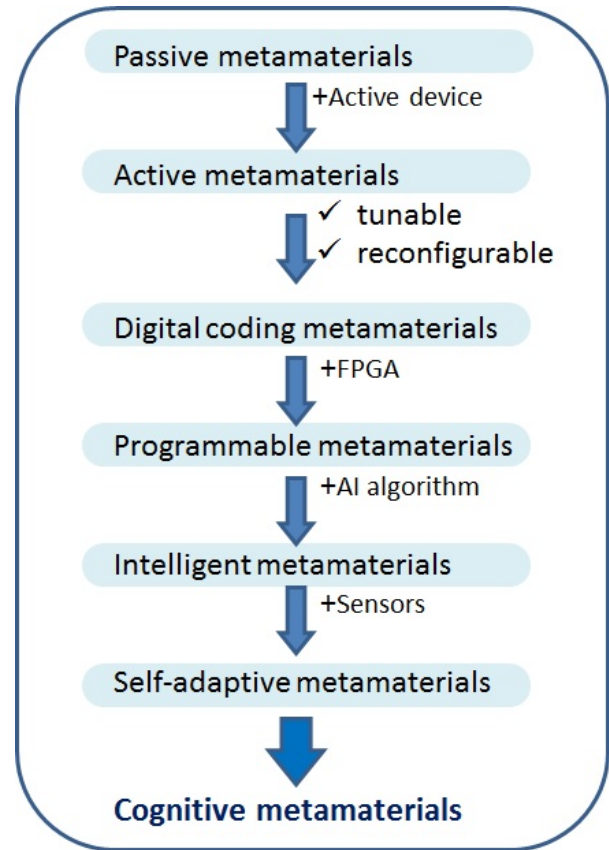


Fig. 8. Steps of metamaterial development (processed after [31])

Traditionally, the active metamaterials include tunable metamaterials and reconfigurable metamaterials (Fig. 8). The tunable metamaterials usually realize similar functions (such as shifting the resonance peaks and perfect absorptions) by tuning the active devices. For reconfigurable metamaterials, which can have significantly different functions (such as changing polarization states and working bandwidth control) by switching active devices, the number of functions is very limited.

The third stage of metamaterial developments is that of digital metamaterials, obtained by representing the digital coding of meta-atoms [24], [31]. By integrating the digital coding metamaterial with the field programmable gate array (FPGA) a programmable metamaterial is obtained.

The development of metamaterials which are programmable in the field is a major breakthrough in the development of metamaterials, as a single programmable metamaterial can perform many distinct functions (eg, single-beam radiation, different multi-beam radiation, beam scanning, wave diffusion, vortex beam generation etc.). All these functions are switched in real time by changing the digital states and sending the instructions by the FPGA.

Thus, the introduction of digital code representation of metamaterials makes it possible to connect the digital world with the physical world, so that metamaterials process digital information directly, resulting in informational metamaterials.

New steps are predicted by applying artificial intelligent (AI) and including specific sensors to obtain intelligent metamaterials, self-adaptive metamaterials and the highest level of cognitive metamaterials.

There are already a multitude of applications, from which three areas are well developed: in optics (for birefringence modification), in wireless power transfer (to increase the efficiency of power transfer), and in the realization of electromagnetic absorbers in the THz domain (to increase the absorption coefficient close to 100%).

V. CONCLUSIONS

The field of metamaterials has been progressing rapidly in the past years, showing that the conventional limitations of modern technologies can be overcome using the advanced knowledge in electromagnetism and in nanofabrication techniques.

The traditional metamaterial classification, with the criterion of the values of permittivity and permeability, is no longer sufficient. Current advances in the field have imposed the new classification of metamaterials in which the criterion of capability and flexibility of dynamic control of electromagnetic waves is considered.

Thus, depending on the types of functionalities that can be achieved, metamaterials are classified into passive and active metamaterials. Active metamaterials can be tunable and reconfigurable. Some active metamaterials are programmable and, by adding the appropriate software, could become information metamaterials.

Advances in understanding the processes that take place in metamaterials, and progress in their realization with modern micro- and nano-technologies show that nowadays the characteristics of these synthetic materials for realization of new generation of communication systems are possible to be explored.

Source of research funding in this article: Research program of the Transilvania University of Braşov.

Contribution of authors:

First author – 70%

First co-author – 30%

Received on June 25, 2020

Editorial Approval on November 02, 2020

REFERENCES

- [1] J. Zhang, J. Tian, and L. Li, "A Dual-Band Tunable Metamaterial Near-Unity Absorber Composed of Periodic Cross and Disk Graphene Arrays," *IEEE Photonic Journal*, vol. 10, 2, April 2018.
- [2] W. Wang, F-P. Yan, S-Y. Tan, H-S., et al., "Numerical Analysis of Magnetic Plasmonic Resonance Modes in Three-Dimension Split Ring Resonator Metamaterials," *IEEE Photonics Journal*, vol. 11, 4, 2019.
- [3] W. Ai, P. Zhou, R. Sun, Y. Liu, et al., "Control of Resonance Absorption Modes for Broadband Infrared Metamaterial Absorber," *IEEE Photonic Journal*, vol. 11, 1, February 2019.
- [4] A. Hoque, M. T.ariqul Islam, A.F. Almutairi, et al., "SNG and DNG meta-absorber with fractional absorption band for sensing application," *Scientific Reports*, 10 (1), art. 13086, 2020.
- [5] M. Zhang, J. Zhang, A. Che, and Z. Song, "Vanadium Dioxide-Based Bifunctional Metamaterial for Terahertz Waves," *IEEE Photonics Journal*, vol. 12, 1, 2020.
- [6] Z. Yangjian, F. Chuhuan, L. Qi, S. Xin, and Y. Hongbin, "Dynamic Reflection Phase Modulation in Terahertz Metamaterial," *IEEE Photonics Journal*, vol. 11, 4, 2019.
- [7] H. Kwon, D.L. Sounas, A. Cordaro, A. Polman, and A. Alù, "Nonlocal Metasurfaces for Optical Signal Processing," *Physical Review Letters*, vol. 121, 17, 173004, October 24, 2018.
- [8] B. Gao, M.F. Yuen, and T. Ye, "Ferrite Film Loaded Frequency Selective Metamaterials for Sub-GHz Applications," *Materials*, vol. 9, 1009, 2016.
- [9] R. Deng, M. Li, B. Muneer, et.al., "Theoretical Analysis and Design of Ultrathin Broadband Optically Transparent Microwave Metamaterial Absorbers," *Materials* vol. 11, 107, 2018.
- [10] Y. Cho, S. Lee, D-H Kim, H. Kim, et.al., "Thin Hybrid Metamaterial Slab With Negative and Zero Permeability for High Efficiency and Low Electromagnetic Field in Wireless Power Transfer Systems," *IEEE Transactions on Electromagnetic Compatibility*, vol. 60, 4, pp. 1001-1009, August 2018.
- [11] D.C. Brooke, O. Umnova, P. Leclaire, and T. Dupont, "Acoustic metamaterial for low frequency sound absorption in linear and nonlinear regimes," *Journal of Sound and Vibration*, 485, 115585, 2020.
- [12] F. Costa, and A. Monorchio, "Multiband electromagnetic wave absorber based on reactive impedance ground planes," *IET Microw. Antennas Propag.*, vol. 4, 11, pp. 1720–1727, 2010.
- [13] A. Dubey, and T.C. Shami, "Metamaterials in Electromagnetic Wave Absorbers," *Defence Science Journal*, vol. 62, 4, pp. 261-268, July 2012.
- [14] D. Hu, H-Y. Wang, and Q-F. Zhu, "Design of Six-Band Terahertz Perfect Absorber Using a Simple U-Shaped Closed-Ring Resonator," *IEEE Photonics Journal*, vol. 8, 2. 2016.
- [15] H. Liu, K. Luo, S. Tang, et al., "An Ultra-Wideband THz/IR Metamaterial Absorber Based on Doped Silicon," *Materials*, 11, 2590, 2018.
- [16] M. Amiri, F. Tofigh, N. Shariati, J. Lipman, and M. Abolhasan, "Wide-angle metamaterial absorber with highly insensitive absorption for TE and TM modes," *Scientific Reports* 10 (1), art. no. 13638, 2020.
- [17] V.G. Veselago, "The electrodynamics of substances with simultaneously negative values of permittivity and permeability." *Sov. Phys. Uspekhi*, 1968, 10, 509–514.
- [18] J.B. Pendry, A.J. Holden, W.J. Stewart, I. Youngs, "Extremely low frequency plasmons in metallic mesostructures." *Phys. Rev. Lett.*, 76, 4773–4776, 1996.
- [19] N.I. Landy, et al., "Perfect Metamaterial Absorber." *Phys. Rev.Lett.*, 100.20, 207402, 2008:
- [20] G. Deng, Y. Lu, Z. Yin, et.al., "A Tunable Polarization-Dependent Terahertz Metamaterial Absorber Based on Liquid Crystal," *Electronics*, vol. 7, 27, 2018.
- [21] H-E. Su, J-L. Li, and L. Xia, "A Novel Temperature Controlled Broadband Metamaterial Absorber for THz Applications," *IEEE Access*, vol. 7, 2019.
- [22] Y. Hollander, ant R. Shavit, "Constitutive parameter extraction and experimental validation of single and double negative metamaterials," *IET Microw. Antennas Propag.* vol. 5, 1, pp. 84–94, 2011.
- [23] Z.Y. Pan, P. Zhang, Z.C. Chen, G. Vienne, and M.H. Hong, "
- [24] J. Cui, H. Xu, X. Yu, G. Shao, and H. Sun, "A Novel Encoding Strategy of Enhanced Broadband and Absorption Conformable Metamaterial for MW Applications," *IEEE Access*, vol. 8, pp. 100458-100468, 2020.
- [25] X. Jing, X. Gui, R. Xia, and Z. Hong, "Ultrabroadband Unnaturally High Effective Refractive Index Metamaterials in the Terahertz Region," *IEEE Photonics Journal*, vol. 9, 1, 5900107, 2017.
- [26] J. Zhang, J. Tian, and L. Li, "A Dual-Band Tunable Metamaterial Near-Unity Absorber Composed of Periodic Cross and Disk Graphene Arrays," *IEEE Photonic Journal*, vol. 10, 2, April 2018.
- [27] H. Liu, K. Luo, S. Tang, et al., "An Ultra-Wideband THz/IR Metamaterial Absorber Based on Doped Silicon," *Materials*, 11, 2590, 2018.
- [28] K.T. Lin, H. Lin, T. Yang, and B. Jia, "Structured graphene metamaterial selective absorbers for high efficiency and omnidirectional solar thermal energy conversion," *Nature Communications*, 11:1389, 2020.

- [29] M. Biabanifard, A. Arsanjani, M.S. Abrishamian, and D. Abbott, "Tunable Terahertz Graphene-Based Absorber Design Method Based on a Circuit Model Approach," *IEEE Access*, vol. 8, 2020.
- [30] T. Liu, and S.S. Kim, "Ultrawide Bandwidth Electromagnetic Wave Absorbers Composed of Double-Layer Frequency Selective Surfaces with Different Patterns," *Scientific REporTS*, 8:13889, 2018.
- [31] T.T. Jun Cui, "Information Metamaterial Systems," *iScience*, 23, 101403, August 21, 2020.
- [32] J. Shabanpour, S. Beyraghi, and H. Oraizi, "Reconfigurable honeycomb metamaterial absorber having incident angular stability," *Scientific Reports*, 10:14920, 2020.

Virtual Instrumentation for Study of Shape Memory Alloys Strip while Bending

Gheorghe-Eugen Subțirelu*, Sonia Degeratu*

*University of Craiova/Department of Electromechanics, Environment and Applied Informatics, Electrical Engineering Faculty, Craiova, Romania, esubtirelu@em.ucv.ro, sdegeratu@em.ucv.ro

Abstract - In this paper, using LabVIEW graphical programming environment and the portable reconfigurable input/output (RIO) device from National Instruments (myRIO-1900), the concept of virtual instrumentation is implemented. Thus, it is created a hardware and software system that is used to study the nickel and titanium shape memory alloy (NiTi SMA) strip during bending under the influence of electric current. The SMA strip is caught in cantilever mode (fixed at one end only). For this study, the following quantities are measured: the deformation of the strip (using a created electronic transducer around an operational amplifier and a piezoelectric effect sensor), the voltage applied to its ends and the current flowing through it (with LEM transducers). The evolution of the electrical resistance as well as the bending of the SMA band at different values of the electric current, during and due to the heating process is reported using this system. The values of the measured quantities are presented in graphical and numerical form. Thus, the evolution on time intervals of the order of seconds can be followed with precision with the help of horizontal and vertical cursors, respectively. Amplitude values can also be accurately determined. The results obtained with the proposed system are useful in practical applications of cantilever SMA strip for development of simple, more compact and reliable actuators or sensors.

Cuvinte cheie: *aliaje cu memoria formei, bandă fixată la un singur cap, instrumentație virtuală, senzor piezoelectric, transductor de deformare cu înaltă sensibilitate.*

Keywords: *shape memory alloy, cantilever strip, virtual instrumentation, piezoelectric sensor, highly-sensitive deflection transducer.*

I. INTRODUCTION

Shape Memory Alloys (SMA) or NiTi SMA (Nickel and Titanium or named Nitinol after the name of the components) are materials capable of remembering a previously memorized shape and exert a useful force or support very high deformations, thanks to their super elasticity properties [1-2].

Today, the use of shape memory alloys for the actuator is a technological opportunity for the development of these electromechanical components: the typical feature of the shape memory alloy strip to provide mechanical action, if stimulated by electricity (and heat) allows the development of more compact devices with light weight and small size [3-5], [8].

These devices will replace alternative technologies based on electric motors, solenoids and relays in automotive industry, healthcare, security and defense, consumer electronics, home appliance, damping systems, robotics.

A full range of SMA actuators advantages are: reduced cost, direct linear or angular movement, noiseless operation, compatibility with harsh environments, no electromagnetic emission.

In the last three decades, the community of researchers and engineers in the field of materials study has shown a significant interest in discovering, understanding and applying the characteristics of SMA.

The result of this intense interest and effort has materialized in numerous publications in the form of books, journal articles and volumes of international scientific events [7], [10-11].

To study the characteristics of the SMA (for example, to investigate by differential scanning calorimetry method during the heating-cooling process) and to extract its most important thermal parameters to correlate them with the evolution over time of other mechanical or electrical parameters, high-performance equipment is used [12-14].

Virtual Instrumentation (VI) can be a good solution in this field too due to its flexibility, performance and costs. In VI, with the help of a suitable hardware platform (built around a data acquisition module) we can easily create our own workspace with all the necessary tools for study of SMA characteristics. We can use VI to bring the facility of flexible software (LabVIEW) and personal computer technology to design applications making accurate measurements. The measurement system is controlled from a computer and data collected and analyzed are presented on a display screen [6], [21].

In the recent paper [9], it is shown how to evaluate the thermal characteristics of the SMA strip by using the differential scanning calorimetry (DSC) experiments. The results of this thermal analysis were the basis for determining the force developed by the SMA strip during the phase transformation. Evolution of the electrical SMA resistance at various values of the activation current is also studied.

In that work there are hints about hardware component of experimental platform but no explicit diagram details are presented. Our goal is to describe them in detail in the present paper.

II. HARDWARE PLATFORM

An experimental platform which uses a flexible piezoelectric effect film sensor for estimate of SMA strip deforming and a portable reconfigurable input/output (RIO) device for the measurement and rapid analyzing of parameters has been developed.

Fig. 1 shows block diagram of the experimental platform designed for study of SMA strip characteristics.

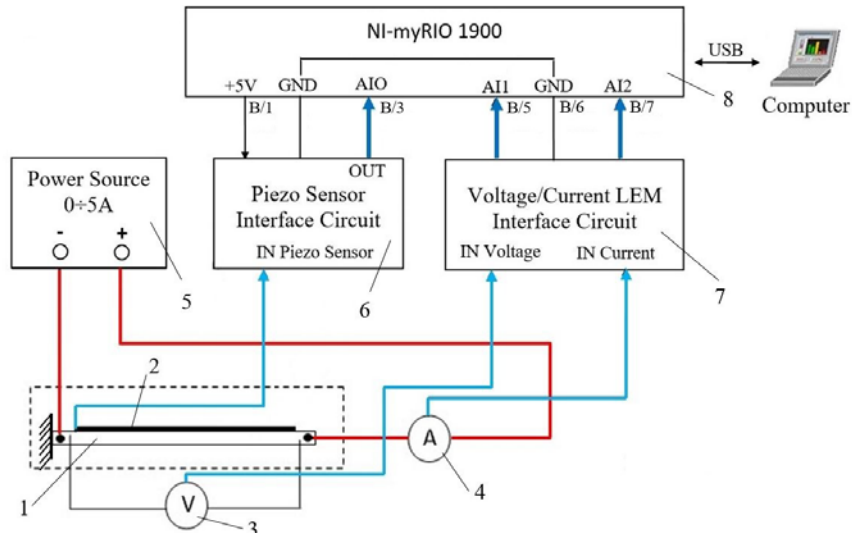


Fig. 1. Block diagram of the experimental platform for control and data acquisition during a displacement of the SMA strip.

The main components of proposed experimental platform are: SMA cantilever strip (1) under test, with piezoelectric sensor (2); voltage (3) and current (4) LEM transducers; power current source (5); piezoelectric sensor interface circuit (6); conditioner circuit for the voltage/current LEM transducers (7); data acquisition (DAQ) module (8) and computer (9). All these elements will be presented in detail.

A nickel-titanium shape memory strip with rectangular cross section (2.5×0.5 mm) was used in this study. The SMA strip was purchased under the name FLEXINOL® from DYNALLOY, Inc. [15]; Flexinol is a trade mark of Dynalloy, Inc., Irvine, California, USA, brand of NiTi shape memory alloy wire or strip [16].

The power supply (5) is a variable direct current source with stable output, available for testing requirements. Current and voltage wires are securely fastened to the SMA strip with small screws.

A flexible piezoelectric sensor (2) was used to control the deformation and movement of the SMA cantilever strip. The sensor is glued to the entire surface of the SMA strip.

Fig. 2 shows a close-up (in top and side view) of the tested SMA cantilever. The connection mode between SMA strip and current source, respectively the LEM current / voltage transducers is shown in the figure. It is also observed how to fix the piezo sensor foil on the SMA strip surface.

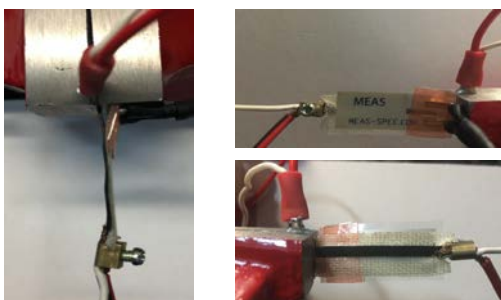


Fig. 2. Image of cantilever SMA strip (detail)

The acquisition of the data necessary for the proposed study is done with the help of NI myRIO - 1900 (8).

This device takes from the experimental platform signals in the form of voltage proportional to: SMA strip deformation (measured with the piezo transducer); the current flowing through the SMA strip and the voltage drop at its ends, respectively (measured with LEM transducers); the maximum length for signal wires is 30 cm.

The NI myRIO-1900 provides analog input (AI), analog output (AO), digital input and output (DIO), audio, and power output in a compact embedded device. The NI myRIO-1900 connects to a host computer over USB cables.

NI myRIO-1900 expansion port (MXP) connectors A and B carry identical sets of signals. The signals are distinguished in software by the connector name (i.e., as in Connector A/DIO1 and Connector B/AIO1).

The analog inputs are multiplexed to a single analog-to-digital converter (ADC) that samples all channels. The resolution of the ADC converter is 12 bits and the value in volts of the increment between data values is 1.221 mV if we use device to measure 0-5 V signals. Some other technical specifications: processor type Xilinx Z-7010 with 2 cores; speed 667 MHz; memory nonvolatile 512 MB and DDR3 256 MB; analog input sample rate 500 kS/s [22].

The image of all connections to NI myRIO MXP connector B, is shown in figure below.

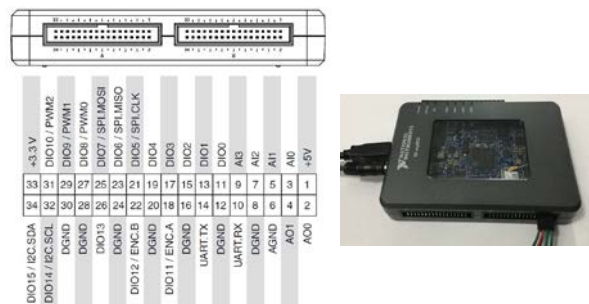


Fig. 3. Image of connections to NI myRIO MXP connector B, power input cable and USB cable

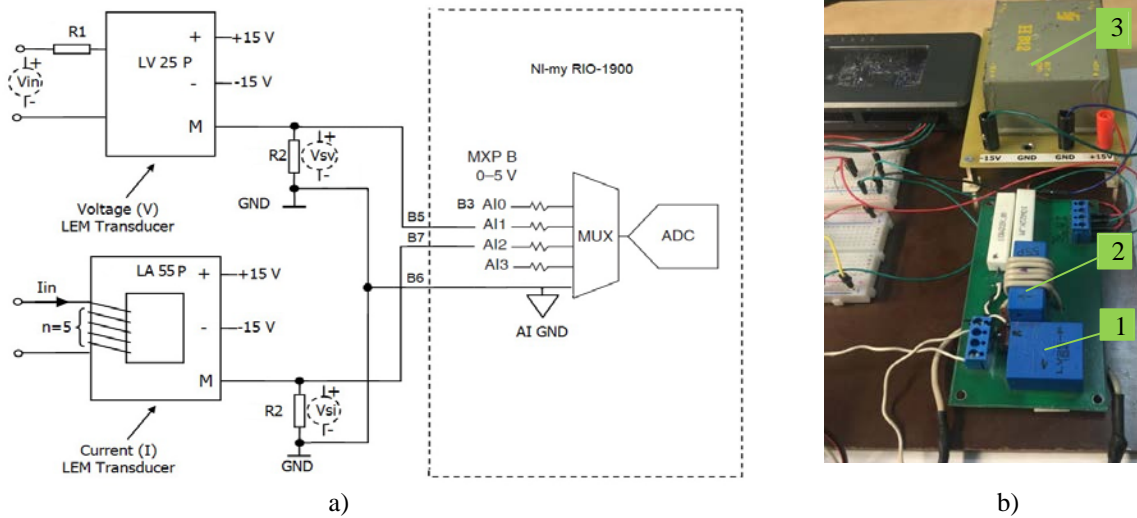


Fig. 4. Voltage/current LEM interface: a) schematic diagram and b) top view image

Fig. 4 shows how to connect and power of LEM transducers and their interface circuit with NI myRIO device connectors (see also Fig. 1 and Fig. 3).

The V_{SV} and V_{Si} voltage signals (with values dependent on the SMA strip voltage V_{in} and the current through it I_{in}) connect to two analog inputs of the MXP Connector B (B5/AI1, B7/AI2).

Primary resistor $R1$ of the voltage LEM transducer (position 1) should be calculated so that the nominal voltage had to be measured corresponds to a primary current of 10 mA. Measuring resistances $R2$ of transducer is dependent on the values of primary nominal current.

Current LEM transducer dynamic performance is the best with a single bar completely filling the primary hole; to increase the sensitivity of the sensor to low values of the measured current, several winding turns are given, $n = 5$ (position 2 in Fig. 4, b).

LEM transducers are powered by a dual source voltage ± 15 V relative to GND (position 3 in Fig. 4, b).

The voltage transducer used is LV-25P and the current transducer type is LA-55P; both are LEM [17].

Piezoelectric effect is the ability of certain materials to generate an electric charge in response to applied mechanical stress. When piezoelectric material is placed under mechanical stress, a shifting of the positive and negative charge centers in the material takes place, which then results in an external electrical field.

A piezoelectric sensor in combination with an electric charge to voltage converter make up the transducer that is used to estimate the deformation and displacement of the SMA strip under the influence of the current flowing through it.

The DT series of piezo film sensor elements are rectangular elements of piezo film with silver ink screen printed electrodes from TE Connectivity (TE); sensor capacitance is $C_s = 1.38$ nF [18].

Schematic diagram and breadboard layout of piezo transducer is shown on Figure 5.

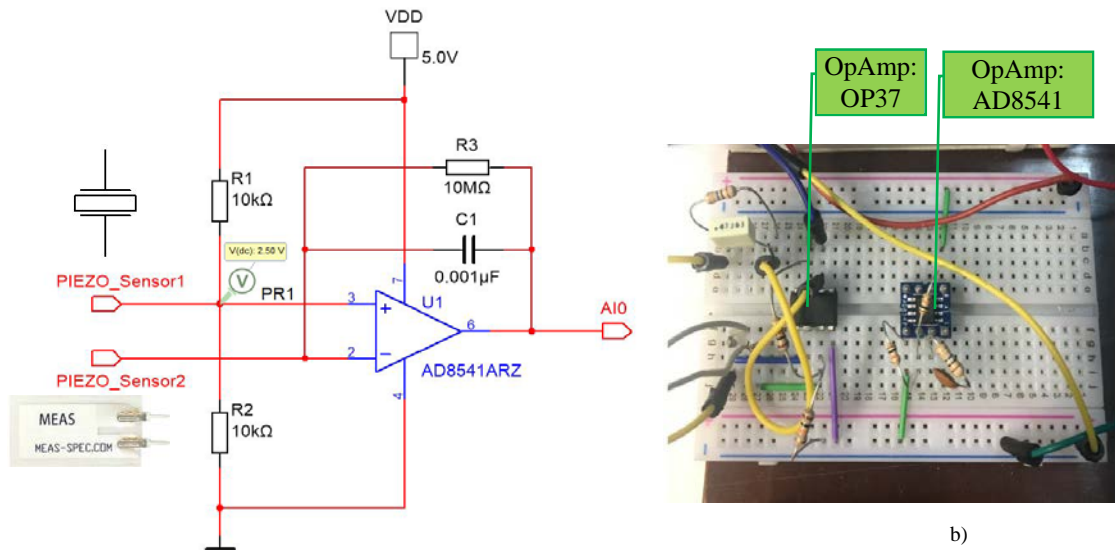


Fig. 5. Piezo transducer: a) schematic diagram and b) breadboard layout

The DT film element produces more than 10 millivolts per micro strain, about 60 dB higher than the voltage output of a foil strain gauge. The sensor can be readily adhered to SMA strip surface with double-sided tape or epoxy. Lead attachment can be achieved by low temperature solder. The piezo sensor can be seen as a capacitor with a piezoelectric crystal between two plates; it is an active sensor because any small deformation causes a variation of the charge which appears as a measurable voltage between the plates.

Piezoelectric sensor is followed by a charge-to-voltage converter that produces a voltage output proportional to the integrated value of the input current, or the charge injected. The converter uses an operational amplifier (U_1) which produces an output voltage inversely proportional to the value of the feedback reference capacitor (C_f) but proportional to the total input charge flowing during the specified time period. The gain of the circuit depends on the values of the feedback capacitor that plays the role of low pass filtering to the charge amplifier for noise mitigation.

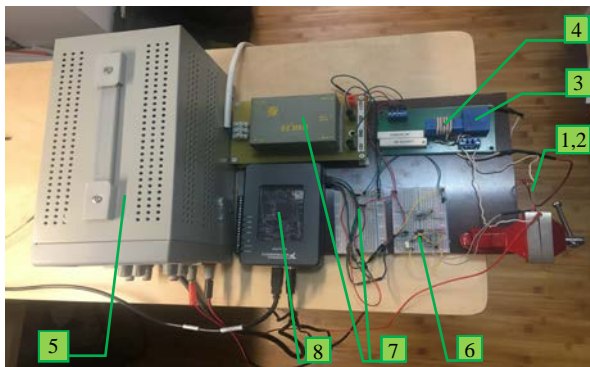
Decreasing the capacity C_f has the effect of obtaining a piezoelectric transducer more sensitive to small changes.

Resistors R_1 , R_2 form a divider that sets the voltage on the sensor to $V_{DD}/2$ (i.e., 2.5 V) and R_3 is a feedback resistor to provide DC gain path.

Two types of operational amplifiers were tested to converter design. High-quality operational amplifier with low noise, precision and high speed produced by Analog Devices – OP37 are used first [19].

Better sensitivity results were obtained with AD8541 operational amplifier. It is characterized by very low input bias current (4 pA), low levels of private noise, wide frequency band and rail to rail capability of input/output [20].

Fig. 6 pictures the experimental platform in a top view photo image a) and front view b). Items are noted accord-



a)



b)

Fig. 6. Photo image of the experimental platform: a) top view and b) front view.

ing to the Fig. 1 (Block diagram of the experimental platform).

The real-time measurements and display acquired waveforms are displayed on a PC screen and the data associated with these waveforms are stored for a later use.

III. SOFTWARE INTERFACE

The demanding of the current research application requires a hardware and software integration. The LabVIEW graphical programming environment is best suited for this integration.

LabVIEW 2018 - myRIO Toolkit [21] was used to communicate with the hardware platform for data acquisition, processing and display of results with designed virtual instrument (VI).

It is known that software minimizes development costs of any complex systems. Graphic programming is highly interactive because it is based on wires and icons, and the data flow is visible in block diagram; the design of the user interface or frontal panel is part of the programming.

Front Panel (FP) is the virtual instrument interface with the user, containing setting and control elements, or elements for displaying the values of different quantities to be studied (buttons, displays etc.).

The *Block Diagram (BD)* contains the graphical source code (known as G code) for how the VI runs. Every Frontal Panel object appear as terminals on the Block Diagram.

A. The Front Panels of virtual instrument

The front panel window is our graphical user interface (GUI) of a virtual instrument. The front panel has two controls, push-buttons (*Write* and *Stop*) and indicators (*Waveform Chart* and *Data Table*). The indicators simulate the instrument's output devices and display the data that the block diagram acquires and processes.

Fig. 7 shows front panel of virtual instrument. The user can see the values acquired by the hardware component of the measurement system (transducers and my RIO device) and processed using the virtual instrument. The visualization of the data is done with the help of four *Waveform Chart* type indicators.

For ease of future development, a tab control consisting of Page 1 (position 1 in the figure) is used.

The voltage generated by the piezoelectric transducer is illustrated in the diagram on the top left of the front panel (*Piezo Sensor Voltage*\V, in volts). The significance of the times on the X axis (*Time index*\s, in seconds) is the following: t_0 is the time at which the electric current is applied; t_1 is the time at which the deformation begins, t_2 is the time at which the deformation is maximum and t_3 is the time at which the electric current is interrupted.

Below this diagram, the user can observe the evolution of the activation electric current (*LEM SMA Strip Current*\A, in amperes; position 4 in Fig. 7).

It is also possible to observe the evolution of the voltage at the terminals of the SMA strip (*LEM SMA Strip Voltage*\V, in volts; position 3).

Knowing the current through and the voltage at strip terminals, our virtual instrument calculates the SMA strip resistance. The evolution of resistance over time is shown in *SMA Strip Resistance*\ Ohm diagram (position 5).

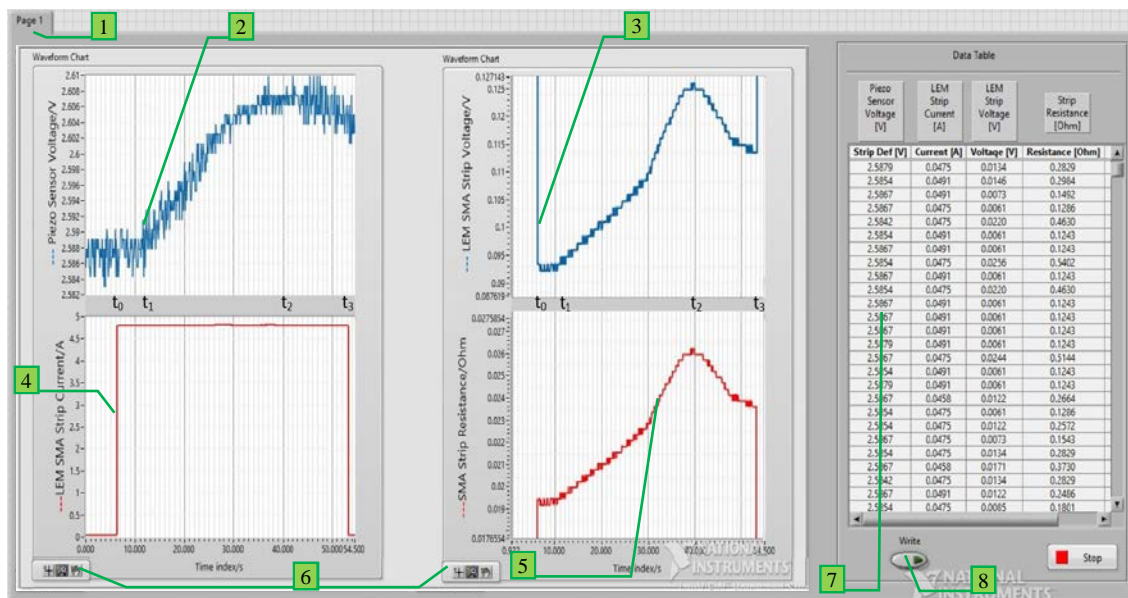


Fig. 7. Front Panel of virtual instrument (VI)

We can customize the appearance of a chart with the shortcut menu options. This allows a cursor to be displayed at a defined point coordinate. The *Graph Palette* (position 6) allows to move the cursor, zoom and pan the chart while VI runs.

The table with four visible columns (position 7 in Fig. 7) contains all the numerical values for the acquired and processed data. The number of rows might change with the vertical scroll bar. All data can be saved for further processing (*Write control*, position 8).

B. The Block Diagram of virtual instrument

Block Diagram is the source code of the virtual instrument. Presentation of the *Block Diagram* is useful for understanding the operation of the virtual instrument because LabVIEW uses data flow programming and the data flow determines the order of execution.

As shown in Fig. 8, this is a *Flat Sequence Structure* with three sub diagrams that execute sequentially: initialize; acquire and process data; close. The last sub diagram reset all the I/O channels of NI myRIO device.

All the objects include terminals of indicator and control, subVIs, functions, constants, structures and wires are included in a *Timed Structures* (type *Timed Loop*); it executes a sub diagram sequentially, each iteration (*i*) of the loop at the specified period.

Using the 1 MHz clock, timed structure can execute an iteration once every 1 microsecond. *Period (dt)* is 100 microseconds and specifies the amount of time that elapses between two subsequent iterations of the *Timed Loop*.

Analog Input Express VI are used for reads values from one or more analog input channels. These *Express VIs* allow the configuration of analog input ports and read a sample each time with the default FPGA personality.

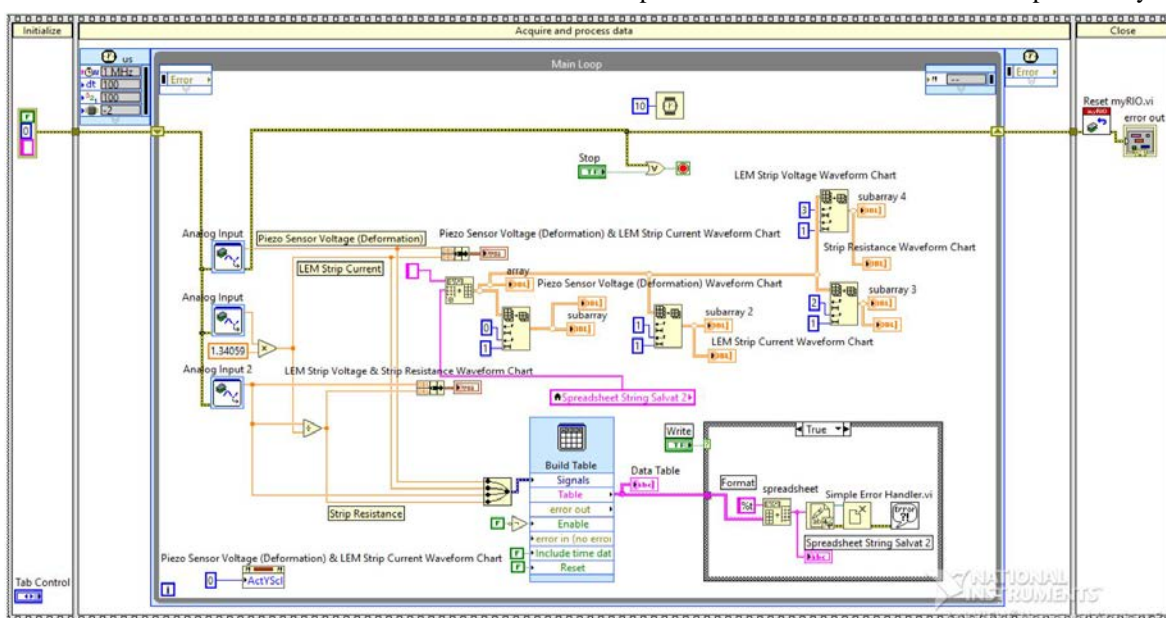


Fig. 8. Block Diagram of virtual instrument (VI)

IV. EXPERIMENTAL RESULTS AND PERSPECTIVES

Fig. 9 shows the tested cantilever SMA strip during the experiments; on the left - undeformed position ($\delta=0$, when the activation current is zero) and on the right – maximal deformation position δ_{max} .

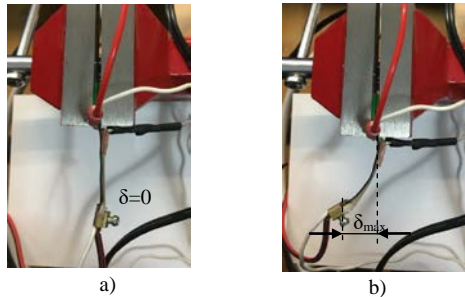


Fig. 9. Close-up image of the tested SMA cantilever: a) in the position without deformation; b) in the maximal deformation position

The following table show the experimental values for tested SMA strip, at different values of activation electrical current (3.6 A to 4.8 A).

TABLE I.
THE EXPERIMENTAL VALUES FOR STUDY OF SMA STRIP

Current [A]	t_0 [s]	t_1 [s]	t_2 [s]	t_3 [s]	V_1 [V]	V_2 [V]	R_1 [Ω]	R_2 [Ω]
4.8	6.16	8.35	40	53.11	2.58	2.6	0.0194	0.026
4.4	5.12	7.61	39.43	43.64	2.6	2.62	0.0246	0.0316
4.0	3.87	6.98	40.45	57.73	2.61	2.62	0.0255	0.0311
3.6	5.50	8.98	44.21	62.36	2.6	2.62	0.0289	0.0315

Data obtained and the connection with the phenomena that occur during the heating of the SMA band to the maximum deformation were analyzed in detail in [9]; the present paper focusing on the practical realization and use of the virtual measurement system.

The tested NiTi SMA strip can be used as an actuator to develop protection applications where very short activation times are required (i.e., vibration control, shape control, position control in automotive industries and fire protection).

In the future, using the advantages of virtual instrumentation (flexibility and minimizing set-up time costs) we will increase the analysis capability and the functionality of present system for testing and controlling of a cantilever SMA strip. Thus, sensors can be added to measure the temperature or elements to trigger an action when a certain threshold is reached.

V. CONCLUSIONS

The evolution of the electrical resistance and bending performance corresponding to the cantilever SMA strip was determined using virtual instrumentation.

The results of real-time measurements and acquired waveforms are displayed on a PC screen, and the data associated with these waveforms are stored on memory for later use.

Thus, the advantages offered by the virtual instrumentation were highlighted.

Source of research funding in this article: Research program of the Electrical Engineering Department financed by the University of Craiova.

Contribution of authors:

First author – 60%

Co-author – 40%

Received on July 14, 2020

Editorial Approval on November 03, 2020

REFERENCES

- [1] K. Otsuka, C.M. Wayman, *Introduction in shape memory materials*, Cambridge: Cambridge University Press, 1999.
- [2] C. LExcellent, *Shape-Memory Alloys Handbook*, Wiley-ISTE, 2013.
- [3] T.W. Duerig, K.N. Melton, D. Stockel, C.M. Wayman, *Engineering Aspects of Shape Memory Alloy*, Butterworth-Heinemann, 2013.
- [4] A. Rao, A. R. Srinivasa, J.N. Reddy, *Design of Shape Memory Alloy (SMA) Actuators*, Springer International Publishing, 2015.
- [5] T. Yoneyama, S. Miyazaki, *Shape Memory Alloys for Biomedical Applications*, Woodhead Publishing, 2008.
- [6] G. Deivasikamani, M. Thathan, P. Vellivel, *Virtual Instrumentation Based Heavy Machinery Vibration Analysis*, LAP LAMBERT Academic Publishing, 2019.
- [7] R. Prabhakaran, T.L. Galloway, "Strain measurement in a shape memory alloy with strain gauges," *Strain*, vol. 41, Issue: 4, pp. 177-184, November 2005.
- [8] H. Tobushi, K. Miyamoto, Y. Nishimura, K. Mitsui, "Novel shape memory actuators," *Journal of theoretical and applied mechanics*, vol. 49, Issue: 3, pp. 927-943, 2011.
- [9] S. Degeratu, G.E. Subțirelu, A. Rotaru, N.G. Bîzdoacă and P. Rotaru, "The electro-mechanical control of element NiTi shape memory alloy strip while bending, based on thermal analysis evidence," *Journal of Thermal Analysis and Calorimetry*, vol. 2, pp. 740-741, August 2020.
- [10] Y. Suzuki, Y. Kagawa, "Active vibration control of a flexible cantilever beam using shape memory alloy actuators," *Smart materials & structures*, vol. 19, Issue: 8, Article Number: 085014, August 2010.
- [11] S. Kaluvan, H.F. Zhang, "A novel DC current sensor using SMA controlled piezoelectric bimorph cantilever," *Proceedings of the ASME Conference on Smart Materials Adaptive Structures and Intelligent Systems*, September 2016.
- [12] U. Icardi, "Large bending actuator made with SMA contractile wires: theory, numerical simulation and experiments," *Composites part B-engineering*, vol. 32, Issue: 3, pp. 259-267, Special Issue: SI, 2001.
- [13] "Thermal Analysis with Differential Scanning Calorimetry product range". Available online: <https://www.perkinelmer.com/category/differential-scanning-calorimetry-dsc>.
- [14] "High-Performance DSC Instruments for Academic Research and Industrial Development". Available online: <https://www.mt.com/dsc/analysis>.
- [15] DYNALLOY, Inc. FLEXINOL® Actuator Ribbon technical and design data. Available online: https://www.dynalloy.com/tech_data_ribbon.php.
- [16] DYNALLOY, Inc. Introduction To FLEXINOL® Actuator Wire. Available online: <https://www.dynalloy.com/flexinol.php>.
- [17] LEM products: current transducers, voltage transducers. Available online: <https://www.lem.com/en>.

- [18] DT piezo film sensor strip. Available online: <https://www.te.com/usa-en/product-CAT-PFS0004.html>
- [19] Low noise, precision, high speed operational amplifier, OP37. Available online: <https://www.analog.com/media/en/technical-documentation/data-sheets/OP37.pdf>
- [20] Sensor interfaces and piezoelectric transducer amplifiers AD8541. Available online: https://www.analog.com/media/en/technical-documentation/data-sheets/AD8541_8542_8544.pdf
- [21] LabVIEW 2018 myRIO Toolkit Readme. Available online: <https://www.ni.com/pdf/manuals/375387d.html>
- [22] NI myRIO-1900: User Guide and Specifications. Available online: <http://www.ni.com/pdf/manuals/376047c.pdf>

Aspects Regarding the Impact of Electrical Vehicles' Charging on Power Quality

Denisa Rusinaru*, Gabriel Cosmin Buzatu*, Leonardo Geo Manescu* and Claudiu Popirlan*

* University of Craiova/Faculty of Electrical Engineering, Craiova, Romania, denisa.rusinaru@incesa.ro

Abstract - A major problem with the increased penetration of electric vehicles is the preparation of the power supply system to accommodate the increasing number of charging stations. Possible problems include exceeding the rated power of distribution equipment and electrical systems components, changing the voltage profile and altering the quality parameters of electricity. In these scenarios it is important for the grid operators to have an accurate information on present grid status, as well as the effects of EVs charging facilities interaction with the hosting grid. This knowledge will help the operators to more efficiently manage their grids while the e-mobility is expanding. This paper addresses issues related to the challenges of large-scale implementation of electric vehicles in Romania and especially their estimated impact on the power quality in current distribution networks. The authors present some of the results of a monitoring and analysis study of the power quality parameters in the coupling buses of some electric vehicle models during their charging cycle. The results of the study are included in a database used as a reference for a larger project aimed at developing intelligent solutions for PQ-based control of load units.

Cuvinte cheie: *calitatea energiei, monitorizare, rețea electrică de distribuție, vehicul electric, stație de încărcare.*

Keywords: *power quality, monitorization, power distribution grids, electrical vehicle, charging stations.*

I. INTRODUCTION

According to Directive 2010/31/EU last amendments, the EU Member States must establish the requirements for the installation of a minimum number of recharging points for electric vehicles for all non-residential buildings with more than twenty parking spaces up to 1. January 2025.

In Romania, the electric car transportation is currently in a pioneering phase, the lack of infrastructure of large capacity recharging stations being the main obstacle in its deploying. Nevertheless, the official figures show that e-mobility is in increasingly local demanding and the national policies are yet to appear. Still, there are some initiatives worth mentioning, as "Green Charging infrastructure program" launched in 2017 by the Ministry of Environment, Waters and Forests to support the acquisition of electrical vehicles (EVs) charging stations (CSs). In this respect, the authorities have created a scheme to finance 6000 EV charging stations by 2020. According to the Direction of Driving Licenses and Vehicles Registration (drpciv.ro) less than 2000 electric vehicles are currently on the roads in Romania. They can access about a 434 public charging points [1]. In order to accommodate the EVs charging loads in the actual

Romanian distribution system, it would be necessary for utilities to invest in and reinforce the grid infrastructures in heavily loaded areas. As the local power grid operator wanted to be prepared for the growing needs of EVs charging industry, it only made sense to choose a smart service that has the capability to be flexible and manage the growing load from EV charging and its impact on the grids. An intelligently integration of EVs can also partially solve the power quality (PQ) problems. For the expected increasing number of private or home charging stations (CSs), a comprehensive assessment of these loads' behaviors and impacts, as well as smart approaches that actively operate the grids can help to reduce the grid connection costs.

II. STATISTICS REGARDING THE EV'S IN ROMANIA

A. Hybrid electric vehicles

The three main types of electrical vehicles are generally known as hybrid electric vehicles (HEV), plug-in hybrids (PHEV) and battery electric vehicles (BEVs).

Although hybrids are not loaded from the distribution network, they are important as a reference for determining the degree of market penetration of BEVs and PHEVs.

There are several hybrid configurations. Modern hybrid electric vehicles use new technologies, such as regenerative braking, which, instead of dissipating the kinetic energy of the vehicle into the environment in the form of heat, as conventional braking systems do, recovers it in the form of electric energy, which is stored in batteries.

Some hybrid electric vehicles use their internal combustion engine to drive an electric generator, the current produced being stored in batteries or powering the electric propulsion motors directly.

Other hybrid electric vehicle technologies reduce emissions when idling by shutting down the internal combustion engine instead of letting it idle and restart it at start-up, a method known as the start-stop system. No mechanical gearbox is required in all configurations, as the speed and torque of an electric motor can be adjusted without problems by varying the frequency and actual current. The main advantage of the electric drive system is the bidirectional flow of energy. While the vehicle is in braking mode, the electric car operates in generator mode, and much of the vehicle's kinetic energy is converted into electrical energy stored in the battery.

Table I presents the technical specifications of the hybrid car models that dominated the market in Romania at the end of 2018.

B. Hybrids plug-in

Plug-in hybrid electric vehicles (PHEVs) have a propulsion system with a gasoline engine and an electric motor similar to HEVs, but with a larger battery that can be charged by both the own systems and power grid by plugging in. Lithium-Ion batteries are usually used for this purpose. Most PHEV devices are designed so that the owner can travel the longest distances in the city, using only battery power, the combustion engine being used only over long distances.

TABLE I.
TECHNICAL SPECIFICATIONS OF THE HEVs IN ROMANIA

Car model	Capacity of gas engine (l)	HP gas engine	HP electric engine	Fuel consumption (l/100 km)	Sold units
Toyota C-HR	1.8	98	72	3.8	355
Toyota Auris Hybrid	1.8	99	82	3.5	242
Toyota Yaris Hybrid	1.5	75	61	3.5	239
ToyotaRAV4 Hybrid	2,5	155	140	5.0	159
Toyota Prius	1,8	98	72	3.3	140

Table II presents the technical specifications of the dominant plug-in hybrids on the Romanian market in 2018. The Mercedes model falls into the exclusive category, less accessible. Nevertheless, it was introduced in this statistic as one of the models that has been available for testing in INCESA laboratory.

TABLE II.
TECHNICAL SPECIFICATIONS OF THE PHEVs IN ROMANIA

Car model	Capacity of gas engine (l)	HP gas engine	HP electric engine	Battery storage capacity (kWh)	Fuel consumption (l/100 km)
VW Golf GTE	1.4	150	102	8.7	1.7
Volvo v60 hybrid	2.4	215	68	11.2	1.8
BMW 225xe iPerformance	1.5	136	88	7.6	2.0
Mitsubishi Outlander	2.0	117	80	12.6	8.1 – 12.0
Porsche Cayenne E Hybrid	3.0	320	95	14.1	3.3 – 3.4
Mercedes-Benz GLE 500 e 4MATIC	3.0	333	116	8.8	3.7

C. Battery electrical vehicles

Battery electric vehicles (BEVs) do not have combustion engines, being driven only by energy stored in large capacity batteries (Lithium-Ion) that are charged from the electricity distribution system. The specifications of the best-selling electric cars in Romania are presented in Table III.

At the time of the study, the Solaris Urbino 18 electric model bus was put into circulation by the City Hall, for the performance tests prior to a future acquisition. It was also introduced in this statistic being another model that has been available for testing with INCESA laboratory's equipments.

D. User experience regarding electric vehicles

The EVs have certain advantages compared to classic fuel vehicles. They are designed to develop the power to cover the average daily distance up to 50 km. In addition to the fact that they do not need to access the services of a petrol station, EVs owners will never change their oil, thus meeting the criteria of a low-maintenance car.

TABLE III.
TECHNICAL SPECIFICATIONS OF THE BEVs IN ROMANIA

Volkswagen e-Golf	
Engine	100 kW (134 HP)
Battery capacity	35.8 kWh
Loading power	7.2 kW AC
Supply voltage	120V 240V
Autonomy	300 km (NEDC)
Speed	150 km/h
Loading time	5h15m
Average energy consumption	12.7 kWh/100 km
BMW i3	
Engine	127 kW (170 CP)
Battery capacity	33.2 kWh
Loading power	3.7 kW AC
Supply voltage	120V 240V
Autonomy	200km (NEDC*)
Speed	150km/h
Loading time	7h30m
Average energy consumption	13.1 kWh/100 km
Renault Zoe	
Engine	68 kW (92 HP)
Battery capacity	41 kWh
Loading power	22 kW AC
Supply voltage	120V 240V
Autonomy	403 km (NEDC*)
Speed	135 km/h
Loading time	2h15m
Average energy consumption	13.7 kWh/100km
Smart	
Engine	52 kW (71 HP)
Battery capacity	17.6 kWh
Loading power	4.6 kW AC
Supply voltage	120V 240V
Autonomy	155 km (NEDC*)
Speed	130km/h
Loading time	4h30m
Average energy consumption	11.5 kWh/100 km
Kia e-Niro	
Engine	64 kW (85 HP)
Battery capacity	67.1 kWh
Loading power	7.2 kW AC
Supply voltage	120V 240V
Autonomy	375 km (NEDC*)
Speed	167 km/h
Loading time	10h30m
Average energy consumption	17.1 kWh/100km
Solaris Urbino 18 electric	
Engine	160 kW (214 HP)
Battery capacity	125 kWh
Loading power	30 ...200 kW
Supply voltage	120V 240V
Autonomy	200 km
Loading time	< 6h

*New European Driving Cycle (NEDC)

However, the disadvantages of EVs are significant. While the technical features of the latest EVs allow owners to use them in the city, their use for travel outside the city is not advantageous due to the lack of a distributed and easily accessible charging infrastructure. Being forced to access certain charging points, the drivers

may be limited to a driving distance of half the total driving mileage of a fully loaded EV.

Many infrastructure changes have been proposed to allow EV owners to drive longer distances, but unfortunately all of these are accompanied by significant problems. In Romania, more than 400 charging stations are installed, of which 161 station (almost 37%) are fast charging points. Unfortunately, there are areas in Romania discovered. In addition, even for a high availability of fast charging stations, they remain less attractive compared to filling a gas tank because they need even 30 minutes to charge the battery to a capacity of 80%

Although the high cost of the batteries remains the main barrier when it comes to the price competitiveness of electric cars, it has decreased significantly in recent years. An analysis by Forbes shows that Lithium-Ion battery cell cost \$1,100/kWh in 2010, and by 2019 the cost dropped to \$156/kWh (with almost 86%) and things do not stop there. Considering that most EVs on the market have a battery capacity of 16... 28 kWh, the battery pack cost between \$3000 and \$7000, relatively easing the financial efforts to replace them.

Experts forecast that the price will reach \$100/kWh by 2023, level at which the electrical vehicles will reach a price parity with those with conventional engines [2].

In addition, new technologies are expected to appear, such as solid-state batteries, which will bring cheaper, faster-charging batteries to the market and have a longer service life, with a higher density.

Until then, however, the all-electric cars are used in Romania only as secondary cars. For people who can't afford a second car, a plug-in hybrid might be a better option. A potential new buyer who wants a "green" car without range restrictions can choose between a hybrid and a plug-in hybrid.

III. EVS CHARGING UNITS DEPLOYMENT AND GRIDS IMPACT

Since EVs require the use of batteries with high storage capacity, a large deployment of this concept is expecting to impact considerably the power grid design and operation [3]. Chargers are in general connected to the low-voltage (LV) grids, and their operation is characterized by electromagnetic perturbations affecting the PQ level. The uncoordinated charging can result in for instance in slow voltage deviations, rapid voltage variations (flicker), harmonics, phase voltage imbalance, grid losses and overloading, fluctuation of grid frequencies, which disturb end-users including more and more sensitive loads [4-8]. An intelligent integration of EVs and their CSs units can partially solve the existing and future power quality (PQ) problems. For the expected increasing number of private or home charging stations (CSs), smart approaches that make use of currently available excess capacities and actively operate the grids can help to reduce the grid connection costs.

A wide spectrum of charging management algorithms is proposed in literature. While PQ issues are solved by designing a new charging connector or charging station with PQ compensation [9, 10], some algorithms have been proposed to move EV charging load to off-peak hours or to react in real-time on changes of the different local or global parameters of the grid [11]. Other EV

charging policies [12] consider voltage support for the distribution network to increased penetrations of distributed PV systems. There are also solutions proposing local smart charging algorithms based on *droop* controller [12, 13] to reduce line voltage drops and voltage unbalances. These solutions estimate the voltage locally, but ignore the overall state of the LV grid. Decentralized approaches considering wider grid areas are developed based on traffic light estimation model of the voltage variation parameter and assets loading [14].

A better understanding of these PQ issues specific to EVs will aid power operators in the design of their distribution systems and provide guidance for asset planning. Consequently, more online monitoring and active interventions during grid operation are necessary to maintain critical boundary conditions such as bus voltages and asset loading within permissible limits. As the local power grid operator wanted to be prepared, it only made sense to choose a smart service that has the capability to be flexible and manage the growing load from EV charging and its impact on the network.

IV. RESEARCH PROJECT FOR ASSESMENT OF EV'S IMPACT REGARDING POWER QUALITY

By regarding the present national politics and the state of hosting power grids, any action and project which aims to integrate and develop an optimal management of the publicly accessible EVs charging infrastructure in the region should take into account the following challenges: (1) Existing local distribution grids are made of long-life assets and equipment which cannot be removed or easily upgraded; (2) The development strategy of the local power distribution grid operator (DGO) envisages improving the level of safety and quality in the distribution of electricity and reducing energy losses; (3) When it comes to e-mobility infrastructure at least three players emerge: the electricity supplier, the charge point operator (CPO - responsible for the installation, service and maintenance of the CSs), and even an e-mobility provider (EMP - enables access to the complex charging infrastructure), which should see "CS operation" as a business model, but as an additional service for customers considering a minimal negative impact on the local hosting grid; (4) The technical, economical, societal and regulatory context for distribution grids and their customer significantly varies has particular specificity in Romania in comparison with other European countries with more advanced e-mobility initiatives; (5) The operational policy of the local DGO and the specific nature of the networks that it operates require the identification of potential risk hotspots associated in the immediate perspective with the expansion of large commercial areas and the acquisition of the EVs fleet of local public transport.

One of the projects (METROPOLITANER) developed within Smart Grids Laboratory of INCESA (Research Hub for Applied Sciences of University of Craiova) aims to develop and validate in a laboratory environment a smart control system architecture for different EVs charging typologies connected to the local power distribution grid in order to reduce the impact on the asset loading and quality of voltage.

For reaching the overall purpose, the project is planning to achieve the following objectives: (1) To

assess the present PQ perturbation background and the individual emissions of the EVs charging units in the power distribution grids by data measurements; (2) To assess the impact of EVs on PQ and assets operation of power distribution grids by measurements and numerical simulation; (3) To perform studies to evaluate the e-cars impact on the distribution network; (4) To identify the needs/requests of different stakeholders regarding concerning an optimal management of the EVs charging infrastructure; (5) To evaluate the efficiency of the adopted charging control system architecture; (6) To develop and test the laboratory-scale prototype for a smart PQ-based control system architecture.

The objectives are feasible and can be done in the framework of this project by taking into consideration that:

- The local municipality has a viable perspective for becoming one the biggest “green city” of Romania by implementation of *Green City Action Plan*. The local authorities launched the procurement procedure for 46 electrical buses, 46 normal charging stations and 11 fast charging stations. This city accommodates the largest commercial complex in the area, with a parking spaces for around 2700 cars, with the prospect of installing 27 CSs.

- The local power distribution grid operator (DGO) is a supporter of the e-mobility initiatives and mainly stakeholder regarding the effects of EVs integration into the actual power grids.

- There is a traditional project-based collaboration between university and the local power distribution company and urban transport authority in the area of energy efficiency and process control and optimisation.

The first phase of the METROPOLITANER project aims the PQ data acquisition and analysis of the EVs charging stations impact on power distribution grids. Some results of these monitorisation sessions are presented in this paper, outlining mainly the features of the acquisition procedures: type and parametrisation of measuring equipments, EV's types, charging type, monitorisation period and time, charger location.

V. PQ MEASUREMENTS AND DATA ANALYSIS

This study includes the results of PQ monitoring for the charging process of two types of EVs: Mercedes-Benz GLE 500 e 4MATIC (HPEV) and Solaris Urbino 18 (BEV). A specific attention was paid to the PQ parameters: voltage deviations, harmonics and flicker. There were also noted the loading variation. The objective is to define and test a measurement and analysis procedure to be extended at whole grid level and develop a database useful for further understanding and forecasting of the CSs behavior regarding PQ issues.

In order to analyze the impacts that the two EVs types have on the local distribution system, the data sets were collected directly at the LV buses of the supplying transformer substations, as well as on the individual charging circuits of EVs batteries.

In order to monitor the electrical parameters that describe the charging process of the batteries of the two vehicles considered, a power quality analyzer FLUKE 435 was used. FLUKE 435 is a PQ meter class A, in accordance with EN 50160. The measurements were performed during whole charging period, with a RMS

sampling of 5000 samples on 10/12 cycles according to IEC61000-4-30 (50 Hz). The recordings include voltage and current waveforms, as well as recording of MIN, MAX and AVG readings of PQ parameters user-configurable at 1 min. The data was stored by the equipment in a .odn file type database that can be opened with the proprietary Fluke Power Analyze software and exported as .xls file type. The characteristics of the monitorization sessions are given in Table IV.

TABLE IV.
CHARACTERISTICS OF THE MONITORIZATION SESSIONS

Characteristics	Values	
	Mercedes-Benz GLE 500 e 4MATIC	Solaris Urbino 18
Charging time duration	4h 15 min (10:00 – 14:15)	2h (15:45-17:45)
Battery charging power (kW)	1.25	83
Battery charging current (A)	5.9	108
Supplying voltage (V)	230 a.c. (1 ph)	400 a.c. (3 ph)
Supplying voltage variations (V)	236.9...241.0	410.5...420.3
Range of voltage harmonic content (VTHD %)	1.73...2.30	5.13...57.36
Range of long-term flicker (Plt)	0...0.562	0...0.448

The results of the monitorization sessions are given in Fig. 1-12 (according to Table V).

TABLE V.
LIST OF RESULTS OF THE MONITORIZATION SESSIONS

Recording	Correspondent figures	
	Mercedes-Benz GLE 500 e 4MATIC	Solaris Urbino 18
Active & reactive power time variation	Fig. 1	Fig.7
RMS voltage time variation	Fig. 2	Fig. 8
RMS current time variation	Fig. 3	Fig. 9
Statistics of voltage variation	Fig. 4	Fig. 10
Statistics of THD variation	Fig. 5	Fig. 11
Statistics of flicker variation	Fig. 6	Fig. 12

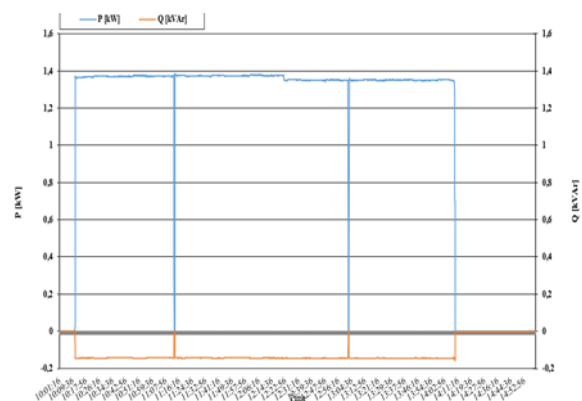


Fig. 1. Power time variation on Mercedes battery charging circuit: active power (blue), reactive power (red).

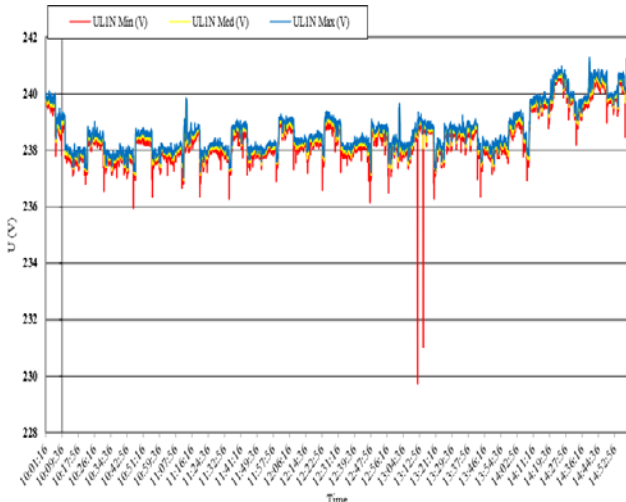


Fig. 2. RMS Voltage time variation on Mercedes battery charging circuit (MIN, MAX, AVG evolution).

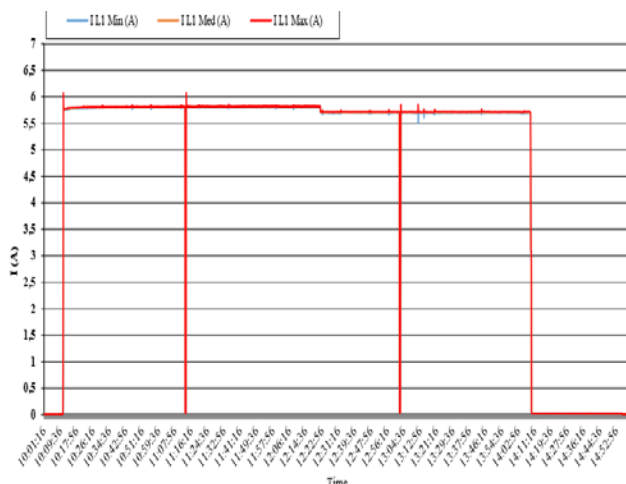


Fig. 3. RMS Current time variation on Mercedes battery charging circuit (MIN, MAX, AVG evolution).

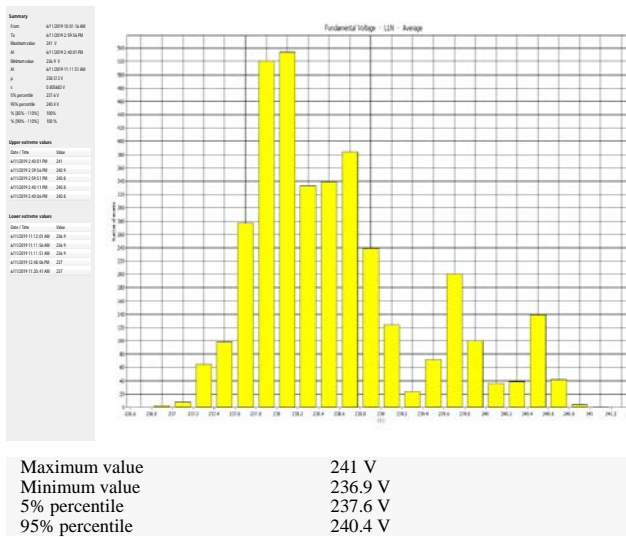


Fig. 4. Statistics of voltage time variation (fundamental voltage L1 average) on Mercedes battery charging circuit.

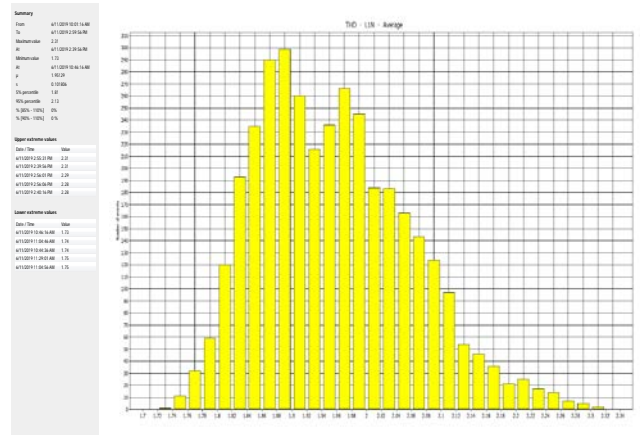


Fig. 5. Statistics of voltage THD (THD L1N average) time variation on Mercedes battery charging circuit.

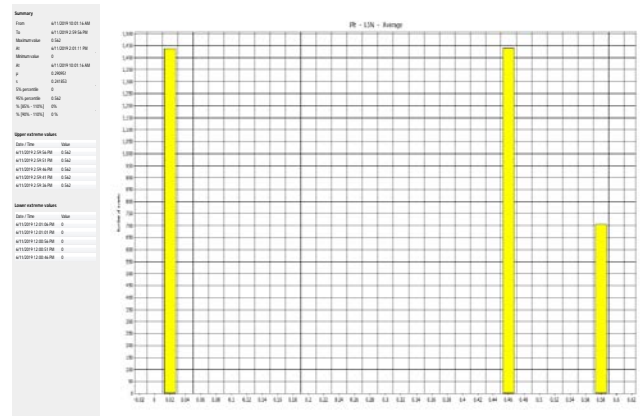


Fig. 6. Statistics of long-term flicker (Plt L1N average) time variation on Mercedes battery charging circuit.

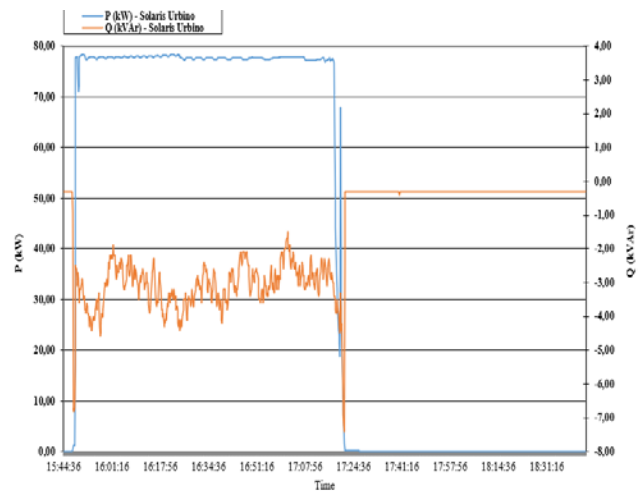


Fig. 7. Power time variation on Solaris battery charging circuit: active power (blue), reactive power (red).

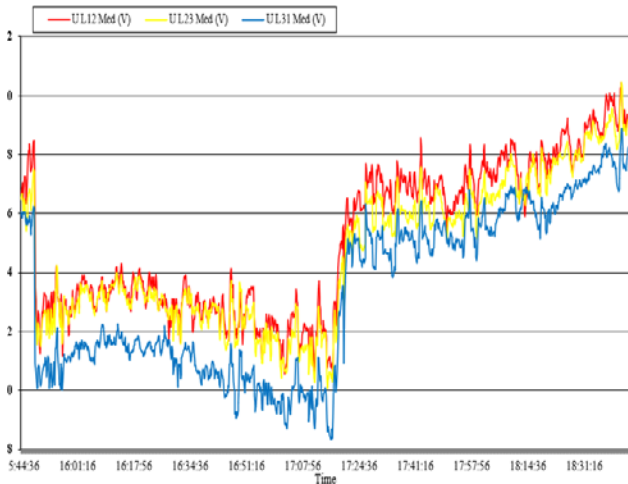


Fig. 8. RMS Voltage time variation on Solaris battery charging circuit (MIN, MAX, AVG evolution).

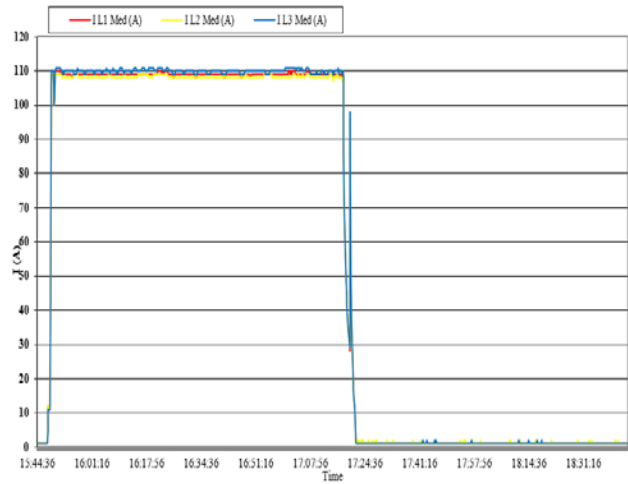
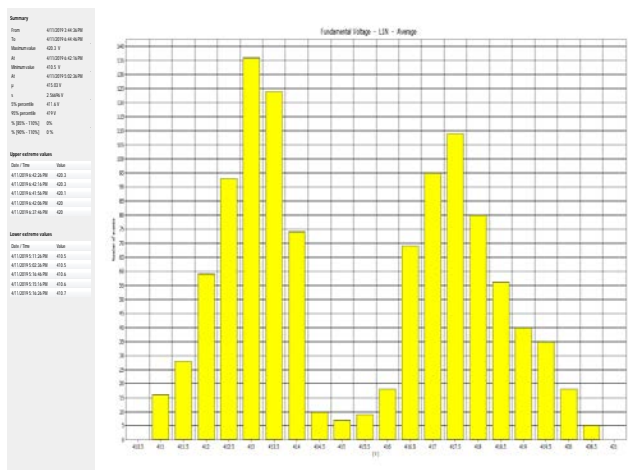
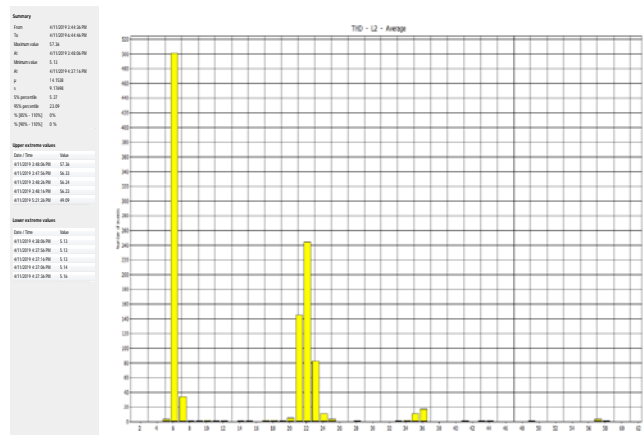


Fig. 9. RMS Current time variation on Solaris battery charging circuit (MIN, MAX, AVG evolution).



Maximum value 420.3 V
 Minimum value 410.5 V
 5% percentile 411.6 V
 95% percentile 419 V

Fig. 10. Statistics of voltage (fundamental voltage L12) time variation on Solaris battery charging circuit.



Maximum value 57.36 %
 Minimum value 5.13 %
 5% percentile 5.37 %
 95% percentile 23.09 %

Fig. 11. Statistics of voltage THD (THD L2 average) time variation on Solaris battery charging circuit.

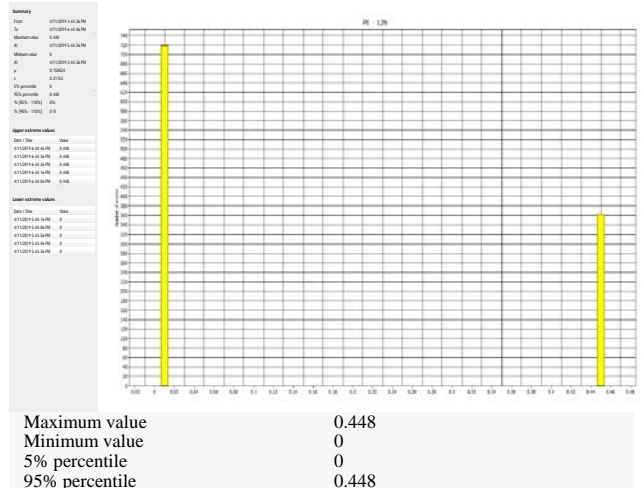


Fig. 12. Statistics of long-term flicker (Plt L2) time variation on Solaris battery charging circuit.

The further observations allow to extend the characterization of PQ parameters' evolution during the entire charging cycle as a set of singleton values.

Mercedes-Benz GLE 500 e 4MATIC

- Variation of voltages on the supply bars in the permissible range ($U_{nom} \pm 10\%$): 236.9... 241 V (Fig. 4);
- Harmonic distortion on the feed bars in the permissible range (THD < 8%): 1.73... 2.31 (Fig.5);
- Plt flicker index on feed bars is in the allowable range ($Plt < 1$): 0...0.562 (Fig.5);
- There are registered 2 periods of approx. 1 min in which the active power decreases to close to 0, with corresponding increases in the reactive power value; the charging cycle shows no other oscillations.
- The variation of the power on the charging cycles of the EV battery, powered on phase B causes variations of reactive power on phase C.

Solaris Urbino 18

- Variation of voltages on the supply bars in the permissible range ($U_{nom} \pm 10\%$): 410.5... 420.3 V, with cumulative probability 95% of 10 min samples CP95% of 419 V;

- Harmonic distortion on the supply bars very high, exceeding the allowed limit (THD < 8%): 5.37...57.36%, with CP95% of 23.09%;

- Plt flicker index on feed bars in the allowable range (Plt < 1): 0...0.448, with CP95% of 0.448;

- Symmetrical system of voltages and currents (zero asymmetry factor);

- The power absorbed from the grid during charging process does not show major variations, except for the end of the period, characterized by multiple oscillations that precede the ending of the charging process.

VI. CONCLUSIONS

The widespread use of electric cars, both cars and trucks and buses, is likely to significantly reduce the pollutant emissions prevented by transport.

The ambitious plan of European countries to drastically reduce emissions from transport by using millions of electric cars could be blocked by the lack of supply capacity of new charging stations in large cities.

In order to achieve government goals of becoming carbon neutral by 2045, EU countries should have several million plug-in hybrids and electric vehicles by the end of the next decade. While many of these will be powered at home for shorter journeys, a network of stations for longer journeys is needed, as are cabs and commercial trucks. The predicted "explosion" of electric cars could lead to a major problem: excessive growth in electricity demand, with proportional impact on the performances, losses and power quality of supplying grid. In order to accommodate the EV charging loads in the actual Romanian distribution system, it would be necessary for utilities to reinforce the grid infrastructures in heavily loaded areas. In order for electric vehicles to be manageable despite the lack of supply capacity or PQ emissions there should be developed extensive assessments of EVs impact on the power grids preceding their intelligent integration.

These solutions can partially solve the existing grid operational and infrastructure problems, and even future power quality (PQ) problems.

In this paper there were presented certain aspects related to the impact on the power quality of the EV charging stations in the supplying distribution grids, as part of an extended research project. The study presented in the paper is based on information obtained through direct measurements for two types of electrical vehicles during their normal charging process.

ACKNOWLEDGMENT

„This work was supported by the grant POCU380/6/13/123990, co-financed by the European Social Fund within the Sectorial Operational Program Human Capital 2014 – 2020.”

Contribution of authors:

First author – 50%

First co-author – 20%

Second co-author – 20%

The third co-author – 10%

Received on July 10, 2020

Editorial Approval on November 23, 2020

REFERENCES

- [1] *** European Alternative Fuels Observatory - Charging infra stats, "Normal and fast public charging points (2020). Romania". Available at: <https://www.eafo.eu/alternative-fuels/electricity/charging-infra-stats#>.
- [2] A. J. Hawkins, "Tesla's Elon Musk said a \$25,000 electric car with next-gen battery in the works". In The Verge, Sep 22, 2020. Available at <https://www.theverge.com/2020/9/22/21450916/tesla-battery-pack-elon-musk-price-kilowatt-hour-ev-cost-tables>
- [3] J.A.P. Lopes, F.J. Soares, P.M.R. Almeida, "Integration of electric vehicles in the electric power system," in Proceedings IEEE 99(1), 2011, pp. 168–183.
- [4] G.A. Putrus, P. Suwanapingkarl, D. Johnston et al, "Impact of electric vehicles on power distribution networks," in Proceedings of the IEEE vehicle power and propulsion conference (VPPC'09), Dearborn, 2009, pp 827–83.
- [5] J. Taylor, A. Maitra, M. Alexander, "Evaluations of plug-in electric vehicle distribution system impacts," in Proceedings of the IEEE power and energy society general meeting, Minneapolis, 25–29 Sept 2009, pp. 1-6.
- [6] J. Chynoweth, C.-Y. Chung, C. Qiu, P. Chu, R. Gadh, "Smart Electric Vehicle Charging Infrastructure Overview," in 2014 IEEE PES Innovative Smart Grid Technologies (ISGT) Conference Washington, DC, USA, 2014. Available at: <https://smartgrid.ucla.edu/pubs/Smart%20Electric%20Vehicle%20Charging%20Infrastructure%20Overview.pdf>
- [7] M. Takagi, K. Yamaji, H. Yamamoto, "Power system stabilization by charging power management of PHEV with LFC signal," in Proceedings of IEEE Vehicle Power and Propulsion Conf (VPPC'09), Dearborn, 2009, pp 822–826.
- [8] L. Kutt, E. Saarijarvi, et al, "A review of the harmonic and unbalance effects in electrical distribution networks due to EV charging," in Proceedings of 12th Internat. Conf. on Environment and electrical eng. (EEEIC'13), Wroclaw, 2013, pp 556–561.
- [9] A. Cortes, S. Martinez, "A hierarchical algorithm for optimal plug-in electric vehicle charging with usage constraints," Automatica 68:119–131. Available at <https://doi.org/10.1016/j.automatica.2016.01.060>, 2018.
- [10] Z. Fan Z, "A distributed demand response algorithm and its application to PHEV charging in smart grids," in IEEE Transactions Smart Grid 3(3), 2018, 1280–1290.
- [11] L.G. Manescu, D. Rusinaru, et.al, "Complex Software System for Data Management and Analysis of Power Distribution Grids," 2017 4th Internat.Conf. on Mathematics and Computers in Sciences and in Industry (MCSI), Corfu, Greece, 2017, pp. 51-56.
- [12] F. Kong, X. Liu, Z. Sun, Q. Wang, "Smart Rate Control and Demand Balancing for Electric Vehicle Charging," in Proceedings of 2016 ACM/IEEE 7th Internat. Conf. on Cyber-Physical Systems (ICCCPS). IEEE, Vienna, 2016, pp 1–10.
- [13] M. Faschang, F. Kupzog, R. Mosshammer, A. Einfalt, "Rapid control prototyping platform for networked smart grid systems.," In Proceedings of IECON 2013 - 39th Annual Conf of IEEE Industrial Electronics Society. IEEE, Vienna, 2013, pp 8172–8176.
- [14] Martinenas, K. Knezovi'c, M. Marinelli, "Management of power quality issues in low voltage networks using electric vehicles: Experimental validation, " in IEEE Transactions Power Delivery 32(2),2017,pp.971–979.

'Open Ended' Laboratory to Study the Influence of Unit's Weight on Axle Torque in Railway Traction

Petropol Șerb Gabriela Dana*, Petropol Șerb Ion†

* University of Craiova/ Faculty of Electrical Engineering, Craiova, Romania, gpetropol@em.ucv.ro

† SC RELOC SA, Craiova, Romania, ionpetropol@yahoo.com

Abstract – The aim of the paper is to propose a scenario and a test bench to study, in a trans-disciplinary way, how the operation of a traction unit with asynchronous motor is influenced by the railway channel. The main issue of the experiment is to find how the weight of the motor unit can influence the axle torque. The topics involved are: 1. 'How to calculate the train resistance to forward movement' (expected results: calculation and plot in Matlab) and 2. 'How to calculate the force needed to move the train and the traction characteristic at the startup of the train' (expected results: data acquisition and plotting in LabView). The design of the scenario follows the guideline of an 'Open Ended' laboratory. The advantages of this approach are: the study can have an inter- and trans- disciplinary approach, the lab could be developed in a hybrid way: in presence in lab, individual for theoretical research and in team to solve and disseminate the results. Regarding IT communication, the research needs to use different software packages as Matlab, LabView.

Cuvinte cheie: laborator cu caracter deschis, rezistența la înaintare a trenului, caracteristica de tracțiune la demarare a unității motoare cu motoare asincrone.

Keywords: open ended laboratory, the forward resistance to train movement, traction characteristic at start of the motor unit with asynchronous motors.

I. INTRODUCTION

According to the literature [5], [7], [8], [10] the analysis of some functional aspects specific to the "asynchronous traction motor – railway traction chain" system shows that, during the start-up period, it is observed that:

- the speed changes in the interval $[0, v_a]$, where v_a is the speed corresponding to the calculation regime and represents the speed up to which the adhesion can be used.
- the frequency changes in the interval $[f_p, f_a]$, where f_a is the frequency corresponding to the speed of the calculation regime, v_a , and f_p the frequency at which the train is detached (starting frequency).
- the vehicle must operate on families of traction characteristics which depend on the total mass of the train, m_t , grip and track slope, i .
- starting can be studied for the following types of characteristics (fig. 1), [13]: starting at the adhesion limit (curve 1), starting at constant traction force (curve 2) and starting at constant acceleration (curve 3).

In order to capture as many functional aspects of the asynchronous motor as possible operating under conditions specific to electric traction, an 'open ended laboratory' type

experiment [11], [12] is proposed which will be carried out in several stages, each responding to a well-established objective. Data obtained by data acquisition will be synthesized and processed during the period (2 weeks) of the experiment. As input data for the determination and graphical representation of the electromagnetic torque (a main parameter of the study) it is necessary to determine the parameters of the working machine and to make a specific calculation diagram in Lab View.

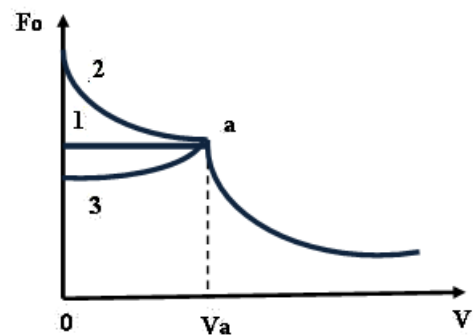


Fig. 1. Possible shapes of the traction characteristic at start-up: starting at the grip limit (curve 1), starting at constant traction force (curve 2) and starting at constant acceleration (curve 3)

II. RESEARCH APPROACH

A. Starting the railway traction vehicle. Mechanical simulation of the maximum traction effort

In order to capture, in conditions as close as possible to reality, the phenomenon of detachment of the drive unit at start-up, it is proposed to mechanically achieve a torque resistant to the asynchronous motor shaft to simulate the initial frictions 'wheel-track', respectively to highlighting the constant term 'a' in the formula for resistance to advance.

1) *Finding the forward resistance to train movement:* for a moving train, the determination of the forward resistance has been the subject of numerous measurements which have led to the most general empirical formulas (1).

$$R_p = a + bv + cv^2 \quad (1)$$

In a first approximation, the constant term a, sometimes called pure slip, depends only on the axle load. It expresses the sliding of the wheel on the rail and bearing. The coefficient b only takes into account the quality of the track and the stability of the convoy. The coefficient c, which naturally represents the aerodynamic part, differs only if the train travels in the

open air or in the tunnel, increasing significantly when passing from one sequence to another, this passage being a function of the piston effect. It is particularly influenced by the aerodynamic quality of the convoy: the front shape, the interval between vehicles, the side roughness, the roughness above and below the body. Except for the fixed form convoy (TGV; Rae; TEEII), where it was possible to measure accurately, this formula remains very approximate.

Table 1 presents some useful formulas for calculating the main forward resistance R_p [N / t] where v [m / s] is the travel speed, S_F [m²] - area of the front surface of the vehicle, m [t] - mass vehicle, and in figures 2,3 their representation in Matlab.

The general formulas, applied to variable shape trains, highlight its mass. This can be exemplified in the case of a locomotive with n axles.

$$R_p = (0.65 \cdot 10^{-3} + 13 \frac{n}{m} + 0.036 \cdot 10^{-3} v + 0.39 \frac{v^2}{m}) \cdot mg \quad (2)$$

TABLE 1:

 CALCULATION FORMULAS FOR THE MAIN FORWARD RESISTANCES R_p .

No	Type of rolling stock	R_p [N/t]
Formulas used by C.F.R., v [m/s]		
1.	Locomotive C'0C'0	$12.3+0.353v+0.0318v^2$
2.	Locomotive B'0B'0	$12.3+0.353v+0.0477v^2$
3.	Passenger wagons	$19.6+0.0397v^2$
4.	Specialized freight wagons	$15.7+0.0471v^2$
5.	Different freight wagons, loaded	$19.6+0.0652v^2$
Formulas used by S.N.C.F., v [km/h]		
6.	Locomotive CFF de 120t: Ae 6/6	$35 + 0,06v + 0,59(v/10)^2$
7.	Locomotive de80t: BB 9001	$13+0,1v+0,375(v/10)^2$
8.	Locomotive de 120t: CC 6001	$12,5 + 0,1v + 0,25(v/10)^2$
9.	Locomotive CFF de 93 t: Am 4/6	$35 + 0,4(v/10 + 1,2)^2$
10.	TGV	$2540+33,44v+0,572v^2$
11.	Freight wagons, specialized material	$15+v^2/400$
12.	Different freight wagons	$15+v^2/160$
Formulas used by metro builders in Moscow, Sao Paolo / Bucharest		
13.	Subways	$28,5+0,424v+0,089v^2$
14.	Subways	$24,5+9,234v^2/m$

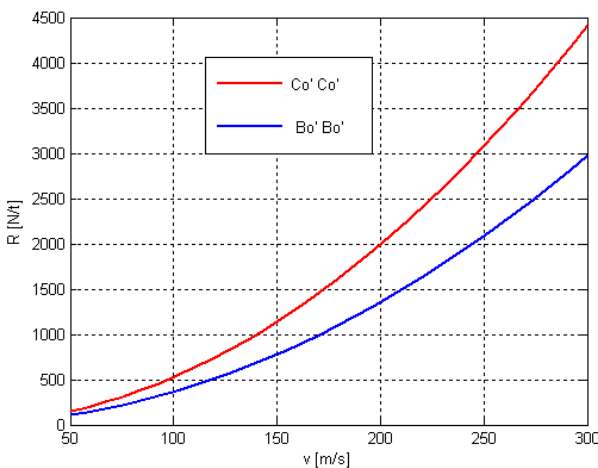


Fig.2. Resistances versus speed for Romanian locomotives (plots in Matlab)

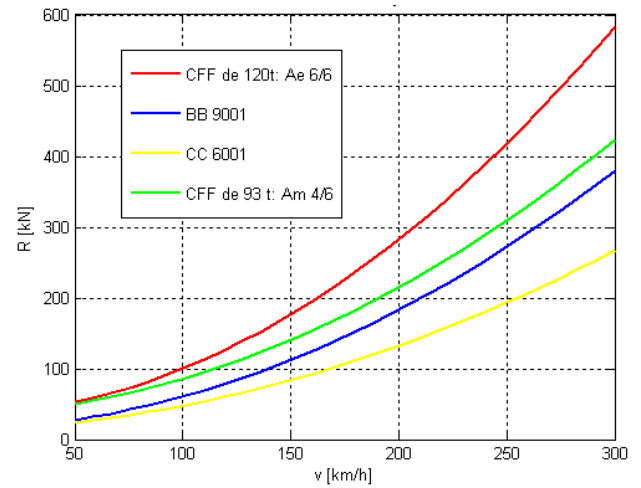


Fig.3. Resistances versus speed for SNCF locomotives (plots in Matlab)

For towed trains, without traction motors included, we can cite the CFF formula for freight trains (3) or the general Strahl formula (4) (table 2) [3], [4].

$$R_p = (1.5 + 0.011v + 7 \cdot 10^{-3} v^2) 10^{-3} mg, [N] \quad (3)$$

$$R_p = (2.5 + k_t (v + v_v)^2 \cdot 10^{-3}) 10^{-3} mg, [N] \quad (4)$$

where v_v is the average wind speed (10-15km / h) and k_t coefficient that takes into account the type of train (table 2).

TABLE 2:

COEFFICIENTS THAT TAKE INTO ACCOUNT THE TYPE OF TRAIN ACCORDING TO STRAHL'S FORMULA.

Coefficient k_t		The type of train
[h ² /km ²]	[s ² /m ²]	
0.25	3.2	a. express, direct, heavy freight train
0.33	4.2	b. classic passenger train
0.4	5.1	c. specialized freight train
0.5	6.5	d. compose freight train
1	13	e. empty freight train

Graphs and formulas are usually given for the current running regime. At start-up, after a longer parking of the vehicle (over 20 minutes) the main forward resistance is higher in the first moments (until the wheels make 1.5-2 rotations) than the one resulting from these graphs or formulas for $v = 0$. It is zero for all other speeds. The starting force is present only at very low speeds; therefore it can be calculated with relation 4.

$$F_a = 7.5 \cdot 10^{-3} \cdot m \cdot g \quad (4)$$

In the literature, [7], [8], [13], the starting torque is determined, depending on the characteristics of the vehicle, by the relation (5):

$$M_{mmax} = \frac{F_{mmax} \cdot D_{med}}{2 \cdot i_a}, [kNm] \quad (5)$$

where F_{mmax} is the maximum traction force developed by the engine, D_{med} is the average wheel diameter, [m], i_a the gear ratio of the gear.

On another scale, given the direct proportionality between the traction force and the electromechanical torque, we can say that it is confirmed that the traction force required at starting (6) is proportional to the mass of the drive unit.

$$F_p = G_t \cdot \left(r_p \pm i + \frac{1}{\varphi} \cdot \frac{dv}{dt} \right), \quad (6)$$

where: G_t , is the total weight of the train in kN; $(1/\varphi) \cdot (dv/dt)$ is the specific inertia force that can be set for an acceleration of 0.2 - 0.6 m/s²; φ represents the acceleration imprinted on the train by a force of 1N / kN.

2) Conception of the experimental situation

In the experiment, the technical solution to achieve this enounced dependence is to place a grooved pulley (FR - figure 4) at the free end of the asynchronous machine shaft. The pulley channel will allow the suspension through a steel cable of a variable weight (figure 4) which represents, on another scale, the weight of the motor unit considered.

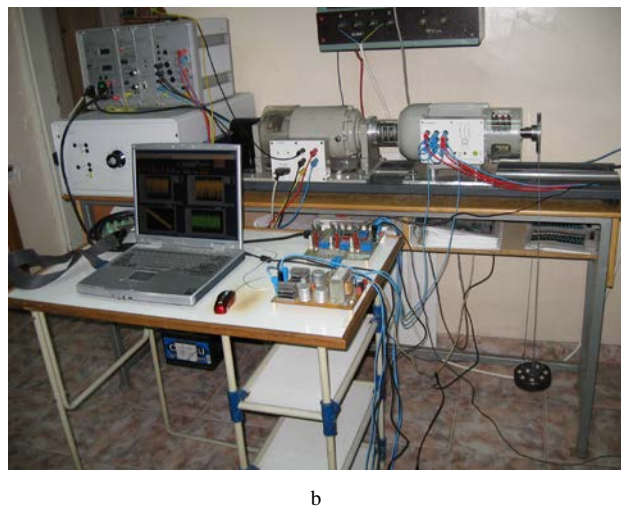
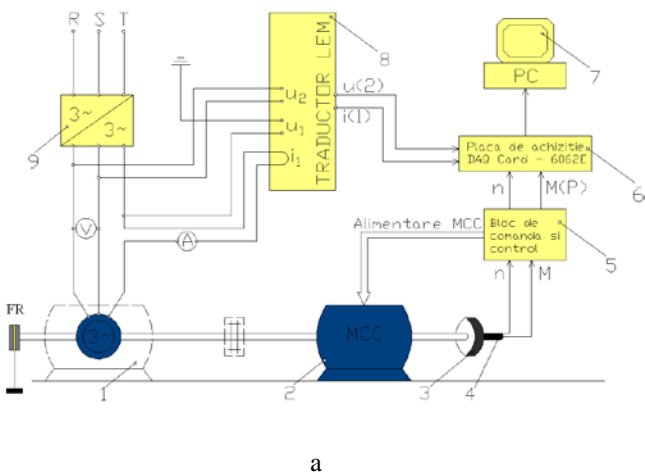


Fig.4. Experimental test bench with the application of the mechanical brake: a. schematic diagram; b. general view

In this way, the process of detaching the drive unit at start-up will be simulated as close as possible to real conditions. To

vary the starting load, toroidal steel weights with a mass of: 0.5, 1, 2 and 3 kg were made, with the help of which the desired load parameter can be set. Several experimental situations were imagined.

3). Realization of the experimental situation: Asynchronous motor operation powered by a frequency inverter with rated voltage $U_n = 400V$ and frequency $f_n = 50Hz$, for different braking weights, $m = ct$.

In order to determine the influence of the weight of the 'drive unit' on the shaft torque in the case of asynchronous motor powered with rated voltage $U_n = 400V$ and frequency $f_n = 50Hz$, the aim is to trace the families of natural mechanical characteristics $M(n)$ for different weights placed on the shaft on pulley.

The practical realization of this experiment involves:

- torque control of the brake machine to ensure a variable torque variable $M_r = 0 - 7 Nm$,
- put one by one, on pulley the different weights ($m = 0.5; 1; 2; 3 kg$);
- supply of the asynchronous motor with nominal voltage, at the nominal frequency.

4). Processing of experimental data

The quantities of interest (speed and mechanical torque at the shaft, supply voltage and current) are purchased using the acquisition board. To visualize the variation of the shaft torque according to the shaft speed, the diagram in figure 5 will be used.

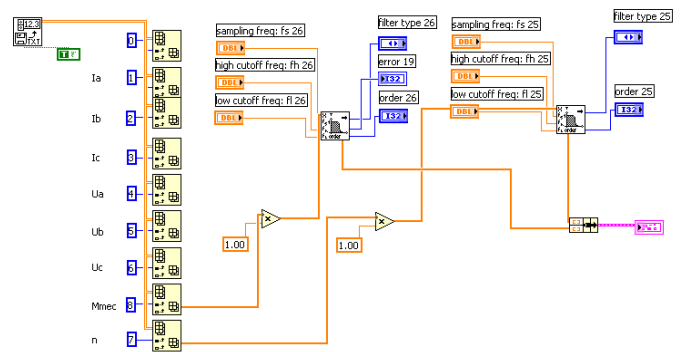


Fig.5. Diagram for visualizing the torque variation at the shaft as a function of speed

III. SIMULATIONS AND RESULTS

The proposed experiment is the starting point to elaborate a learning scenario for an 'open ended' laboratory around the topic: How the weight of the motor unit can influence the axle torque? The aim of this scenario is to connect the students around this subject, to immerse the students in a learning experience that allow them to discuss the problem and to gain high order thinking skills from following the solution. This scenario could be a modern method to use e – techniques in electrical engineering learning. As in [11], a flow chart could be proposed to debate the scenario of the problem.

The experiment was repeated for different weights placed at the free end of the cable and by further processing in Lab View the families of characteristics in figure 6 were obtained.

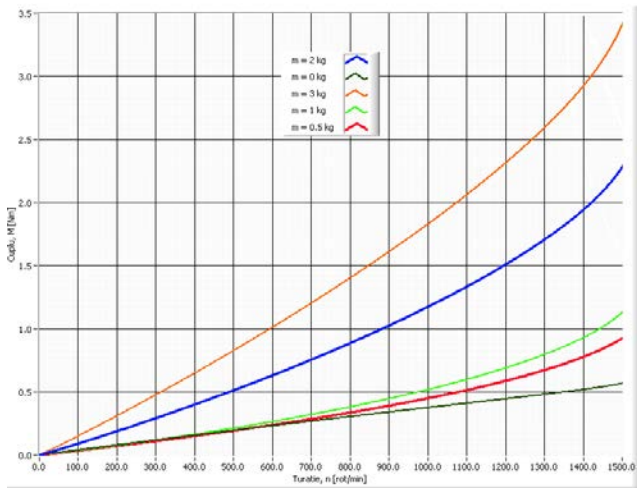


Fig.6. Family of characteristics $M(n)$ for $m = ct$, $M_r = 0 - 7 \text{ Nm}$, $U = 400 \text{ V}$, $f = 50\text{Hz}$.

From the study of the family of characteristics it is observed, as expected, that at the same speed (for example $n = 1400 \text{ rpm}$), the torque required at the shaft is higher for a higher braking mass ($m = 0\text{kg}$, $M = 0.51 \text{ Nm}$; $m = 0.5\text{kg}$, $M = 0.82 \text{ Nm}$; $m = 1\text{kg}$, $M = 0.99 \text{ Nm}$; $m = 2\text{kg}$, $M = 1.93 \text{ Nm}$; $m = 3\text{kg}$, $M = 2.94 \text{ Nm}$;). Therefore, the higher the mass of the vehicle, the higher the torque at the required shaft and therefore the starting torque.

Following the evolution of the speed in the two cases ($m = 0 \text{ kg}$, $m = 3\text{kg}$) it is observed that this is also influenced by the presence of the weight at the end of the pulley.

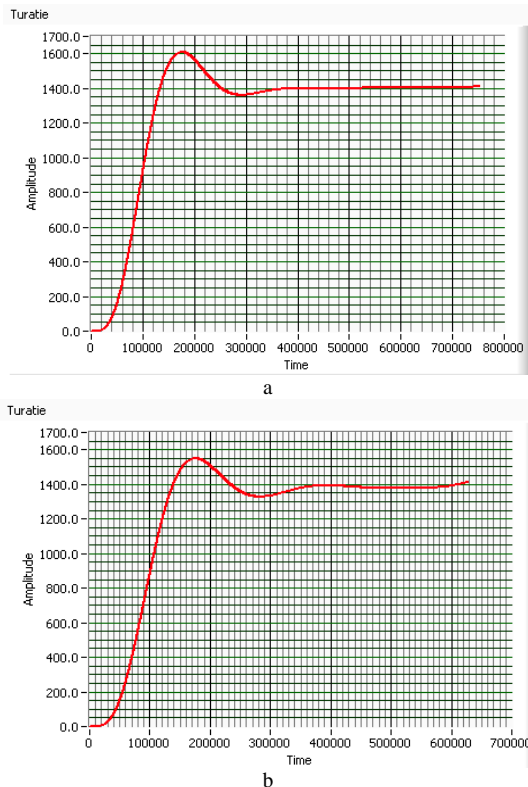


Fig.7. Variation of asynchronous motor speed over time, $n(t)$, in cases where the braking mass is: a. $M = 0\text{kg}$, b. $M = 3\text{kg}$

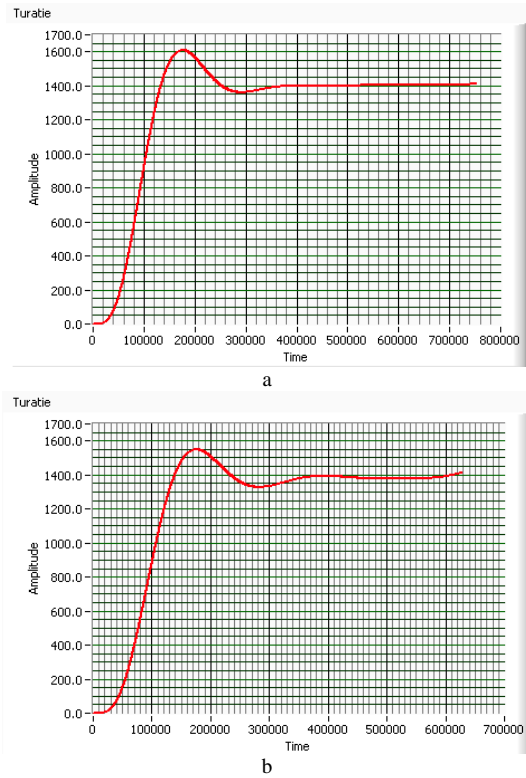


Fig.8. Time variation of the mechanical torque at the asynchronous motor shaft, in cases where the braking mass is: a. $m = 0\text{kg}$; b. $m = 3\text{kg}$.

Figures 7 and 8 show the time variation of the speed and the mechanical torque at the shaft, under the conditions of operation on the natural mechanical characteristic without a braking mass, $m = 0\text{kg}$ (fig. 7a, fig. 8a), respectively on the natural mechanical characteristic (fig. 7b, fig. 8b) if the braking mass is $m = 3 \text{ kg}$.

There are different time intervals to reach the stationary value of the torque (lower in case of a higher braking weight), as well as the oscillations of the speed and torque in the first moments of starting, after which both the speed and the torque reach the values stationary.

In order to observe the variation of the torque at the shaft in case of variable frequency starting ($f = 0 - 50 \text{ Hz}$), as well as the effect of the braking weight on this variation, we aim to trace the families of characteristics $M(n)$ for different weights placed at the end of the brake cable. mechanical.

The practical realization of this experiment involves:

- constant torque control of the brake machine;
- suspending in turn, at the end of the pulley cable, the different weights;
- starting the asynchronous motor with variable frequency, on frequency characteristics ($f = 0 - 50 \text{ Hz}$).

In order to observe the influence of the starting frequency on the value of the shaft torque, repeated starts of the asynchronous motor with different starting frequencies for the same weight of the motor unit will be performed. The tracing of the families of characteristics $M(n)$ will be followed.

The practical realization of this experiment involves:

- torque control of the brake machine to ensure a variable torque variable $M_r = 0 - 7 \text{ Nm}$,
- suspension in turn, on pulley, of different weights;

- starting the asynchronous motor with variable starting frequencies (increasing from 10 to 10 Hz);
 - The purchase of the quantities of interest (speed and mechanical torque at the shaft, voltage and supply current) is made with the help of the acquisition board.
- Subsequent processing in Lab View yields the feature families in figure 9 for a starting frequency $f_p = 50\text{Hz}$.

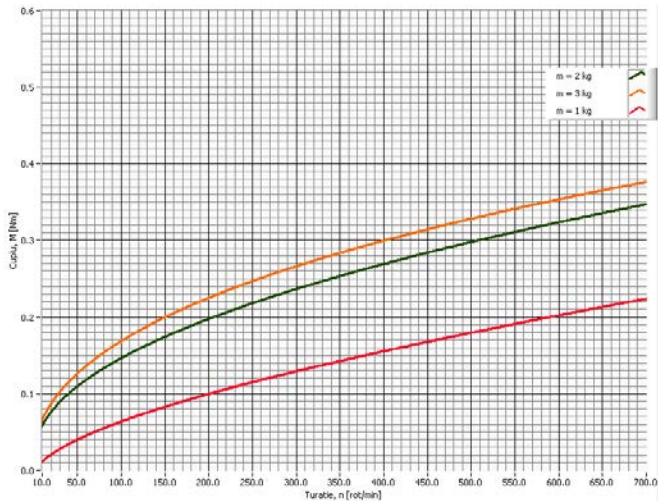


Fig.9. Family of starting characteristics $M(n)$ for starting frequency $f = 50\text{Hz}$ and braking masses $m = 1; 2$ and 3 kg .

Figure 9 shows that, for the same starting frequency, the initial value of the torque is higher for a higher braking mass.

Figures 10 and 11 show the same variations for the frequencies of 30 Hz and 20 Hz, respectively.

Comparing figures 9, 10 and 11, which represent the family of starting characteristics with constant frequency and different braking masses, it is observed once again that, for the same starting frequency, the initial torque value is higher for a higher braking mass is big.

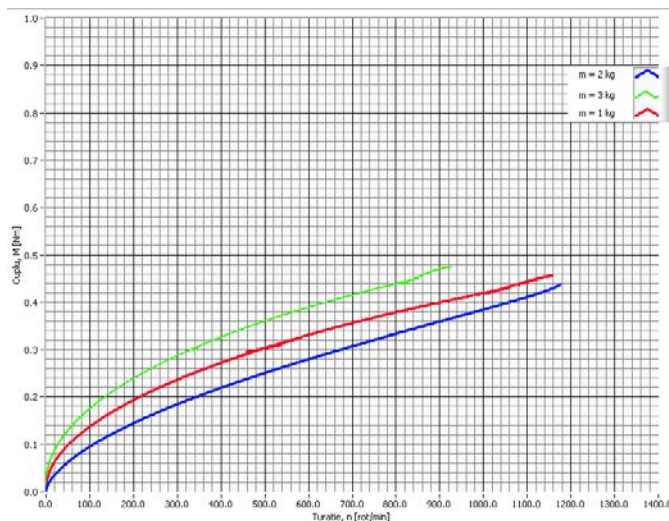


Fig.10. Family of starting characteristics $M(n)$ for starting frequency $f = 30\text{Hz}$ and braking masses $m = 1; 2$ and 3 kg .

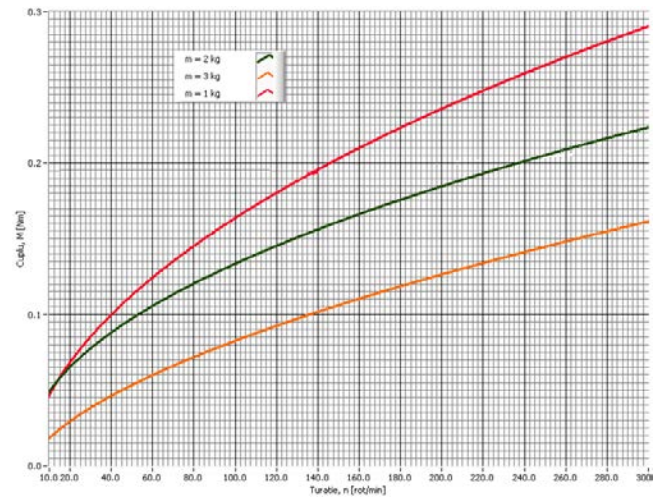


Fig.11. Family of starting characteristics $M(n)$ for starting frequency $f = 20\text{Hz}$ and braking masses $m = 1; 2$ and 3 kg .

During the experiments, in addition to the mechanical quantities, the torque and speed of the machine shaft and the values of stator currents and voltages were acquired. With the help of these data direct observations can be made on the behavior of the asynchronous traction motor. The variation in time of these quantities, in the situations presented in the experiment, can be visualized with the help of a block diagram made by LabView, similar to the one in figure 5.

IV. CONCLUSIONS

The paper proposes a learning tool to study different practical situation which are involving a traction motor unit with asynchronous motor.

Proposing and realizing experimental situations, the paper show how the acquired data could be implement using numerical method to calculate different characteristics of an asynchronous motor. These results could be easier applied in different practical situation or learning scenarios.

An important advantage of this proposal is that the study could be made in a hybrid mode both in presence as in online (an important feature of our days).

It also responds to an actual context of industrial environment and educational background characterized by translating into computer mode all data, aimed to increase the efficiency and the quality of process.

This paper is a response to the need of organized the knowledge in an authentic and resourceful form to be effortless applies to improve the understanding of operating the electro-mechanical systems.

Source of research funding in this article: Research program of the Electrical Engineering Department financed by the University of Craiova.

Contribution of authors:

First author – 60%

First coauthor – 40%

Received on July 02, 2020

Editorial Approval on November 15, 2020

REFERENCES

- [1] Duffy, M.C., "Three-phase motor in railway traction", IEE PROCEEDINGS-A, Vol. 139, No. 6, pp. 329-337, ISSN 0960-7641, November 1992.
- [2] Gandanegara, G., *De la modélisation à la simplification de modèles par bond graph. Application à une chaîne de traction ferroviaire*, Rapport de DEA INP Toulouse, 2000.
- [3] Kaller, R., Allenbach, J.A., *Traction électrique, Volume 1, Collection Électricité*, Presses Polytechniques et Universitaires Romandes, Lausanne, 1995.
- [4] Kaller, R., Allenbach, J.A., *Traction électrique, Volume 2, Collection Électricité*, Presses Polytechniques et Universitaires Romandes, Lausanne, 1995.
- [5] Kreuawan, S., Gillon, F., Moussouni, F., Brisset, S., Brochet, P., *Optimal design of traction motor in railway propulsion system*, In proceeding of International Aegean Conference on Electric Machines, Power Electronics and Electromotion Joint Conference, pp. 343-348, September 2007.
- [6] Lochot, C., *Modélisation et caractérisation des phénomènes couplés dans une chaîne de traction ferroviaire asynchrone*, Thèse INP Toulouse, 1999.
- [7] Mihăilescu, D., *Locomotive și trenuri electrice cu motoare de tracțiune asincrone*, Ed. Didactică și Pedagogică, București, 1997.
- [8] Mihăilescu, D., *Sustența și propulsia magnetică în transportul feroviar*, Ed. Academiei Romane, București, 2008.
- [9] Nicola, A., D. Cismaru, D., C., *Tracțiune Electrică - Fenomene Modele Soluții, Volumul I*, Ed. Sitech, Craiova, 2006.
- [10] Patin, P., *La traction électrique et diesel-électrique*, ÉDITIONNS LÉON EYROLLES, Paris, 1954.
- [11] Petropol-Serb, G.D., Petropol-Serb, I., "Open ended laboratory" method applied in the conception of a test bench to simulate a diesel electric transmission – Annals of the University of Craiova - Electrical Engineering Series, No. 35, 2011; ISSN 1842-4805, pg 184 -191.
- [12] Petropol-Șerb, G.D., Petropol-Șerb, I., Câmpeanu, A., Petrisor, A., Degeratu, S., *Virtual Laboratory in the Engineering Education*, New aspects of engineering education, Proceedings of the 5th WSEAS / IASME International Conference on Engineering Education (EE'08), pp. 99-104, ISBN: 978-960-6766-86-2, ISSN:1790-2769.
- [13] Popa, G., „Tracțiunea feroviară cu motoare asincrone trifazate”, Ed. Matrix Rom, București, 2005.
- [14] *** - *LabVIEW™ .- User Manual*, National Instruments, Austin, 2003.
- [15] Lozano, J. A. ; Félez, J.; de Dios Sanz, J.; Mera, J.M - *Railway Traction*, Universidad Politécnica de Madrid Spain, Reliability and Safety in Railway, www.intechopen.com
- [16] Radosavljevic, A. - *Measurement of train traction characteristics*. Proceedings of the Institution of Mechanical Engineers, Part F: Journal of Rail and Rapid Transit, 220(3):283–291
- [17] M.M. Albu, K.E. Holbert, G.T. Heydt, S.D. Grigorescu, V. Trusca, "Embedding remote experimentation in power engineering education," IEEE Transactions on Power Systems, Vol. 19, No. 1, Feb. 2004, pp. 139-143.
- [18] Uyulan, C.; Gokasan, M.; Bogosyan, S. - Re-adhesion control strategy based on the optimal slip velocity seeking method, Journal of Modern Transportation, 26, pages36–48(2018)
- [19] Konowrocki, R. - *Modelling of dynamic aspects of operation in railway vehicle traction drive system including the electromechanical coupling*. Scientific Journal of Silesian University of Technology. Series Transport. 2019, 105, 101-111. ISSN: 0209-3324. DOI.

Constructive Dimensions Optimization for Asynchronous Motors used in Coal Mills

Raluca-Cristina Presură (Nicolae), Sorin Enache*, Ion Vlad*, Marian-Ștefan Nicolae*

*University of Craiova/ Faculty of Electrical Engineering, Romania, raluca.presura92@gmail.com

Abstract - The high operating cost, owed to the large consumption of active and reactive power, led to the optimization of the design and construction of asynchronous motors used in driving the coal mills. The reduction of the operating cost is a difficult problem, because the motor usually lies in a closed enclosure, with provided gauge dimensions, and with specific requirements imposed by the type of drive in use. Using this information, while keeping the existing electromagnetic stresses (for heating reasons), the optimal construction dimensions can be established by design, so as to reduce the operating cost. The optimization is substantiated by the decrease of the operating cost of such a motor with 26100 euros, as compared to the existing version.

Cuvinte cheie: motoare asincrone pentru mori de carbune, proiectare optimala, simulare.

Keywords: asynchronous motors for coal mills, design optimization, simulations.

I. INTRODUCTION

The preparation of the coal dust is performed with the aid of six combined mills, with hammers and fans, each mill being driven by a high-power asynchronous motor of 500 kW.

The coal grinding mill from Fig.1 performs the crush, grind and transformation of the coal into dust, which is then sprayed into the furnace boiler. The better the quality of the grinding, the higher the efficiency and productivity of the power plant, the costs of electricity production being also reduced.

The coal mill has a high moment of inertia, resulting in a substantial increase of the start-up time. To avoid the overheating of the rotor cage, the current limitation was required over this interval, and an accessible starting torque needed to obtain accelerations mechanically supported by the whole system.

The asynchronous motor is coupled to the rotor of the mill by a regulable hydraulic coupling, to which the oil is introduced in half-couplings, centrifuged toward the outside, thus becoming a toroidal ring that performs the drive.

The concern for the optimization of electric motors has gained a lot of attention lately, considering the huge manufacturing and operating expenses borne by the manufacturer and the beneficiary.

Currently, the optimal design methods of electric motors are reanalyzed and continuously enriched with new elements, in order to increase the accuracy of the experimental measurements (eg use of appropriate software, high-performance computers, introduction of

saturation and skin effect in classic models of electric motors). For this reason, the amount of calculations increased a lot, and efforts are being made to reduce the working time [1-6].

The resemblance with an optimal motor can be achieved only by means of a large number of independent variables, which determine a very large number of possible combinations, of around $10^{20} - 10^{24}$. Therefore it is not recommended to try all of the possible combinations.



Fig. 1. Fan coal mill.

In general, the mathematical models that take into account the magnetic saturation and its dynamic variation, as well as the effect of the repression current, accurately provide valuable results in a range of admissible and practical errors.

These models [7-9], are mandatory in the design stage, as well as in anticipating the behavior of a manufactured motor, subjected to a given stationary or dynamic process.

II. THE MATHEMATICAL MODEL USED IN THE OPTIMAL DESIGN OF ASYNCHRONOUS MOTORS

A. These mathematical models

The models [5] be expressed as:

$$\begin{aligned} h_i(x_1, x_2, \dots, x_n) &= 0, \quad i = 1, 2, \dots, l \\ g_j(x_1, x_2, \dots, x_n) &\leq 0 \quad j = 1, 2, \dots, m \end{aligned} \quad (1)$$

where $i = 1, 2, 3, \dots, n$ are the optimization variables.

The restrictions imposed for the motor driving the coal mill are checked after their calculation, and in case the

mathematical model is not solved, new values are used for the optimization variables.

The literature shows that the electromagnetic stresses are important factors in the design process of asynchronous motors, with major impact over the optimization criteria.

B. The objective function, variables and constraints

In order to establish the optimum constructive dimensions of asynchronous motors used in driving the coal mills, we use of minimum operating cost criterion, $f(\bar{x})=C_e=\min$.

It correctly reflects the operating expenses (which are high), necessary during the amortization of the investment:

$$C_e = C_{ea} + C_{er} = N_o T_{ri} c_{el,a} \Sigma p + N_o T_{ri} c_{el,r} \Sigma q \quad (2)$$

N_o - the number of operation hours, during a year, of the motor, $c_{el,a}$ - the cost of one kWh of active power, $c_{el,r}$ - the cost of a kVARh of reactive power, T_{ri} - investment payback time; Σp , Σq - the total motor losses / reactive power consumption at rated load operation.

The investment made to buy this type of motor is expressed by the manufacturing cost:

$$C_f = k_f C_{ma} \quad (3)$$

The cost of the active materials C_{ma} , is simply determined by knowing m_{Fe1} , m_{Fe2} - the consumption of silicon sheet for the stator and rotor magnetic circuit, respectively; m_{Cu1} , m_{Cu2} - the quantities of copper conductor for windings, and the prices of these materials.

The factor k_f - determined for asynchronous similar motors, takes into account the efficiency of the technological process in the power plant.

The variables of the objective function are established depending on their weight over the established optimization criterion.

This optimization uses eight variables, these being the main constructive dimensions: D , δ - diameter and air gap of the machine, $\beta_{c1}=b_{c1}/t_1$, b_{01} , h_{01} , - dimensions related to the stator slot and $\beta_{c2}=h_{c2}/b_{c2}$, b_{02} , h_{02} - dimensions related to the rotor slot.

The lower and superior limits are established to limit the search domain, thus reducing the working time.

$$\begin{aligned} x_{\min_i} &\leq x_i \leq x_{\max_i} \\ x_i &= \{D, \delta, \beta_{c1}, b_{01}, h_{01}, \beta_{c2}, b_{02}, h_{02}\} \end{aligned} \quad (4)$$

There are also restrictions imposed by the specific of the coal mills drive system:

$$m_p \geq m_{p,i}; \quad i_p \leq i_{p,i}; \quad m_m \geq m_{m,i} \quad (5)$$

m_p , m_m , i_p - starting and maximum torque; starting current.

C. Computing the minimum of the objective function

The direct search methods [10-14], of the optimum for multi-variable problems, with restrictions, are the most appropriate, because they do not use the derivatives of the objective function and are based on the idea of advancing to the optimal through improvements made along the way.

Determination of the optimum using Rosenbrock method with constraints

It is proposed the minimization the objective function depending on the following variables:

$$C_e = f(D, \delta, \beta_{c1}, b_{01}, h_{01}, \beta_{c2}, b_{02}, h_{02}) \quad (6)$$

The Rosenbrock optimization methods involve a search after each variable, until convergence is reached or an area limited by the vicinity of the constraints is reached. The limit areas are determined as follows:

-the lower area

$$x_{\min_i} \leq x_i \leq x_{\min_i} + (x_{\max_i} - x_{\min_i}) \cdot 10^{-4} \quad (7)$$

- the superior area

$$x_{\max_i} - (x_{\max_i} - x_{\min_i}) \cdot 10^{-4} \leq x_i \leq x_{\max_i} \quad (8)$$

The search begins with an arbitrary point $\bar{x}^{(0)}=(D^{(0)}, \delta^{(0)}, \beta_{c1}^{(0)}, b_{c1}^{(0)}, h_{c1}^{(0)}, \beta_{c2}^{(0)}, b_{c2}^{(0)}, h_{c2}^{(0)})$ placed in the admissible domain of restrictions, without being part of the limit areas. The main stages are:

- the function $f(\bar{x}^{(0)})=C^{(0)}=C^*$ is evaluated

- from the chosen point, the initial search directions parallel to the coordinate system are established and the next steps are determined;

- for each point where the constraints are met, the function $f(\bar{x})$ is evaluated;

- the obtained value is compared with the previous one, the lowest value is kept and it is denoted by C^* .

- Rosenbrock sequential movements are carried out for each direction and the value of the function $f(\bar{x})$ is evaluated.

If the value at the current point is weaker than C^* , or the restrictions are violated, the search procedure is continued without restrictions, by using new movement reference frames, obtained with the Gramm - Schmidt procedure.

The search continues until the chosen convergence criterion is met.

III. SIMULATIONS AND RESULTS

The results of the construction optimization of the asynchronous motor used to drive a coal mill can be noted in the presented analysis. The considered parameters are $P_N=500$ kW - rated power; $U_N=6$ kV - rated voltage; $I_{IN}=62.6$ A - rated current; $n_1=500$ rpm - synchronism speed.

The operation of the mill requires the following starting and operating characteristics: $M_p \geq 1.05 \cdot M_N$ - starting torque; $I_p \leq 5.5 \cdot I_N$ - starting current; $M_m \geq 2.1 \cdot M_N$ - maximum torque.

The manufacturing, operation costs and the costs with the active / reactive power were calculated starting from known data: $N_{ore}=330 \cdot 24=7920$ hours / year - the number of operation hours per year; $T_{ri}=6$ years - time to recover the investment; $c_{Cu}=12$ €/kg - the cost of one kilogram of copper; $c_{Fe}=0.95$ €/kg - the cost of one kilogram of iron (silicon sheet); $c_{el,a}=0.131$ €/kWh - the cost of one kWh of

active power, $c_{el,r} = 0.013$ €/kVARh - the cost of one kVARh of reactive power.

The following costs resulted for the analyzed motor: $C_{f,m} = 68590$ €; $C_{em} = 403400$ €; $C_{e,a} = 217000$ €, $C_{e,r} = 186400$ €.

These results will be further considered as reference (reported) quantities.

In order to easily track the weight of each optimization variable, the plots are provided in per unit values. The costs are reported with equations of type (9):

$$c_e = \frac{C_{e, var, m}}{C_{e, m}} \quad c_{ea} = \frac{C_{ea, var, m}}{C_{ea, m}}, \quad c_{er} = \frac{C_{er, var, m}}{C_{er, m}}, \quad (9)$$

$C_{e, var, m}$, $C_{ea, var, m}$, $C_{er, var, m}$ - costs with the operation / active energy / reactive energy for the analyzed motor version;

$C_{e, m}$, $C_{ea, m}$, $C_{er, m}$ - the same costs, but for the motor version considered as reference.

A. The optimization with respect to the variables D, δ (motor and air gap diameter)

The research conducted with respect to these variables (constructive dimensions) led to much better results: a decrease of c_t by approximately 4.54%, Fig.2.a.

There is a great limitation of the search field due to the restrictive conditions imposed. The areas of $c_{e,a}$, c_{er} - the total active / reactive power costs, as components of the operating cost, can be noticed in Fig.2.b and Fig.2.c.

The results of the optimization with respect to the analyzed pair of variables (D, δ) can be observed in table no.1, where the most important characteristics are presented.

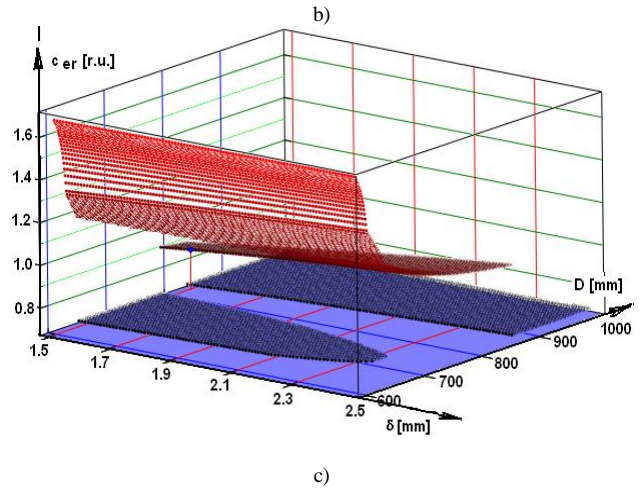
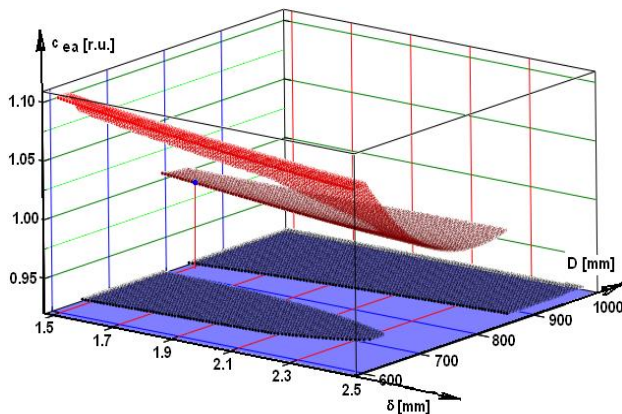
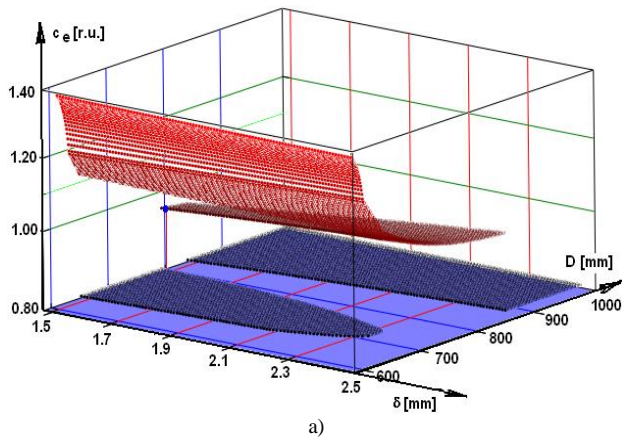


Fig. 2. The response areas for the pair of variables D, δ: a) c_e - the operating cost; b) c_{ea} - the active power cost; c) c_{er} - the reactive power cost.

The optimum point resulted for: $D = 826.1$ mm, $\delta = 1.502$ mm, and the optimization resulted in a decrease of the total cost $\Delta c_t = 4.536\% = 18300$ €.

TABLE 1

Criterion	C_e (€)	$C_{e,a}$ (€)	$C_{e,r}$ (€)	$C_{e,a}/C_{er}$ (r.u.)	m_p (r.u.)	i_p (r.u.)	m_m (r.u.)
Variant							
Values imposed	-	-			≥ 1.05	≤ 5.5	≥ 2.1
V_m - Real var.	403400	217000	186400	1.164	1.184	5.455	2.627
V_o - Opt. var.	385100	218200	166900	1.307	1.050	5.346	2.504

B. Study on the optimization of the main dimensions

For the pair of variables D and δ (diameter and air gap), possessing the largest weights in the optimization process, a supplementary analysis was performed considering a single variable. Due to the restrictions imposed by the design theme, taking into account the proposed variation domain for the studied variable, only one area of the domain is allowed. This may be also noticed while performing the simulations for the optimization and previously presented.

In Fig. 3 are presented the per unit plots for the analyzed criterion and the associated costs c_e - operation cost and c_{ea} , c_{er} - active and reactive power costs. The two variables greatly change the reactive power consumption, which has an important weight in the optimization, $c_{er} \approx 0.46 * c_e$. It results that, in order to reduce the operating cost, the most important aspect is to reduce the air gap and to increase the diameter of the machine as much as the imposed restrictions allow.

In Fig. 4 are analyzed the variation curves for m_m , m_p , i_p - the maximum / strating torque and the start current, and important variations may be noticed for these quantities.

The lower limit of the variable δ - the air gap is determined by the increase of the start current over the imposed limit. All of the starting current limits the variable D - the diameter on a certain area, $D = (650 \div 750)$ mm, and the superior limit is imposed by the decrease of the starting torque.

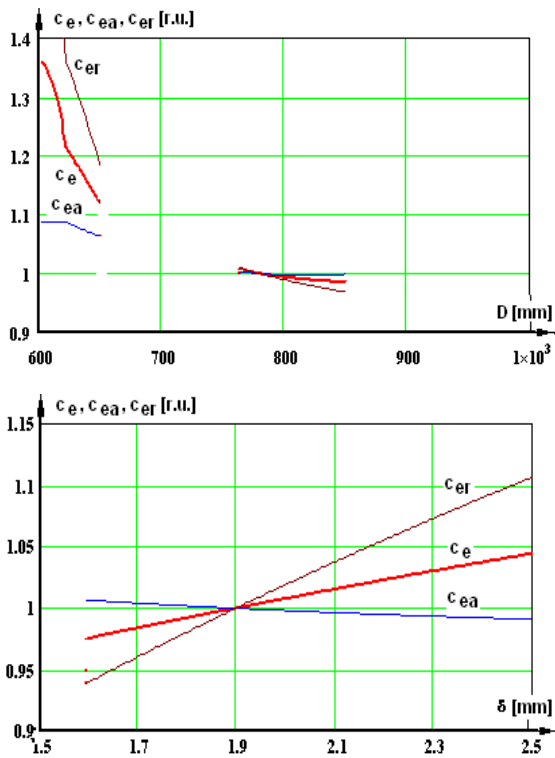


Fig. 3. Variation curves for c_e , c_{ea} , c_{er} - operating costs of active / reactive power for: a) variable D - machine diameter; b) the variable δ - the size of the air gap

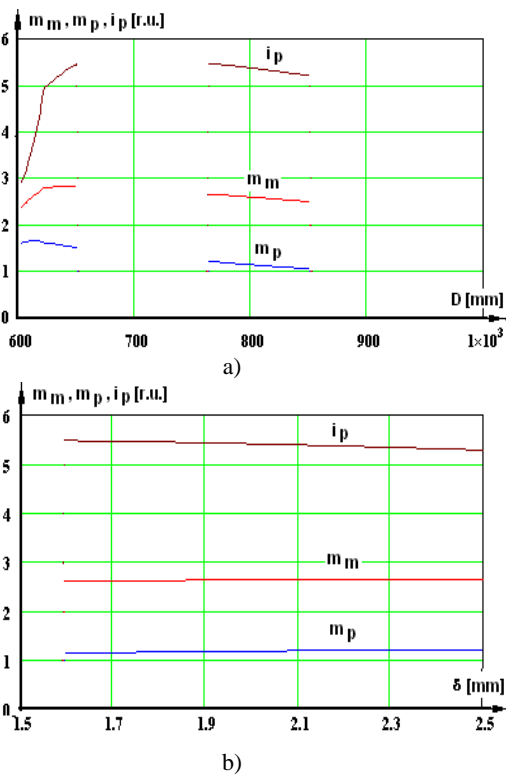


Fig. 4. Variation curves for m_m , m_p , i_p - the maximum / starting torques and the starting current for: a) variable D - machine diameter; b) variable δ - the size of the air gap.

C. Optimization of the stator slot geometry

A study was performed for optimizing the geometry of the stator slot, with respect to the established criterion, $C_e = \text{minimum}$.

The variables considered are: $\beta_{c1} = b_{c1}/t_1$ - the slot shape factor (b_{c1} , t_1 - the width of the slot and the tooth pitch), b_{01} , h_{01} - the dimensions of the isthmus. With respect to the most important variables β_{c1} and h_{01} , a simulation was performed, the results being presented in Fig.5.

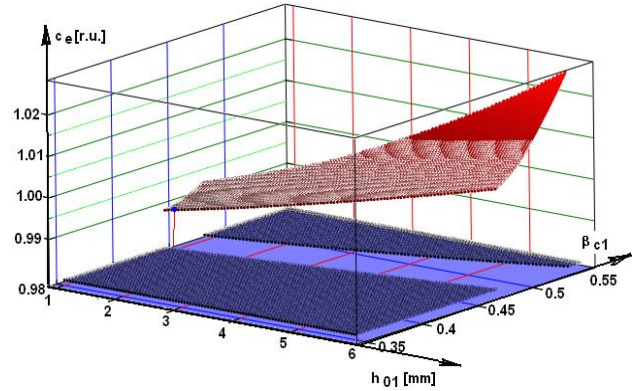


Fig. 5. Response areas for c_e - the operating cost when the pair of variables β_{c1} and h_{01} is considered.

The optimum solution resulted for the following variable values: $\beta_{c1} = 0.451$, $b_{01} = 10.23$ mm, $h_{01} = 1.53$ mm.

The number of analyzed versions was $N_t = 747900$ motors, and in this case resulted a decrease of the operating cost by $\Delta c_e = 0.967\% = 3900$ €.

TABLE 2

Version \ Criterion	C_e (€)	$C_{e.a}$ (€)	$C_{e.r}$ (€)	$C_{e.a}/C_{e.r}$ (r.u.)	m_p (r.u.)	i_p (r.u.)	m_m (r.u.)
Values imposed	-	-	-	-	≥ 1.05	≤ 5.5	≥ 2.1
V_m - Real ver.	403400	217000	186400	1.164	1.184	5.455	2.627
V_{α} - Opt. ver.	399500	218500	183600	1.175	1.067	5.207	2.507

D. Optimization of rotor slot geometry

A study was performed for optimizing the geometry of the rotor slot, considering the established criterion $C_e = \text{minimum}$. The variables are: $\beta_{c2} = h_{c2}/b_{c2}$ - the shape factor of the slot (b_{c2} , h_{c2} the width and height of the slot), b_{02} , h_{02} - the dimensions of the isthmus.

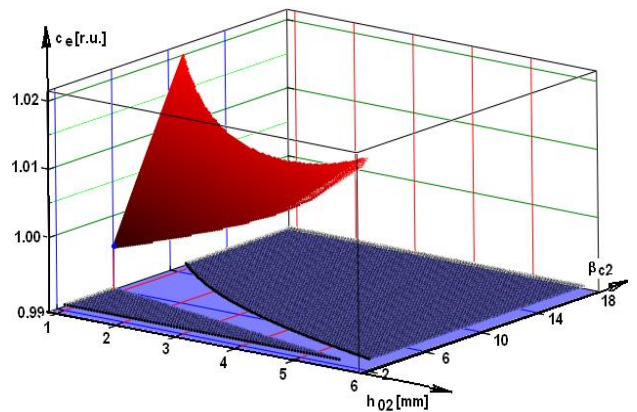


Fig. 6. The response areas for c_e - the operating cost when the pair of variables β_{c2} and h_{02} is considered.

The simulation was carried out with respect to the most important variables β_{c2} and h_{02} , the result of which being presented in Fig. 6.

The optimal solution resulted for the following values of the variables: $\beta_{c2}=5.436$, $b_{02}=1.648$ mm, $h_{02}=1.102$ mm.

The number of analyzed versions was $N_t=375800$ motors, and in this case a small decrease of the operating cost resulted, by $\Delta c_e=0.396\%$, $=1600$ €.

TABLE 3

Version \ Criterion	C_e (€)	$C_{e.a}$ (€)	$C_{e.r}$ (€)	$C_{e.a}/C_{e.r}$ (r.u.)	m_p (r.u.)	i_p (r.u.)	m_m (r.u.)
Values imposed	-	-	-	-	≥ 1.05	≤ 5.5	≥ 2.1
V_m - Real ver.	403400	217000	186400	1.164	1.184	5.455	2.627
V_o - Opt. ver.	401800	216900	184900	1.173	1.217	5.500	2.693

E.Total optimization

The optimization study is further performed with respect to all of the analyzed variables (D , δ , β_{c1} , b_{01} , h_{01} , β_{c2} , b_{02} , h_{02}). No graphical representations can be provided for this case, but the results are listed in table no. 4.

The optimal solution resulted for the following values of the variables: $D=867.1$ mm, $\delta=1.484$ mm, $\beta_{c1}=0.483$, $b_{01}=10.9$ mm, $h_{01}=1.053$ mm, $\beta_{c2}=4.494$, $b_{02}=1.60$ mm, $h_{02}=1.02$ mm.

In order to solve the problem, a number of $N_t=22450000$ motor versions was considered, and the optimal solution resulted was obtained with a decrease of the operating cost by $\Delta c_e=9.075\%$, $=26100$ €.

TABLE 4

Version \ Criterion	C_e (€)	$C_{e.a}$ (€)	$C_{e.r}$ (€)	$C_{e.a}/C_{e.r}$ (r.u.)	m_p (r.u.)	i_p (r.u.)	m_m (r.u.)
Values imposed	-	-	-	-	≥ 1.05	≤ 5.5	≥ 2.1
V_m - Real ver.	403400	217000	186400	1.164	1.184	5.455	2.627
V_o - Opt. ver.	377300	218000	159200	1.369	1.060	5.489	2.604
Variation in %	9.075%	0.461%	14.59%	17.61%	10.50%	0.623%	0.875%

Table no. 5 collects the results of the analyzed optimizations (by groups of variables and the end result), in order to establish which variables are most relevant. In this way, the variables with low weights are dropped, the volume of computations decreases and, consequently, the computation time is reduced.

Table no. 5

Optimization \ Criterion	C_e (€)	$C_{e.a}$ (€)	$C_{e.r}$ (€)	$C_{e.a}/C_{e.r}$ (r.u.)	m_p (r.u.)	i_p (r.u.)	m_m (r.u.)
Values imposed	-	-	-	-	≥ 1.05	≤ 5.5	≥ 2.1
The real version	403400	217000	186400	1.164	1.184	5.455	2.627
Main dimensions	385100	218200	166900	1.307	1.050	5.346	2.504
Stator slot dimensions	399500	218500	183600	1.175	1.067	5.207	2.507
Rotor slot dimensions	401800	216900	184900	1.173	1.217	5.500	2.693
Optimization for all variables	377300	218000	159200	1.369	1.060	5.489	2.604

IV.CHARACTERISTICS OF THE OPTIMIZED MOTOR

In order to meet the imposed requirements, the resulted solution is a motor with a cage made of high crossing bars, with slightly variable parameters (affected by the current repression and the magnetic saturation).

For the optimal asynchronous motor solution, which fulfills all the conditions required by the operation of the coal mill, the operating characteristics were depicted in Fig.7, while the current diagram was plotted in Fig.8.

In Fig.7.c is depicted the evolution of the partial and total losses with respect to the motor load. Considering the operating characteristics presented in Fig.7, an increase of $\cos\phi=0.878$ and $\eta=0.923$ may be noticed, leading to a low operating cost.

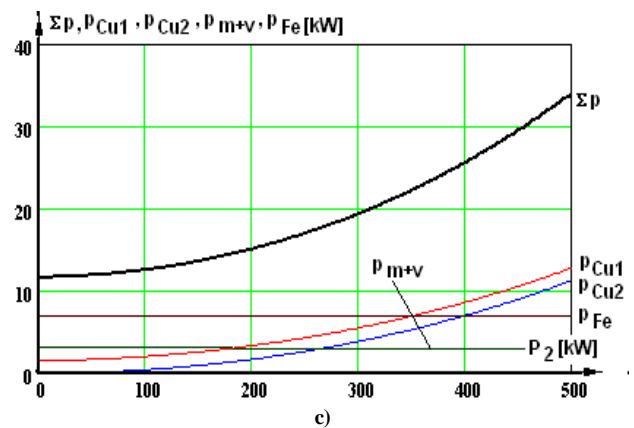
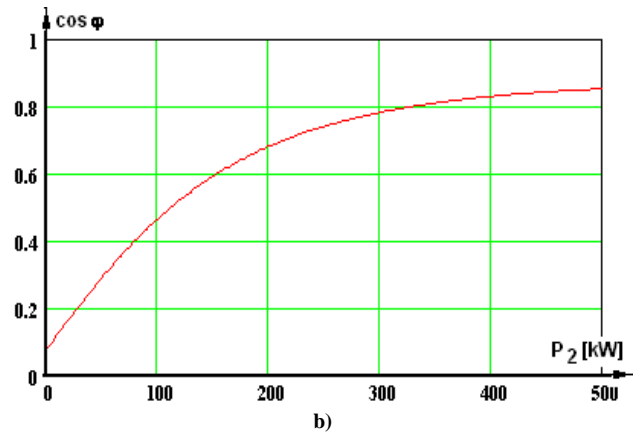
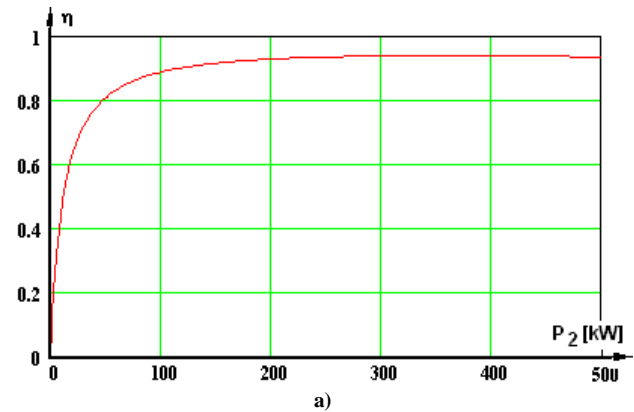


Fig. 7. Operating characteristics of the optimized motor: a) efficiency curve; b) power factor curve; c) variation curves for the motor losses: P_{Cu1} , P_{Cu2} - losses in stator / rotor windings, P_{Fe} - iron losses, P_{m+v} - mechanical losses, Σp - total losses.

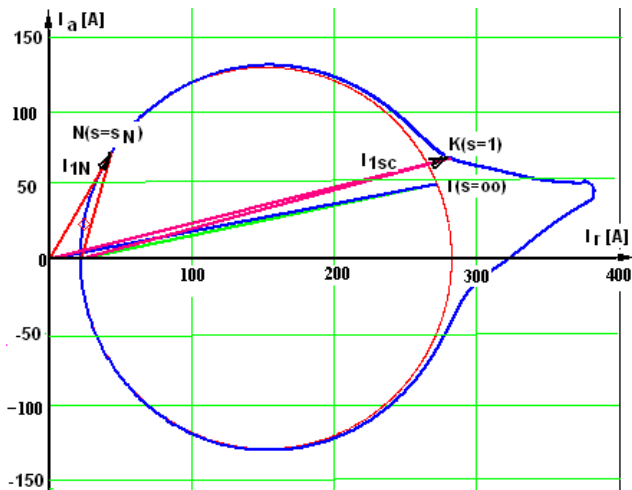


Fig. 8. Current locus for the optimized asynchronous motor.

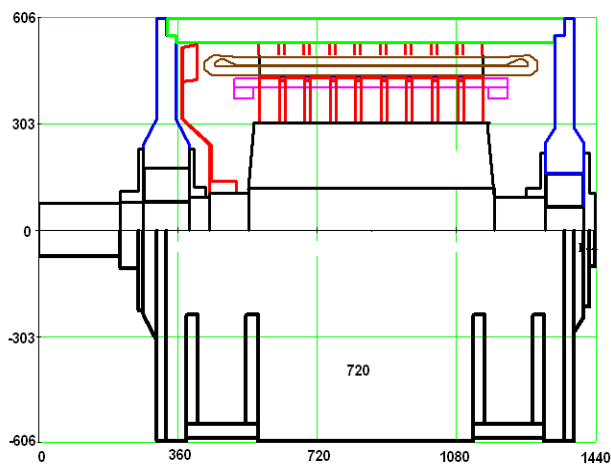


Fig. 9. Longitudinal section and view through the optimized motor.

CONCLUSIONS

The study and the simulations performed had as main objective the identification of the important variables involved in the optimization for obtaining $C_e = f(x) = \text{minimum}$, in order to substantially reduce the number of variables, and finally the computation effort necessary for the optimization.

For constant electromagnetic stresses, by modifying the main constructive dimensions and the stator and rotor slots, a significant decrease of the operating cost with $\Delta C_e = 9.075\% = 26100 \text{ €}$ resulted, as compared to the existing motor version, while keeping the restrictions imposed by the specifics of the drive system.

The presented simulations and results prove that the geometries of the stator and rotor slots affect the operating cost.

Source of research funding in this article: Research program of the Electrical Engineering Department financed by the University of Craiova.

Contribution of authors:

First author – 50%

First co-author – 20%

Second co-author – 15%

The third co-author – 15%

Received on July 17, 2020

Editorial Approval on November 15, 2020

REFERENCES

- [1] J. L. Besnerais, V. Lanfranchi, M. Hecquet, and P. Brochet, "Multi-objective optimization of induction machines including mixed variables and noise minimization", *IEEE Trans. on Mag.*, vol. 44, no. 4, Apr. 2008.
- [2] M. Centner, U. Schäfer, "Machine design software for induction machines," in *Proc. ICEM*, Vilamoura, Portugal, 2008, pp. 1–4.
- [3] C.U. Brunner, "International Standards for Electric Motors", Standards for En.Efficiency of Electric Motor Systems (SEEM), 2007, pp. 6-10.
- [4] D. Necula, N. Vasile, M.F. Stan, "The Electrical Machines Impact on the Environment and Solution to reduce its", *Scientific Bulletin of the Electrical Engineering Faculty*, no.3(17)/2011, Bibliotheca Publishing House, Târgoviște, 2011, pp. 37 – 42.
- [5] I. Vlad, A. Campeanu, S. Enache, *Computer-aided design of asynchronous motors. Optimization problems*. Universitaria Publishing House, Craiova, 2011 (in Romanian).
- [6] *** CEI 60034-2-1 Standard: "Rotating electrical machines-Part 2-1. Standard methods for determining losses and efficiency from tests", Edition 1.0, 2007.
- [7] A. Câmpeanu, "Nonlinear dynamical models for the saturated induction machine", *Rev. Roum. Sci. Techn.-Electrotech. et Energ.*, Vol 46, No. 1, pp 89-99, January-March 2001.
- [8] A. Boukhelifa, M. Kherbouch, A. Cheriti, R. Ibtouen, O. Touhami, R. Tahmi, "Stator current minimization by field optimization in induction machine", *International Conference on Electrical, Electronic and Computer Engineering, ICEEC'04*, 2004.
- [9] W. N. Fu, S. L. Ho, and H.C. Wong, "Design and analysis of practical induction motors", *IEEE Trans. on Magnetics*, vol. 37, no. 5, pp. 3663-3667, 2001.
- [10] S. Curteanu, *Numerical computation and symbols in MATHCAD*, Matrix Rom Publishing House, Bucharest, 2004 (in Romanian).
- [11] G. Liuzzi, S. Lucidi, F. Parasiliti, M. Villani, "Multiobjective optimization techniques for the design of induction motors", *IEEE Trans. on Magnetics*, vol. 39, no. 3, May 2003.
- [12] D. Samarkanov, F. Gillon, P. Brochet, D. Laloy, "Techno-economic Optimization of Induction Machines: an Industrial Application", *ACEMP - Electromotion 2011*, Istanbul –Turkey, 2011, pp. 825-830.
- [13] I. Vlad, A. Campeanu, S. Enache, G. Petropol, "Operation Characteristics Optimization of Low Power Three-Phase Asynchronous Motors", *AECE Journal*, Volume 14, Issue 1, Year 2014, pp. 87-92.
- [14] J.P. Wiecek, Ö. Gözl, Z. Michalewicz, "An evolutionary algorithm for the optimal design of induction motors", *IEEE Trans. on Magnetics*, Vol. 34 No.6, 1998, pp. 3882-3887.

Program for Monitoring Operation Regimes of Low-Power Electrical Machines

Sorin Enache*, Ion Vlad*, Monica-Adela Enache*

* University of Craiova/Faculty of Electrical Engineering, Craiova, Romania, senache@em.ucv.ro

Abstract – In this paper there are presented details about a program for monitoring steady states and dynamic regimes of low-power electrical machines. The program allows viewing the variation waves of the main electrical quantities, their harmonic content and the relative position of the characteristic phasors. The program advantages are mentioned and there have exemplified some data acquisitions, carried out for a few concrete situations. The main work windows from the Instrument menu are detailed. There have also been presented the results obtained by monitoring the operation of two motors, a three-phase asynchronous motor with single-phase supply and a single-phase asynchronous motor. A part of the conclusions obtained could be mentioned as follows: a) for the case of three-phase asynchronous motor with single-phase supply, we noticed that a voltage increase leads to an increase of the inductive phase shift of the current I_1 , the phase shift of the current I_2 (measured on the phase in series with the capacitor) remains practically unchanged, the capacitive phase shift of the current I_3 increases and the distortion degree of the current I_1 decreases; b) for the case of the single-phase asynchronous motor we noticed that in load operation (at rated voltage) a decrease of the phase shift between the current and voltage corresponding to the main winding occurs and the current distortion degree increases when the load increases. The paper ends with conclusions and references.

Cuvinte cheie: *masini electrice de mica putere, regimuri dinamice, program de monitorizare, analiza armonica, fazori.*

Keywords: *low-power electrical machines, dynamic regimes, monitoring program, harmonic analysis, phasors.*

I. INTRODUCTION

For monitoring operation regimes of electrical machines, especially when it comes to distorting dynamic or steady states, it is necessary to use high sampling frequency data acquisition systems [1], [2], [3].

Their interface, having a facile use, is ensured by monitoring programs.

These programs ensure both data acquisition, their processing and results displaying [4], [5], [6].

The program presented below belongs to this category.

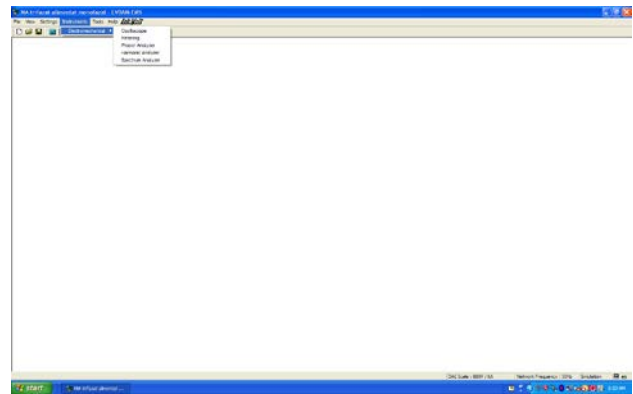
It ensures an adequate use of the test stand detailed in [7], stand used for monitoring the operation of electrical machines rated under 1kW.

II. PROGRAM DESCRIPTION

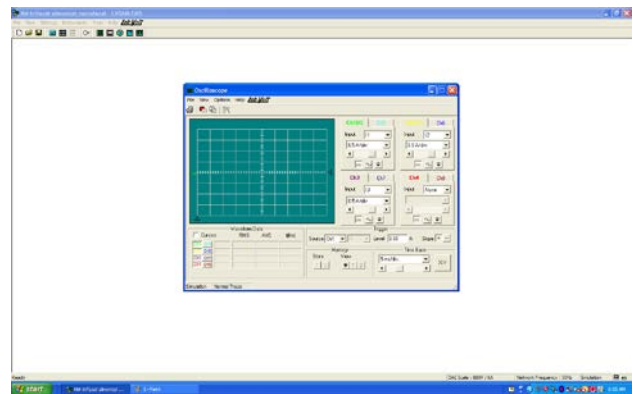
The program is built around a menu displayed in the upper part of the screen.

The main sub-menu of it is "Instruments" (Fig. 1.a).

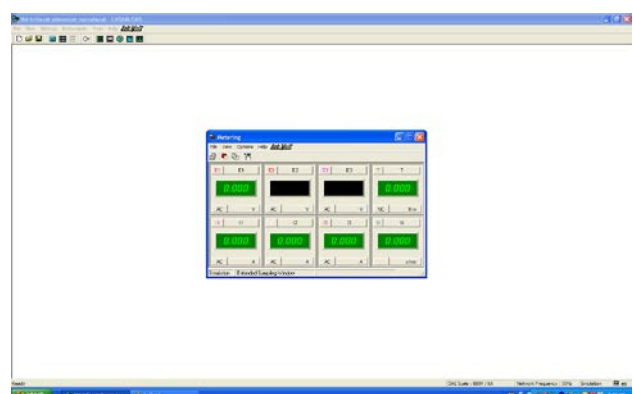
This sub-menu contains five working tools, materialized in five windows: Oscilloscope (Fig. 1.b), Metering (Fig. 1.c), Phasor Analyser (Fig.1.d), Harmonic Analyser (Fig. 1.e) and Spectrum Analyser (Fig. 1.f).



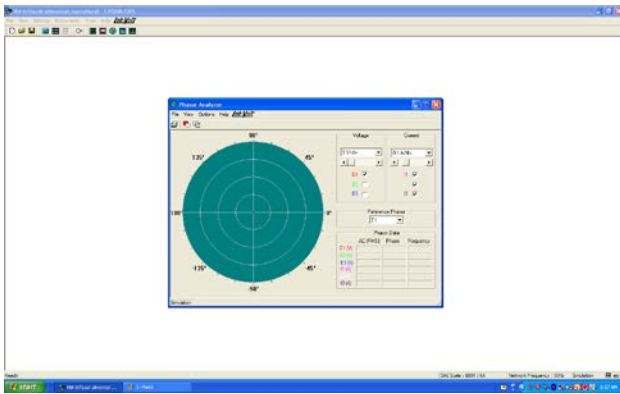
a)



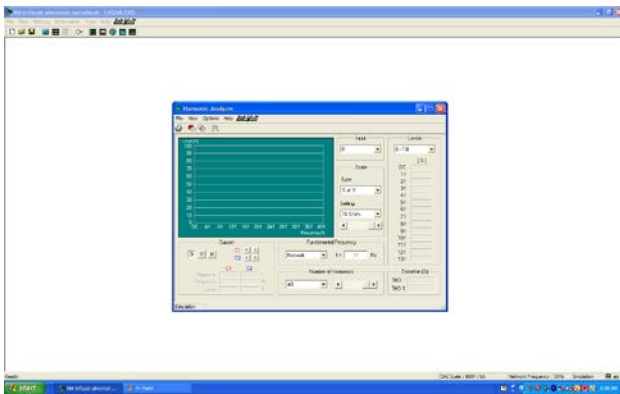
b)



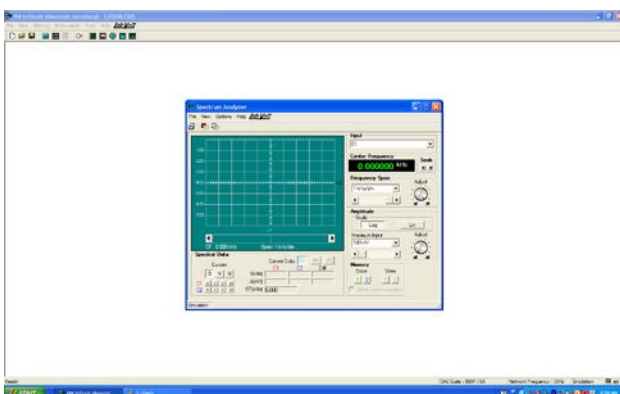
c)



d)



e)



f)

Fig. 1. Windows from the menu "Instruments".

Some examples of using these tools will be presented below.

III. MONITORING EXAMPLES

Two monitoring cases are presented in the following:

- A. case of a three-phase asynchronous motor with single-phase supply;
- B. case of a single-phase asynchronous motor.

A. For the case of a three-phase asynchronous motor with single-phase supply, from the multitude of tests carried out, there are presented a few of them:

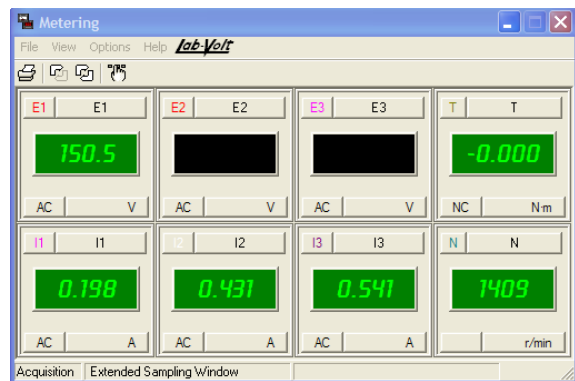
- test at $E_1=150$ V, $C_1=5$ μ F, $M_r=0$ Nm;
- test at $E_1=20$ V, $C_1=5$ μ F, $M_r=0$ Nm.

The notations meaning are presented in [8].

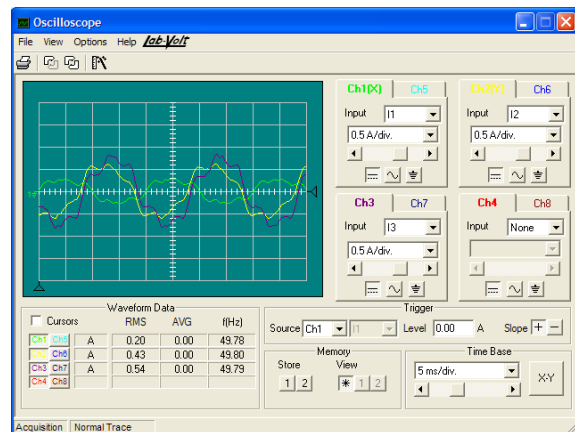
The root-mean-square value of the voltage, E_1 , and the resistant torque value can be modified with the test stand [9], [10].

The test from Fig. 2 has been carried out for $E_1=150$ V, the smallest voltage for which the motor enters the speed (its speed is close to the rated one - 1409 r.p.m). From Fig. 2.a it results that the root-mean-square values of the phase currents are different ($I_1=0,198$ A, $I_2=0,431$ A, $I_3=0,541$ A). Moreover, according to Fig. 2.c, where the voltage E_1 has been chosen as a phase origin, the current I_1 is inductive ($\varphi=-50,7^\circ$) and I_2 ($\varphi=175,5^\circ$) and I_3 ($\varphi=148,3^\circ$) are capacitive.

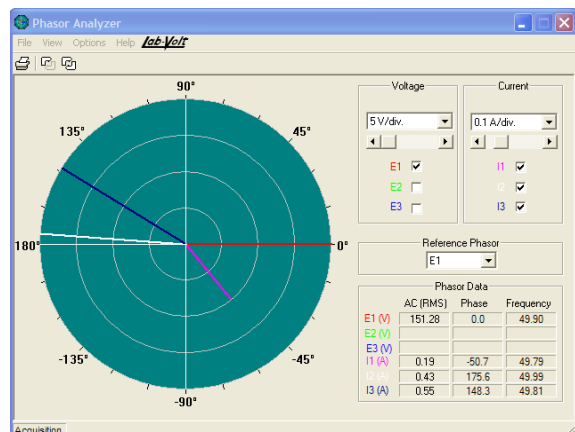
According to Fig. 2. b, d, e and f, the phase currents are deeply distorted (mainly because of the supply source). The current having the highest content of harmonics is I_1 which has THD=24,5.



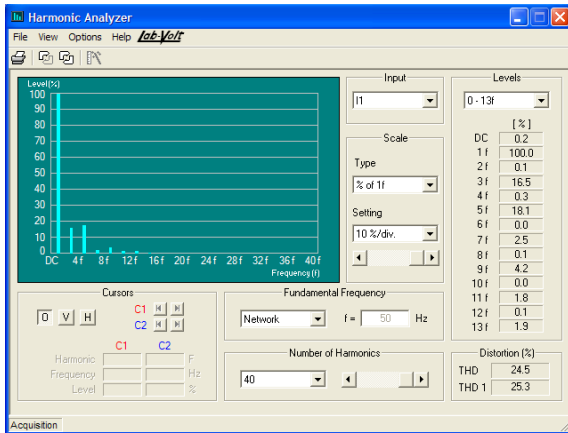
a)



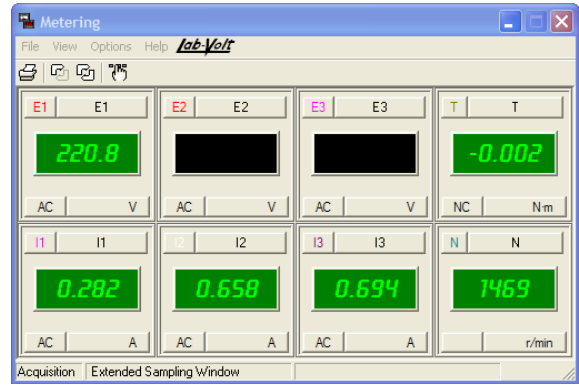
b)



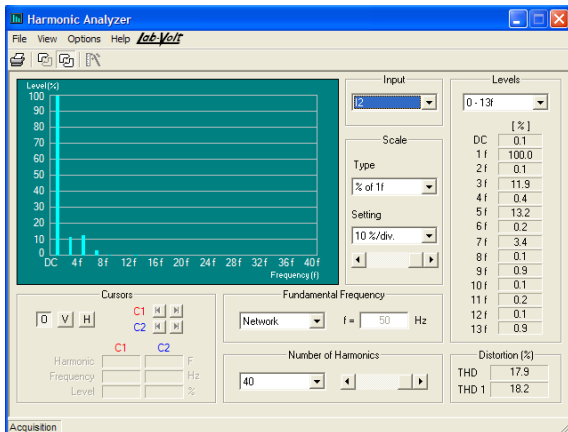
c)



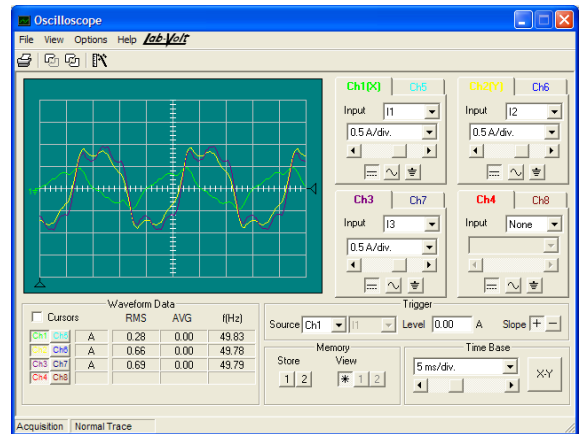
d)



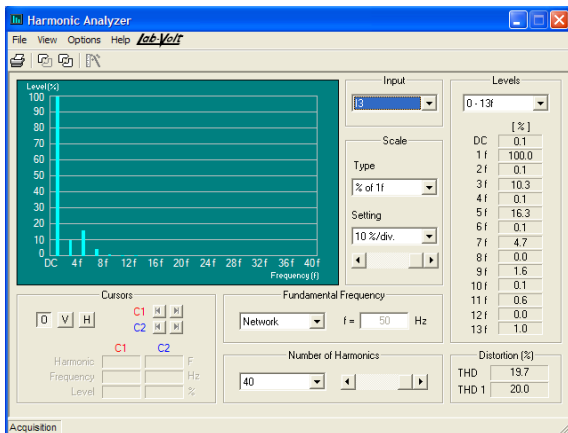
a)



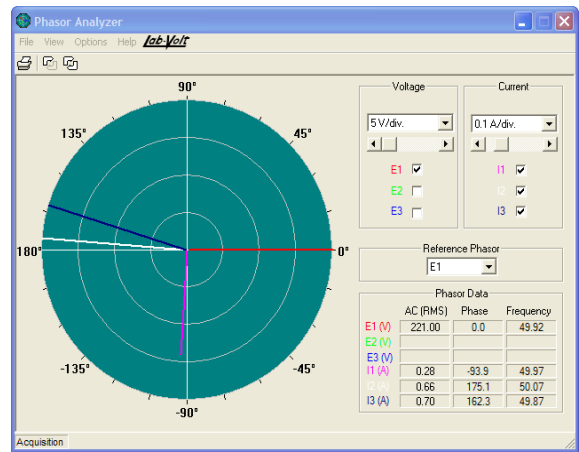
e)



b)



f)



c)

Fig. 2. $E_1=150$ V, no-load operation, $C_1=5$ μ F.

The case when the supply voltage is the rated one, $E_1=220$ V, is depicted in Fig.3.

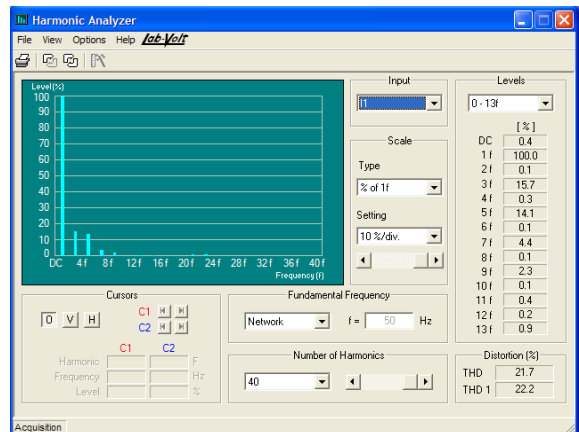
The following modifications can be observed in comparison with the previous situation:

- the inductive phase shift of the current I_1 increases to the value $\varphi=-93,9^\circ$;

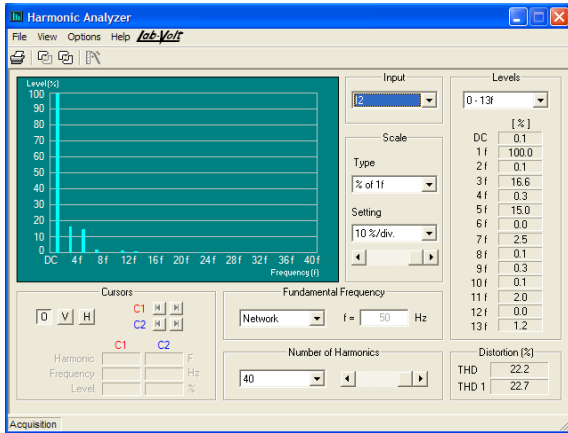
- the phase shift of the current I_2 (measured on the phase in series with the capacitor) remains practically unchanged ($\varphi=175,1^\circ$);

- the capacitive phase shift of the current I_3 increases to the value $\varphi=162,3^\circ$.

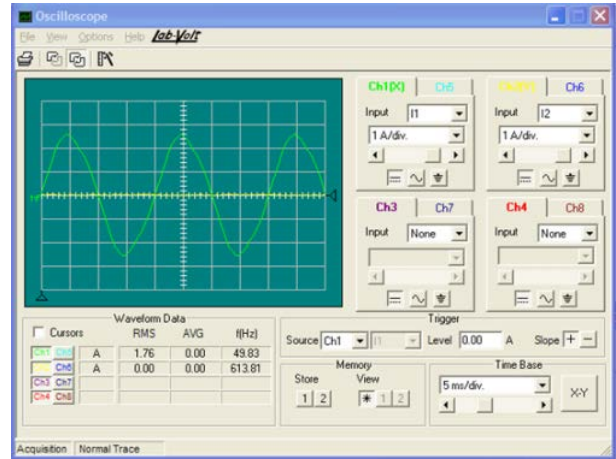
- the distortion degree of the current I_1 decreases to THD=21,7.



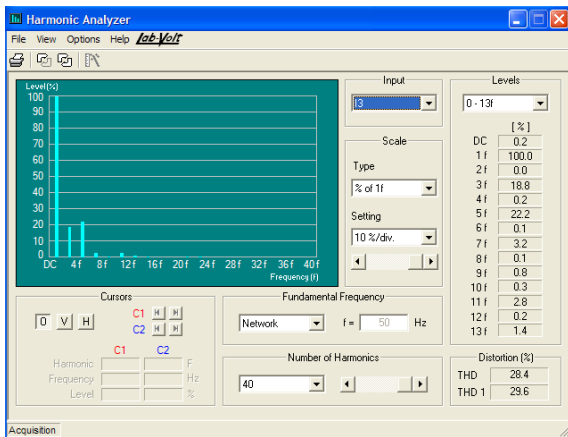
d)



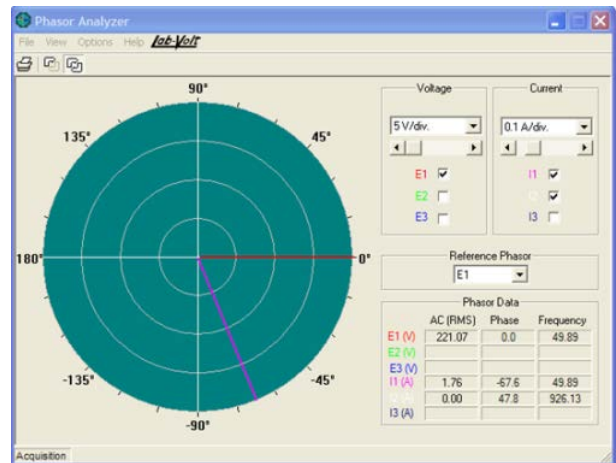
e)



b)



f)



c)

Fig. 3. $E_1=220$ V, no-load operation, $C_1=5\mu\text{F}$.

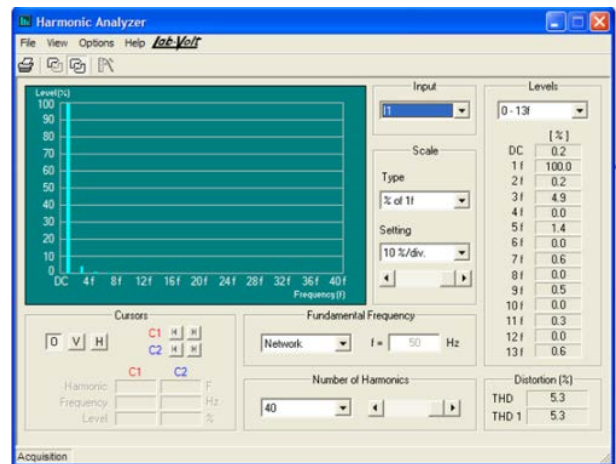
B. For the case of a single-phase asynchronous motor there have been obtained the graphics depicted in Figures 4 and 5.

B1) Operation at the rated voltage (220 V), no-load

For this case there have been obtained the results presented in Figure 4.

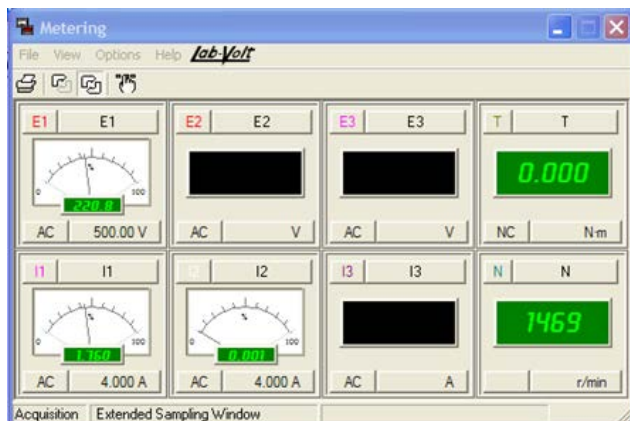
In case of no-load operation at the rated voltage (Fig. 4) it is noticed that the main winding is the only one supplied (Fig. 4 a, b and c).

That circuit is mostly inductive, fact confirmed by the phase shift presented in Figure 4.c (67,6 electrical degree).



d)

Fig. 4. Characteristics obtained at 220V, no-load.



a)

B2) Operation at the voltage supply 220 V and load of 1,3 Nm

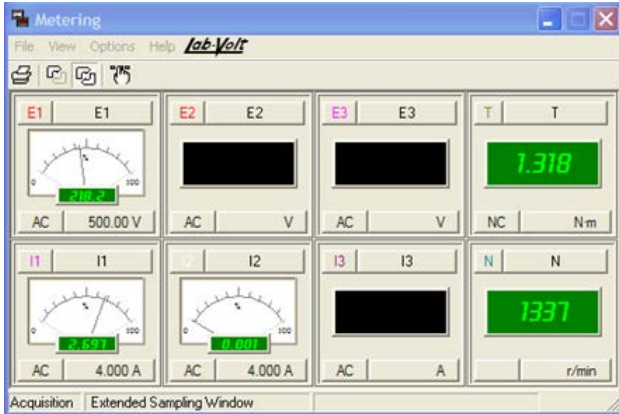
The same testing method as in the previous situations has also been used in this case.

There have been obtained the results detailed in Fig. 5.

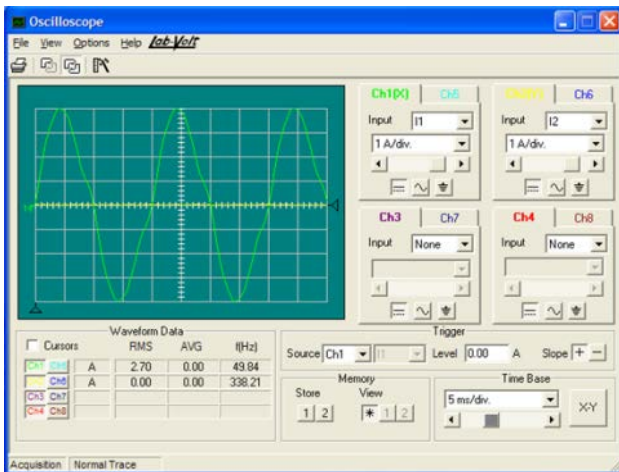
As expected, the speed has a slight decrease in case of load operation, because of the „rigid” feature of the motor mechanical characteristic (the speed decreases from 1469

r.p.m, at null resistant torque, down to 1337 r.p.m, at a resistant torque of 1,3 Nm).

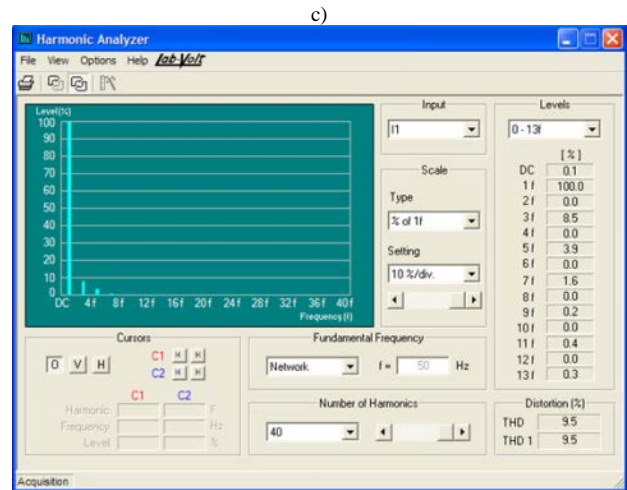
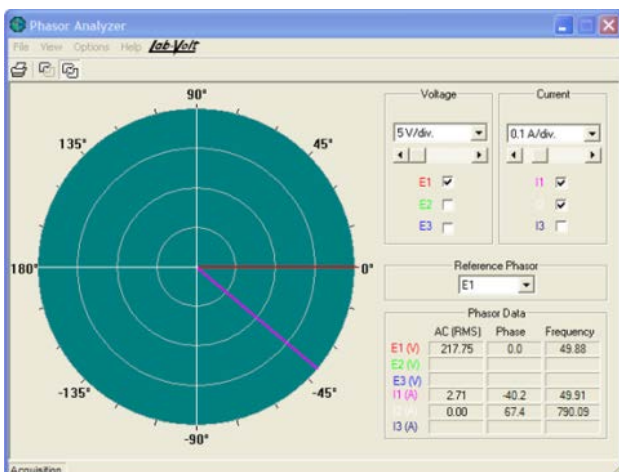
In case of load operation (rated voltage) a decrease of the phase shift between the current and the voltage corresponding to the main winding is observed (the phase shift decreases down to 40,2 electrical degrees as against the value of 67,6 electrical degrees, in case of no-load operation). The distortion degree of the current also increases with the load increase (for the example from the previous figures, the third order harmonic represents 8,5 % as against the value of 4,9 % in case of no-load operation).



a)



b)



c)

Fig. 5. Characteristics obtained at 220 V, load operation.

IV. CONCLUSIONS

The research carried out has revealed the following conclusions:

- the program presented in the paper enable viewing some electrical signals in dynamic regime, their harmonic analysis and the relative position of the characteristic phasors;

- for the case of the three-phase asynchronous motor with single-phase supply, it is noticed that at the voltage increase, the inductive phase shift of the current I_1 increases, the phase shift of the current I_2 (measured on the phase in series with the capacitor) remains practically unchanged, the capacitive phase shift of the current I_3 increases and the distortion degree of the current I_1 decreases;

- for the case of the single-phase asynchronous motor it is noticed that in case of load operation (rated voltage) a decrease of the phase shift between the current and the voltage corresponding to the main winding occurs and the distortion degree of the current increases with the load increase.

A few contributions of the authors could be mentioned:

- the program, the basic structure of which exists, has been improved by the authors of this paper, by adding a module of harmonic analysis of the acquired signals;

- the initial version, functional in an older version of Windows, has been adapted for working in Windows 10.

Source of research funding in this article: Research program of the Electrical Engineering Department financed by the University of Craiova.

Contribution of authors:

First author – 50%

First coauthor – 25%

Second coauthor – 25%

Received on June 08, 2020

Editorial Approval on November 16, 2020

REFERENCES

- [1] J. Svarny, L. Pusman, P. Turjanica, M. Sykora, "Data Acquisition Unit for On-Site Diagnostics of Air Compressors", *2020 International Conference on Diagnostics in Electrical Engineering (Dagnostika)*, Pilsen, Czech Republic, 2020.
- [2] X. Li, W. An, H. Hu, P. Li, X. Jiang, "Development of data acquisition system for CNC machine tools", *2020 IEEE International Conference on Advances in Electrical Engineering and Computer Applications (AEECA)*, 25-27 Aug. 2020, Dalian, China, 2020.
- [3] F. Hamann, G. Mesones, "Development of a hybrid system for automatic identification of brushed direct current motors", *2020 IEEE XXVII International Conference on Electronics, Electrical Engineering and Computing (INTERCON)*, 3-5 Sept. 2020, Lima, Peru, 2020.
- [4] D. K. Chaturvedi, S. Iqbal, M. P. Singh, "Condition monitoring of induction motor", *2015 International Conference on Recent Developments in Control, Automation and Power Engineering (RDCAPE)*, 12-13 March 2015, Noida, India, 2015.
- [5] B. Adli, P. H. Rusmin, „Vibration Measuring Tools For Rotary Pumping Machine With Accelerometer MEMS Sensor”, *2020 FORTEI-International Conference on Electrical Engineering (FORTEI-ICEE)*, 23-24 Sept. 2020, Bandung, Indonesia, 2020.
- [6] P. Modesto, T. Estrabis, R. Cordero, "Analysis about the Application of Frequency-Domain Multiplexing in Data Acquisition for Vector Control", *2020 IEEE XXVII International Conference on Electronics, Electrical Engineering and Computing (INTERCON)*, 3-5 Sept. 2020, Lima, Peru, 2020.
- [7] M. A. Enache, A. Campeanu, S. Enache, I. Vlad, "Testing Stand for Low-Power Electrical Machines", *International Conference on Applied and Theoretical Electricity ICATE 2018*, Craiova, Romania, 2018.
- [8] S. Enache, A. Campeanu, I. Vlad, M.A. Enache, "Aspects Regarding Tests of Three-Phase Asynchronous Motors with Single-Phase Supply", *2019 16th Conference on Electrical Machines, Drives and Power Systems (ELMA)*, Varna, Bulgaria, 2019.
- [9] ***, Virtual Laboratory and Equipments, User Guide, *Lab-Volt*, 32359-E0, 2017.
- [10] ***, Data Acquisition and Management System, User Guide, *Lab-Volt*, 30328-E0, 2017.

Contributions Regarding the Monitoring in the Command Center of the Anti-Hail Launch Pads

Sorin Stepan, Gheorghe Manolea*

Conestoga College, Ontario, Canada, e-mail: sostepan@yahoo.com

* University of Craiova / Department of Electromechanical, Environmental and Applied Informatics, Craiova, Romania
e-mail: ghmanolea@gmail.com

Abstract – This paper describes an Internet-connected radio remote control designed for the positioning system of the launching pad of anti-hail missiles used by the Romanian Anti-Hail System. The remote control works on the ISM band of 433 MHz and was successfully tested on a small size experimental model of the launch pad. The azimuth and elevation position can be locally controlled by the operator, with the possibility of monitoring and even controlling the launch pad from the Command Center, over the Internet. The remote control uses a touch screen display on the operator side and a PLC connected to the launch pad. The commands on the touch screen are grouped into three pages: manual positioning, automatic positioning, and a list of recorded events. Sending the coordinates to the launch pad and firing the missiles are considered events, automatically recorded on an SD card or USB flash drive attached to the remote control. Communication between the touch screen and the PLC is realized by two RF transceivers using LoRa modulation. The touch screen display is connected to the Internet, making it possible to remotely monitor and control the launch pad using an Internet-connected computer. The access to the remote control is password protected and can be disabled by the local operator.

Cuvinte cheie: telecomandă, anti-grindină, PLC, ecran tactil, lansator de rachete, sistem de poziționare, ISM, LoRa.

Keywords: remote control, anti-hail, PLC, touch screen, missiles launch launch pad, positioning system, ISM, LoRa.

I. INTRODUCTION

This research is intended to overcome a problem found when the authors visited an anti-hail Zonal Command Center and an anti-hail Local Unit. It has been found that the launching launch pads used by the anti-hail system in Romania are positioned manually, or using temporary cables, with no possibility to monitor the launch pad position from the Command Center [1], [2], [3].

The technical solution described in this paper speeds up the launch pad positioning, eliminates the need for the temporary cables, and makes possible monitoring and controlling the launching launch pad over the Internet.

II. THE REMOTE CONTROL

The remote control works on a two ways radio communication channel between the touch screen and the PLC, using AS32-DTU-100 RF transceivers. A 178 mm touch screen is used by the operator to send commands to the launch pad, and to display the launch pad position and the presence and type of the missiles on the launch pad (Fig. 1).

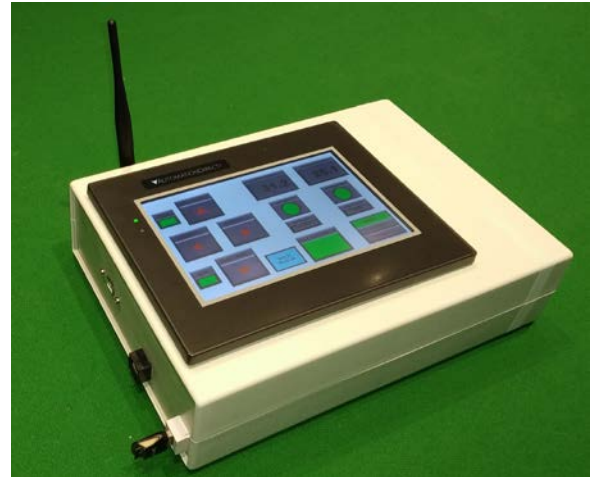


Fig. 1. The remote control

The electrical block schematic of the remote control is shown in Fig. 2.

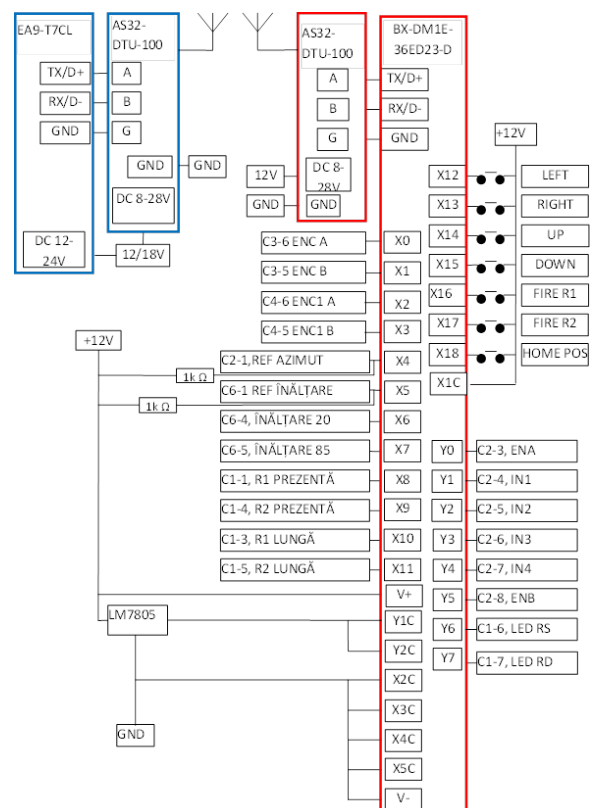


Fig. 2. The remote control block schematic

The commands entered by the operator on the touch screen are grouped into three pages of the screen:

- manual positioning,
- automatic positioning, and
- list of events produced.

The manual controls screen is shown in Fig. 3.

The operator holds the arrow labeled buttons until the desired position of the launch pad is reached. The presence and type of the missiles loaded are displayed on the touch screen, along with the azimuth and elevation coordinates.

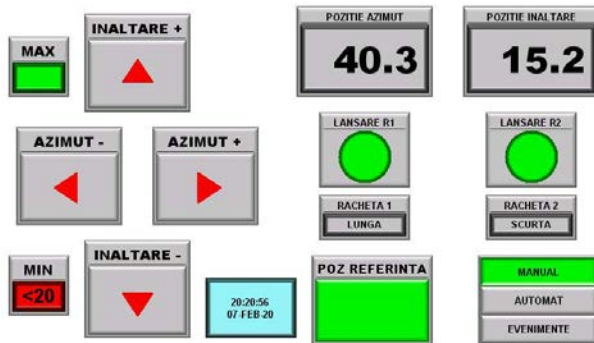


Fig. 3. The manual positioning controls screen

The automatic positioning screen is shown in Fig. 4.



Fig. 4. The automatic positioning screen

From this screen, the operator can prescribe the azimuth and elevation coordinates for the launch pad using a virtual keyboard that pops up on the touch screen when the azimuth or elevation prescribing buttons are depressed. After sending the coordinates, the launch pad moves automatically to the desired position.

The remote control is provided with SD card and USB memory ports. The third screen shows a list of events recorded on the external memory. The positioning of the launch pad using the "SEND COORDINATES" button and the missile launch are recorded as events, with a time stamp.

III. MONITORING THE LAUNCH PAD OVER THE INTERNET

For the launch pad monitoring in the Control Center, we proposed to connect the remote control to the Internet,

and we used, for this purpose, the Ethernet port of the EA9-T7CL touch screen is provided.

Monitoring the remote control involves, in addition to connecting to the internet, certain settings on the touch screen, as well as on the PLC and the router used by the touch screen to connect to the internet:

- Setting the IP address and DNS server for the touch screen, by accessing the Setup - Panel Network - Ethernet Port menus in the touch screen software.
- Setting the same IP address and DNS server for the PLC, by accessing the PLC menus - System Configuration - Internal Ethernet Port in the PLC software program.
- Activating the Web Server application by accessing the Setup - Panel Network - Web Server menus from the touch screen software.
- Activating the Remote Access application by accessing the Setup - Panel Network - Remote Access menus in the touch screen software program.
- Setting dedicated ports (80 for the Web Server application, respectively port 11102 for the Remote Access application) in the Port Forwarding menu of the router. These ports are suggested by the touch screen software program but are not mandatory.

To connect to the touch screen using a computer, a remote user only needs the public internet address of the touch screen, respectively the public IP of the router to which the touch screen is connected, the account username and the password. No other software is required, an ordinary internet browser is used.

After typing the touch screen public IP address in the browser, the main screen of the "Web Server" app shows up (Fig. 5).



Fig. 5. The main screen of the "Web Server" app

When accessing the "File List" link, a web page opens with the events recorded in the external memory of the remote control (SD card or USB flash, according to the settings used), grouped in text documents created daily.

The "Screen List" link opens a web page from which the remote control screens can be viewed (manual

positioning commands, automatic positioning commands, and recorded events).

The launch pad control is performed using the "Remote Access" application, included in the program loaded in the remote control. Accessing this application is done with the "Remote Access" link from the main screen of the Web Server application.

When accessing the "Remote Access" link, the main screen of the application opens (Fig. 6).

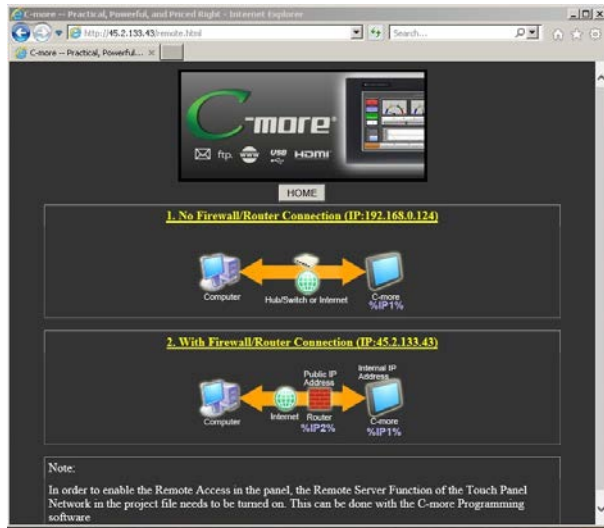


Fig. 6. Remote launch pad control using "Remote Access" app

In order to control the launch pad in the Command Center, the user must choose the connection option no.2, the one that involves the existence of a router. Option 1 can be used in a local network only.

Accessing the link has the effect of downloading the RemoteHMI_IP executable program, with the possibility of saving or running it on your computer. Saving this program, possibly with a shortcut on the desktop, makes it easier to use the Remote Access application later, in the future it is no longer necessary to go through the Web Server application. When running the application, after entering the account username and password, the image of the remote control touch screen shows in the internet browser. Using a mouse, the launch pad can be controlled as if the commands were performed locally on the touch screen (Fig. 7).

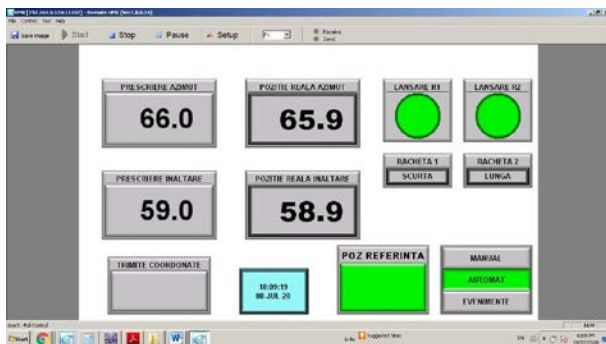


Fig. 7. RemoteHMI_IP app screen

V. CONNECTION TO THE LAUNCH PAD

The launch pad azimuth and elevation positioning are achieved by using two permanent magnet synchronous motors, provided with worm gears and incremental encoders, and driven by electrical drives (Fig. 8) [4], [5].



Fig. 8. Elevation motor and drive mounted on the ramp [4]

The PLC connected to the experimental model can be connected to the launch pad drives with minor adjustments:

- all the PLC terminals connected to 0V (GND) on the experimental model will be connected to the 0V control terminal on both drives
- terminals X0-X3 connected to the encoder outputs on the experimental model will be connected to the encoder outputs on the drives, using the buffered encoder output connectors. Ground terminal on the buffered output connectors on both drives will be connected.
- terminal X1C, connected to +12V on the experimental model, will be connected to +V terminal on the buffered encoder output on one drive
- Terminals Y0, Y1 and Y2 connected to ENA, IN1 and IN2 on the experimental model will be connected to control terminals DRIVE ENABLE, RUN FORWARD and RUN REVERSE on the drive used for azimuth positioning
- Terminals Y3, Y4 and Y5 connected to IN3 and IN4 and ENB on the experimental model will be connected to control terminals RUN FORWARD, RUN REVERSE, and DRIVE ENABLE on the drive used for elevation positioning
- an additional digital I/O module will be attached to the PLC, since the experimental model simulates the launch of two missiles, and the launch pad can carry eight missiles
- the PLC program and the local controls panel will be modified for eight missiles
- one constant in the PLC program will be modified, on each axis, to reflect the difference in the number of pulses the encoders provide for one degree of rotation of the launch pad.

VI. CONCLUSION

The 433 MHz Internet connected remote control is a technical solution that overcomes two challenges of the anti-hail launch pads operation: the use of temporary cables for the launch pad positioning and the lack of monitoring the launch pad from the Command Center. The remote control and its monitoring over the Internet were tested on an experimental model build for this purpose. The implementation of the remote control on the real launch pad can be done with minimal modifications of the equipment used.

ACKNOWLEDGMENT

The research was carried out during the elaboration of the doctoral thesis of the first author. The CITT models and experience in the field of hail systems were used for the doctoral research. Experimental measurements have been done in the Telecommunication Laboratory of Conestoga College, Ontario, Canada. The launch pad model and the remote control were built from own funds.

Contribution of authors:

First author – 90%

First coauthor – 10%

Received on June 11, 2020

Editorial Approval on November 14, 2020

REFERENCES

- [1] G. Manolea, L.I. Alboteanu, S. Stepan "Contributions to the Development of Complementary Equipment for the Romanian Anti-Hail System," 11th International Conference on Electromechanical and Power Systems, 12-13 October 2017, Chişinău.
- [2] G.Manolea ,L.I. Alboteanu , A. Novac , C. Şulea-Iorgulescu , S.Stepan , "Contributions Regarding the Modernization of the Anti-Hail Rocket Launcher Monitoring System," Annals of the University of Craiova, 2019, <https://ieeexplore.ieee.org/document/8905892>
- [3] G.Manolea, L.I.Alboteanu, S. Stepan, "An algorithm for the adaptive control of anti hail missile launch launch pads," IASI POLYTECHNIC INSTITUTE BULLETIN Published by "Gheorghe Asachi" Technical University of Iaşi Vol 64, Nr .2, year 2018 Section ELECTROTECHNICS. ENERGETICS. ELECTRONICS , ISSN 1223-8139, <http://www.bulipi-eee.tuiasi.ro>
- [4] G. Manolea, S. Ivanov, L.I. Alboteanu, C. Şulea, Ş.M. Nicolae "Design and Control of the Electric Drive of the Anti- Hail Launching System," Annals of the University Eftimie Murgu, Resita,2014
- [5] EMERSON Industrial Automation, *AC variable speed drive for servo motors, user guide* <http://www.acontrol.com.pl/uploads/pdf/instrukcje/Digitax-ST-user-guide-ENG.pdf>

Modeling of Thermal Comfort Parameters in Residential Buildings

Radu-Cristian Dinu*, Daniela Popescu*, Ioana-Gabriela Sîrbu*, Dan Gabriel Stănescu*

* University of Craiova / Faculty of Electrical Engineering, Craiova, Romania, e-mail: rcdinu@elth.ucv.ro

Abstract – At the level of residential buildings, current studies and research are focused on issues that have as a main priority, the energy of buildings. Energy efficiency of buildings involves, in addition to technical regulations and energy rehabilitation works, an economic optimization of energy in buildings. This optimization must not be done at random, but we must ensure that the conditions of thermal comfort inside the building are met at all times. In this paper, the object of the study is a room located in the middle of a condominium building in Craiova. The building of which the studied room is part is located inside the locality and has constructive structure of the tire elements, characterized by specific thermal resistances of the construction materials used. The mathematical model involves determining the values of thermal comfort parameters (indoor temperature, average radiation temperature, etc.) and their implementation in the calculation of the thermal comfort index, B. The results obtained for the three categories of rooms, allow the feeling of comfort to be included in one of the seven levels. Between the three types of studied rooms there are differences of the calculated interior temperatures, due to the temperature differences on the faces of the construction elements.

Cuvinte cheie: *clădire, camera, confort termic, indice de confort, temperatură interioară.*

Keywords: *building, room, thermal comfort, comfort index, indoor temperature.*

I. INTRODUCTION

The concept of energy is closely related to the building and the system of installations related to the building, the energy saving problems implicitly referring to the latter category. The building is a set of spaces delimited by a series of surfaces that make up the building envelope and through which heat loss occurs. The envelope of a building separates the heated volume of a building from the outside air, floor, adjoining rooms not heated or much less heated, delimited by the volume of the building through walls and / or floors, properly insulated, and other buildings with adjacent walls, delimited by the building considered by joints [1].

For condominium buildings (residential blocks), the supervision and management of the endowment facilities is a necessary and complex problem. By using energy management systems, buildings become safer, consume less energy, ensure better operation of facilities and have a high level of comfort [2].

An efficient method of reducing the consumption of thermal energy for heating, and therefore of heating costs, is the intermittent operation of the set of heating installations (source - distribution network - heating

elements). Through the intermittent (discontinuous) operation of the heating system, in addition to the benefits obtained from the source of thermal energy production (reduction of primary energy consumption and impact on the environment) there are a number of disadvantages regarding the degree of satisfaction of thermal comfort [1], [3].

The interruption of thermal agent supply leads to the decrease, in time, of the air temperature inside a room (of an enclosed space) which has the effect of worsening the thermal comfort index [3].

II. GENERAL PRESENTATION OF THE PROBLEM

As most people spend (80 ... 90)% of their lives in buildings, enclosed spaces must ensure: the possibility of performing both physical and intellectual work with maximum efficiency and the possibility of performing recreational, rest and sleep activities in optimal conditions [4], [5]. Achieving these conditions depends on many factors, which influence the feeling of comfort, work capacity and human regeneration.

The design of enclosed spaces taking into account these conditions is a complex issue that must take into account the current trends of rationalization of energy consumption, which decisively influence the optimal or allowed values of comfort parameters [4]. In most cases these influences have negative effects because this criterion leads to inadequate values in terms of comfort.

The notion of technical comfort includes all the parameters achieved and controlled with installations, which directly influence a person's mood and act on his senses. It includes thermal, acoustic, olfactory and visual comfort. Corresponding to the following percentages of dissatisfaction with the comfort provided: 10%, 20%, 30%, enclosed spaces are classified into three categories: A, B and C [1], [3], [5].

The perception and appreciation of the basic elements of comfort a person is influenced by some psychological factors, but at the same time the evolution and psychological balance of man are closely related to the environment. So there is a mutual relationship between psychological and technical comfort. However, the human psyche also depends on independent factors such as age, sex, etc., which also influence the assessment of the level of technical comfort. Thus, the sensation of pleasure may appear as the optimal result of the parameters of technical and psychological comfort (Fig. 1).

Comfort is the subjective sensation that occurs in the human body based on the complex action of physical and mental parameters. The subjective comfort of people in an enclosed space depends on many factors, which can be

grouped, according to G. Blanchere, as follows: temperature, humidity and air circulation; smell and breath, touch and touch, acoustic factors; sight and color effects; vibrations and movements of the building, special factors (solar inputs, ionisation); safety factors; factors related to the daily schedule; unforeseen dangers; economic factors [4].

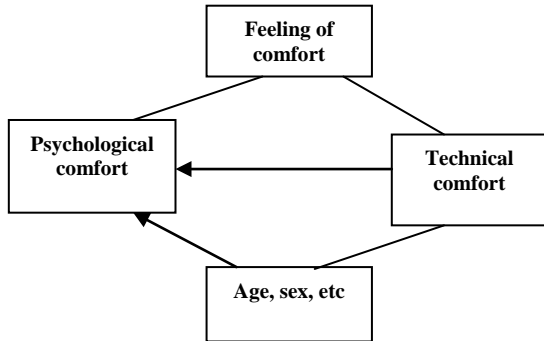


Fig.1. Getting the feeling of comfort [4]

By listing the comfort factors we can see a group related to the thermal environment, called thermal comfort factors. The appearance of the subjective sensation of thermal comfort is decisively determined by the following parameters: indoor air temperature, t_i [°C], average radiation temperature of the delimiting surfaces, θ_{mr} [°C], relative humidity of the indoor air, φ_i [%] and the partial pressure of water vapors in the air, p_s [bar], the speed of the indoor air, v_i , [m/s], the heat production of the human body (labor intensity), i_M [met], the heat released, thermoregulation, thermal resistance of clothing and its influence on evaporation, R_{clo} [clo] [4].

The first four are physical parameters, and the other two are related to the human body's ability to adjust in order to maintain thermal balance. The basic factors that influence the thermal balance of the human body are: the heat produced by the body, which depends primarily on the level of activity, but is also influenced by age, sex, etc. respectively, the heat given off by the body, which depends on the clothing, but also on the other parameters listed above [5], [6].

The sensation of thermal comfort is defined as that conscious state that expresses satisfaction with the thermal environment and whose evaluation is performed using the subjective seven-level comfort scale (relation 1): +3 (very warm); +2 (hot); +1 (slightly warm); 0 (neutral); -1 (coolness); -2 (cold); -3 (cold) [4], [6], [7]:

$$B = C + 0,25 \cdot (t_i + \theta_{mr}) + 0,1 \cdot x - 0,1 \cdot (37,8 - t_i) \cdot \sqrt{v_i} \quad (1)$$

where C is a constant that has the value -9.2 in the cold period and -10.6 in the hot period and x is the absolute humidity of the air inside the room, [$\text{g}_{\text{apă}}/\text{kg}_{\text{aer}}$] [7].

The average radiation temperature, θ_{mr} represents the weighted average temperature of the delimiting surfaces (horizontal and vertical walls, doors, windows, heating elements) of the studied room. From a mathematical point of view, the average radiation temperature represents a weighted average of the products of the specific surfaces S_j [m^2] and their specific

temperatures, θ_j [°C], being in fact a result of the radiation effect on a body inside the room, on hot surfaces (heating bodies) and cold surfaces (relation 2) [8]:

$$\theta_{mr} = \frac{\sum_{j=1}^n S_j \cdot \theta_j}{\sum_{j=1}^n S_j} \quad (2)$$

The average temperature of the interior surfaces of the construction elements (their specific temperatures) is determined by the relation 3 [5]:

$$\theta_j = t_i - R_i \cdot \frac{t_i - t_e}{R_j} \quad (3)$$

where R_i is the thermal resistance at the surface of the construction elements, [$\text{m}^2\text{K}/\text{W}$], t_e is the temperature of the air outside the considered space, [°C] and is the corrected thermal resistance of the construction elements delimiting the examined space, [$\text{m}^2\text{K}/\text{W}$]. The value of the thermal resistance at the surface of the construction elements R_i , is considered $0,125 \text{ m}^2\text{K}/\text{W}$ for all categories of vertical construction elements and respective ceilings, $0,172 \text{ m}^2\text{K}/\text{W}$ for floors [5], [7].

Highlighting the thermal comfort in an enclosed space (room) involves, in addition to establishing the thermal comfort index, the determination of groups of comfort indexes established in the order of their evolutions, as follows [4]: thermal stress evaluation indexes under extreme environmental conditions, which include the effect of several environmental parameters and the discomfort of ICA airflow.

A. Thermal stress assessment indexes in extreme environmental conditions.

With the help of thermal stress evaluation indexes, the safety limits and the tolerance time for industries where the activity takes place in environments with high temperatures can be established. This category includes: P4SR index (McArdl); ITS thermal stress index; physiological effect index (Robinson); thermal acceptability ratio (lonodes); the WBGT index (Yaglou and Missenard); the nomograms of Vogt and Metz etc.

The thermal stress index is standardized internationally by ISO-7243, coded WBGT (Wet Bulb Globe Temperature - wet bulb temperature of a special construction thermometer) and defined using relation 4 [9]:

$$WBGT = 0,7 \cdot t_u + 0,2 \cdot t_g + 0,1 \cdot t_{as} \quad (4)$$

where t_u is the temperature of the wet thermometer, [°C], t_g is the temperature of the black globe, [°C] and t_{as} is the temperature of the air under solar thermal charge, [°C].

B. Indexes that include the effect of several parameters of the environment.

1. **The effective temperature**, established by Yaglou, is defined as the index that includes the effect of the temperature measured with the dry bulb thermometer, humidity and air movement in a single value and which

produces the sensation of heat or cold felt by the human body. For low air currents ($v_i < 0,15$ m/s) the effective temperature is calculated with the relation (McIntyre) [6]:

$$t_E = 0,492 \cdot t_i + 0,19 \cdot p_s + 6,47, \quad (5)$$

2. **The resulting temperature**, established by Missenard, represents the temperature of an uniform environment, with calm air in which the air temperature is equal to the average radiation temperature and which produces a sensation equivalent to the existing environment (rel. 6) [7]. The resulting dry temperature is less sensitive to the radiation temperature and does not consider the humidity:

$$t_R = \frac{\theta_{mr} + 3,17 \cdot t_i \cdot \sqrt{v_i}}{1 + 3,17 \cdot v_i}, \quad (6)$$

3. **The equivalent temperature** is defined as the air temperature in a room in which $v_i = 0$ and $t_i = \theta_{mr}$ and where a black cylinder 558 mm high and 390 mm wide loses the same quantity of heat as in the surrounding environment. The surface of the cylinder is maintained at a temperature equal to the temperature of the human body by recording and compensating the energy consumed during the heat exchange with the environment [2]. This index of thermal comfort indoors can be determined by the relationship [6]:

$$t_{ech} = 0,522 \cdot t_i + 0,478 \cdot \theta_{mr} - 0,21 \cdot (37,8 - t_i) \cdot \sqrt{v_i}, \quad (7)$$

C. ICA airflow discomfort

According to Mayer and Fanger, the discomfort of the air current, ICA, can be determined according to the degree of turbulence of the indoor air, T_u [%], the speed of movement of the indoor air, v_i [m/s] and the temperature of indoor air, t_i [°C], according to relation [4]:

$$ICA = (34 - t_i) \cdot (v_i - 0,05)^{0,62} \cdot (0,37 \cdot T_u \cdot v_i + 3,14) [\%] \quad (8)$$

III. RESULTS

The applicative part of this article consists in determining the thermal comfort indicators for a room located in a residential building, in the middle (a single exterior wall - Fig. 2), based on mathematical calculation models.

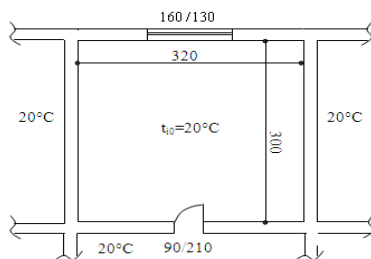


Fig. 2. Constructive Dimensions and parameters measured for the studied room.

The studied room is of the living room type, with a height of 2.5 m, and the air temperature inside the room, to satisfy the conditions of thermal comfort, being $t_i = +20^\circ\text{C}$. The absolute air humidity for this category of rooms is $x_i = 7$ kg_{water}/kg_{air}, the air speed inside the room is 0.15 m/s and the air turbulence coefficient $T_u = 40\%$ [9]. The room is heated by a radiator type heater with 10 elements KALOR 600/160 series, with a thermal power of 136.7 W/ element, each element having a heating surface of 0 de 0,306 m², the heating agent being hot water with a temperature of 65/45°C.

The room is part of a building located inside the Municipality of Craiova, included in the second climatic zone, for which the average external temperature of calculation is considered to be $\theta_e = -15^\circ\text{C}$.

The corrected thermal resistances of the perimeter construction elements were established according to the constructive structure of each type of element and the thermal characteristics of the constructive materials, resulting: exterior walls (PE), $R_{PE} = 0,255$ m²K/W; interior walls (PI), $R_{PI} = 0,393$ m²K/W; ceiling (Tv), $R_{TV} = 0,433$ m²K/W; terraces over the top floor (Tr), $R_{Tr} = 0,269$ m²K/W; floor (Pd) $R_{Pd} = 0,433$ m²K/W; exterior window (FE), $R_{FE} = 0,390$ m²K/W; interior door (UI), $R_{UI} = 0,348$ m²K/W [10].

The heat supply regime is intermittent, a regime that implies that both during the night and during the day, the supply of the heating agent will turned off [11]. During the day, we will consider an interruption of the heat supply for 7 hours. During the interruption of the heat supply, the outside air temperature is considered to remain constant ($\theta_e = -15^\circ\text{C}$ - Table I).

TABLE I.
INDOOR AIR TEMPERATURE VARIATION WHEN INTERRUPTING THERMAL ENERGY SUPPLY [9]

hour	Indoor air temperature, [°C] (Measured values)		
	Ground floor	Intermediate floor	Top floor
0	20	20	20
1	19,796	19,798	19,781
2	19,694	19,698	19,672
3	19,593	19,598	19,563
4	19,492	19,498	19,455
5	19,391	19,398	19,347
6	19,291	19,299	19,239

Based on the mathematical models presented in the second part of the article (rel. 1-8), for the studied room, located at different levels, different values are obtained for the specific temperatures on the inner faces of the perimeter construction elements (table II for the located room on the ground floor, tab. III for the room located on the intermediate floor and tab. IV for the room located on the top floor), and different values of the thermal comfort index.

The hourly variation of the thermal comfort indicators is presented in figures 3 - 5, highlighting the variation curves for the thermal comfort index (Fig. 3), of the effective temperature (Fig. 4) and of the air current discomfort (Fig. 5).

TABLE II VARIATION OF THERMAL COMFORT INDICES INSIDE THE ROOMS LOCATED ON THE GROUND FLOOR, WHEN NO HEAT IS SUPPLIED

Parameter/ symbol/U.M.	Heat supply shutdown time, [h]						
	0	1	2	3	4	5	6
	Variation of indoor air temperature as a function of the heat supply shutdown time, [°C]						
	20	19,796	19,694	19,593	19,492	19,391	19,291
Temperature on the inside of the FE, θ_{FE} , [°C] (rel. 3)	8,78	8,64	8,57	8,51	8,44	8,37	8,30
Temperature on the inside of the PE, θ_{PE} , [°C] (rel.3)	2,82	2,72	2,67	2,62	2,57	2,51	2,46
Temperature on the inner faces of the interior construction elements, [°C] (rel. 3)	20	19,796	19,694	19,593	19,492	19,391	19,291
The temperature on the inside of the floor, θ_{Pd} , [°C] (rel. 3)	17,18	17,05	16,98	16,92	16,85	16,79	16,72
Temperature on the inside of the ceiling, θ_{Tv} , [°C] (rel. 3)	20	19,855	19,782	19,710	19,638	19,567	19,495
Temperature on the heater θ_{Ci} , [°C]	55	19,796	19,694	19,593	19,492	19,391	19,291
Average radiation temperature, θ_{mr} , [°C] (rel. 2)	19,16	16,98	16,89	16,81	16,73	16,65	16,57
Thermal comfort index, B (rel. 1)	0,60	0,00	-0,05	-0,10	-0,15	-0,20	-0,25
The sensation felt	Neutral/slightly warm	neutral	neutral	neutral	neutral	neutral	neutral
Equivalent temperature, t_{ech} , [°C] (rel. 7)	18,15	16,98	16,88	16,78	16,68	16,58	16,48
The resulting temperature, t_R , [°C] (rel. 6)	29,62	27,98	27,84	27,70	27,56	27,42	27,28
Effective temperature, t_E , [°C] (rel. 5)	16,31	16,21	16,16	16,11	16,06	16,01	15,96
The discomfort of the air current, ICA, [%] (rel. 8)	10,62	10,77	10,85	10,93	11,01	11,08	11,16

TABLE III VARIATION OF THERMAL COMFORT INDICES INSIDE THE ROOMS LOCATED ON THE INTERMEDIATE FLOOR, WHEN NO HEAT IS SUPPLIED

Parameter/ symbol/U.M.	Heat supply shutdown time, [h]						
	0	1	2	3	4	5	6
	Variation of indoor air temperature as a function of the heat supply shutdown time, [°C]						
	20	19,798	19,698	19,598	19,498	19,398	19,299
Temperature on the inside of the FE, θ_{FE} , [°C] (rel. 3)	8,78	8,64	8,58	8,51	8,44	8,37	8,31
Temperature on the inside of the PE, θ_{PE} , [°C] (rel. 3)	2,82	2,72	2,67	2,62	2,57	2,52	2,47
Temperature on the inner faces of the interior construction elements, [°C] (rel. 3)	20	19,798	19,698	19,598	19,498	19,398	19,299
The temperature on the inside of the floor, θ_{Pd} , [°C] (rel. 3)	20	19,869	19,804	19,740	19,675	19,610	19,546
Temperature on the inside of the ceiling, θ_{Tv} , [°C] (rel. 3)	20	19,850	19,775	19,701	19,627	19,552	19,478
Temperature on the heater θ_{Ci} , [°C]	55	19,798	19,698	19,598	19,498	19,398	19,299
Average radiation temperature, θ_{mr} , [°C] (rel. 2)	19,99	19,80	19,71	19,61	19,52	19,43	19,34
Thermal comfort index, B (rel. 1)	0,81	0,70	0,65	0,60	0,55	0,49	0,44
The sensation felt	slightly warm	slightly warm	Slightly warm	neutral/slightly warm	neutral/slightly warm	neutral	neutral
Equivalent temperature, t_{ech} , [°C] (rel. 7)	18,55	18,34	18,23	18,13	18,02	17,92	17,81
The resulting temperature, t_R , [°C] (rel. 6)	30,19	29,89	29,75	29,60	29,45	29,31	29,16
Effective temperature, t_E , [°C] (rel. 5)	16,31	16,21	16,16	16,11	16,06	16,02	15,97
The discomfort of the air current, ICA, [%] (rel. 8)	10,62	10,77	10,85	10,92	11,00	11,08	11,15

TABLE IV VARIATION OF THERMAL COMFORT INDICES INSIDE THE ROOMS LOCATED ON THE TOP FLOOR, WHEN NO HEAT IS SUPPLIED

Parameter/ symbol/U.M.	Heat supply shutdown time, [h]						
	0	1	2	3	4	5	6
	Variation of indoor air temperature as a function of the heat supply shutdown time, [°C]						
	20	19,781	19,672	19,563	19,455	19,347	19,239
Temperature on the inside of the FE, θ_{FE} , [°C] (rel. 3)	8,78	8,63	8,56	8,49	8,41	8,34	8,26
Temperature on the inside of the PE, θ_{PE} , [°C] (rel. 3)	2,82	2,71	2,66	2,60	2,55	2,49	2,44
Temperature on the inner faces of the interior construction elements, [°C] (rel. 3)	20	19,781	19,672	19,563	19,455	19,347	19,239
The temperature on the inside of the floor, θ_{Pd} , [°C] (rel. 3)	20	19,86	19,79	19,72	19,65	19,58	19,51

Parameter/ symbol/U.M.	Heat supply shutdown time, [h]						
	0	1	2	3	4	5	6
	Variation of indoor air temperature as a function of the heat supply shutdown time, [°C]						
Temperature on the inside of the ceiling, θ_{TV} , [°C] (rel. 3)	9,907	9,751	9,674	9,596	9,519	9,442	9,366
Temperature on the heater θ_{Ci} , [°C]	55	19,781	19,672	19,563	19,455	19,347	19,239
Average radiation temperature, θ_{mr} , [°C] (rel. 2)	17,84	15,65	15,57	15,48	15,39	15,30	15,21
Thermal comfort index, B (rel. 1)	0,27	-0,34	-0,39	-0,45	-0,50	-0,55	-0,61
The sensation felt	neutral	neutral	neutral	neutral	neutral/ cool	neutral/ cool	neutral/cool
Equivalent temperature, t_{ech} , [°C] (rel. 7)	17,52	16,34	16,23	16,13	16,02	15,91	15,80
The resulting temperature, t_R , [°C] (rel. 6)	28,74	27,07	26,92	26,77	26,62	26,47	26,32
Effective temperature, t_E , [°C] (rel. 5)	16,31	16,20	16,15	16,10	16,04	15,99	15,94
The discomfort of the air current, ICA, [%] (rel. 8)	10,62	10,79	10,87	10,95	11,03	11,12	11,20

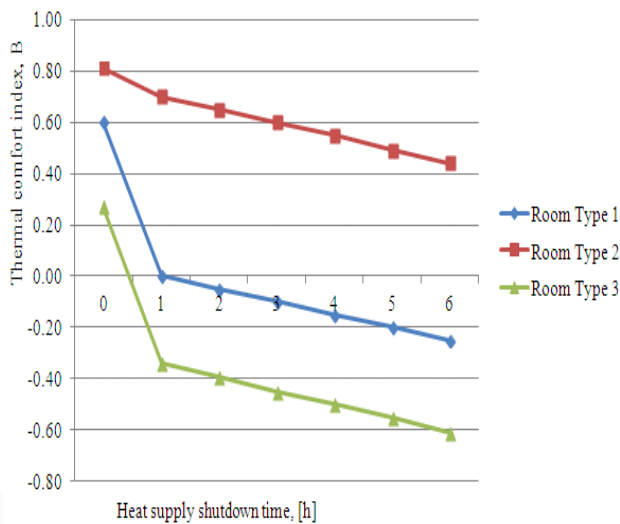


Fig. 3. Hourly variation of the thermal comfort index, B, during the interval of interruption of the heat supply, depending on the type of room, at outside temperature of -15°C: type 1 - room located on the ground floor; type 2 - room located on the intermediate floor; type 3 - room located on the top floor.

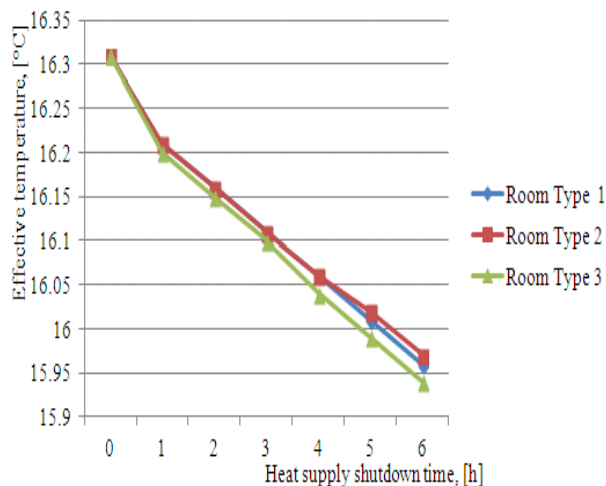


Fig. 4. Hourly variation of the effective temperature, t_{ef} , during the interval of interruption of the heat supply, depending on the type of room: type 1 - room located on the ground floor; type 2 - room located on the intermediate floor; type 3 - room located on the top floor.

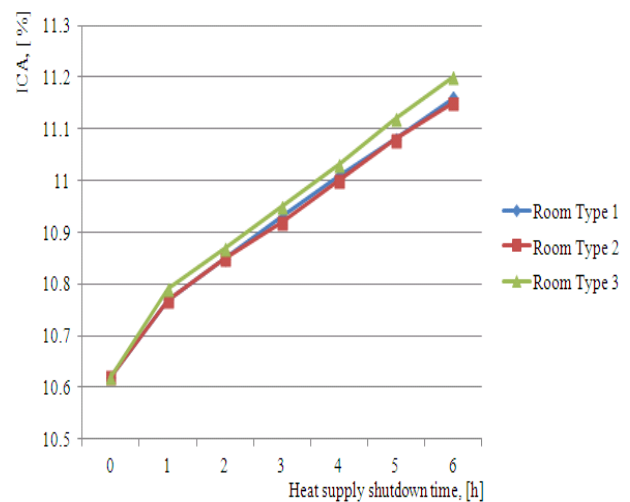


Fig. 5. Hourly variation of the air current discomfort, ICA, during the heat supply interruption interval, depending on the type of room: type 1 - room located on the ground floor; type 2 - room located on the intermediate floor; type 3 - room located on the top floor.

IV. CONCLUSION

The intermittent (discontinuous) operation of heat supply systems has the main advantage of the reduction of thermal energy consumption for heating. It should be noted that, at low outdoor temperatures and for long intervals of interruption of the thermal agent supply, the thermal comfort indicators that define the climate inside an enclosure, can undergo important changes. Thus, situations may arise in which the level of thermal comfort inside the heated rooms no longer satisfies the requirements of the occupants or of a certain number of people.

An important aspect that should be emphasized is that the intermittent operating regime of heating installations is not imposed by the manufacturer / distributor of the heating agent, but by the final consumers, regardless of their nature, in order to reduce maintenance costs as much as possible.

In the case study it is observed that:

1. The thermal comfort index, B, after 6 hours of interruption of the thermal agent supply for heating varies much more emphatic, shifting from a positive value (0.81)

to a negative value (-0.61), which means a transition from an occupant-like sensation of neutral to slightly warm to a sensation of neutral to cool (fig. 3).

2. In the case of type 1 and type 3 rooms, after the first hour of interruption of the thermal agent supply the thermal comfort index, B, worsens sharply, decreasing from 0.60 to 0 in the case of type 1 and type 0 rooms, from 0.27 to -0.34 in the case of type 3 rooms (fig.3).

3. The effective temperature, meaning the temperature felt by the human body and which produces the sensation of cold or heat, varies very little depending on the type of room, and during the interval of 6 hours of interruption of the thermal agent supply, this variation is between 16,31°C and 15,94°C.

4. The actual temperature varies mainly depending on the number of exterior construction elements. It is observed that in the case of the type 3 room, regardless of the value of the outside temperature, the actual temperature has a different variation from the other room types (fig.4), which is explained by the fact that in the case of this type of room the number of exterior construction elements is three, not two, as in the case of type 1 and 2 rooms.

5. Regarding the discomfort of the air current, it has values higher than 5% (fig. 5) which means that, from the point of view of this indicator, the climatic conditions inside the studied room do not satisfy the thermal comfort of the occupants. By analyzing the diagram it is observed that in the case of rooms type 1 and type 2, characterized by the same number of construction elements outside (two elements) discomfort of the air flow is identical for every interruption time of the heat supply (blue curve overlaps the red one) with slight deviations after the 2 hour interval of power supply interruption. In the case of the type 3 room, the variation of the air current discomfort is different in comparison with the first two types of rooms, due to the higher number of external construction elements.

6. In the case of other categories of rooms (bathrooms, kitchens, etc.) the value of the absolute humidity of the air is higher, so that the thermal comfort indices will have different variations compared to the case of the living rooms studied in this paper. Also, major differences in the variation of thermal comfort indexes occur if the construction structure of the exterior and interior construction elements is greatly modified.

Source of research funding in this article: Research program of the Electrical Engineering Department financed by the University of Craiova.

Contribution of authors:

First author – 50%;

First co-author – 20%;

Second co-author – 15%;

Third co-author – 15%

Received on July 07, 2020

Editorial Approval on November 20, 2020

REFERENCES

- [1] Cocora, O., *Auditul și expertiza termică a clădirilor și instalațiilor aferente*, Editura MatrixRom, București, 2004.
- [2] Sârbu, I., Kalmár, F., *Optimizarea energetică a clădirilor*, Editura Matrix Rom, București, 2002.
- [3] Iliina, M., ș.a., *Enciclopedia tehnică de instalații. Manualul de Instalații – Încălzire*. Ediția a II - a, Asociația Inginerilor de Instalații, Editura ARTECNO, București, 2010.
- [4] Dinu, R., C., *Instalații în construcții – Note de curs*, www.retele.elth.ucv.ro/Dinu Radu Cristian/Instalații în construcții.
- [5] Mircea I., Dinu R.C., *Producerea energiei electrice și termice, partea a-II-a*, Editura Universitaria, 2006.
- [6] Sârbu, I., Kalmár, F., Cincă, M., *Instalații termice interioare. Optimizare și modernizare energetică*, Editura Politehnica, Timișoara, 2007.
- [7] Iliina, M., Lungu, C., *100 de probleme practice de instalații de încălzire*, Editura MatrixRom, București, 2005.
- [8] Dinu R. C., Mircea I., Ruieneanu L., Popescu N., "The Evaluation of Thermal Comfort Indices in Households", Journal of Sustainable Energy, Volume 3, no. 3, 2011
- [9] Mircea, P.M., Dinu, R.C., Popescu, N., Buzatu, G., „Monitoring and analysis of thermal comfort parameters in a living room of a building”, Journal of Sustainable Energy, Volume 5, no. 1, 2014, cotat BDI, ISSN 2067 – 5534.
- [10] N.-M., Rădulescu - Brănișteanu, Influența funcționării intermitente a sistemelor de încălzire asupra temperaturii interioare, Craiova: Sesiunea Națională a Cercurilor Științifice Studentești, ELSSES – 2020, 10.07.2002.
- [11] Bánhidí, L., Zöld, A., Kalmár, F., Csoknyai, T., *Influența variației dinamice a temperaturii interioare asupra confortului termic*, Conferința “Instalațiile pentru Construcții și Confortul Ambiental”, Timișoara, 2000.

Studies on the Command of Single-Phase Rectifiers Using the Scalar Control Technique

Florin Alexandru Teodorescu

University of Craiova, Faculty of Electrical Engineering, Craiova, Romania, ax.teodorescu@gmail.com

Abstract - One of the important problems of power supply systems consists in ensuring the quality of energy supplied to consumers. In this issue, the reduction of the harmonic spectrum of the supplied voltage and current has a key role. As electronic power converters are now increasingly used by consumers, the problem of reducing the harmonic spectrum of the current absorbed by the power supply by these consumers is becoming more and more pronounced. For this, there is the problem of using consumers with a power factor as close as possible to the unit, which also ensures the increase of the efficiency of these consumers. The present paper focuses on the study of single-phase rectifier configurations provided with power factor control (PFC) structures. Among the multiple techniques and methods of power factor control, the scalar power factor control technique was applied to a boost type power converter, in two variants. The first variant is that of a single-phase rectifier in fully controlled bridge. The second is that of a single-phase rectifier in uncontrolled bridge. In both cases, the study of the scalar PFC technique was based on the Matlab/Simulink modeling of the two mentioned configurations. Achieving these models allowed the study of the correction mechanism of the power factor under the influence of the various functional parameters of the approached configurations.

Cuvinte cheie: factor de putere, redresor, convertor static ridicător, control scalar, model Matlab-Simulink.

Keywords: power factor, rectifier, boost convertor, scalar control technique, Matlab/Simulink model.

I. INTRODUCTION

AC-DC, DC-DC or DC-AC power converters are widely used because they provide a variable level voltage at the output, a high efficiency and, in the case of DC - AC converters, a variable output voltage and frequency separately or simultaneously. An important drawback, which is characteristic of these converters connected to the alternating current network, is that they absorb from the power supply a current in the form of pulses on each alternation. Therefore, these converters have a high total harmonic distortion factor (*THD*) and a low power factor.

Typically, these converters are used in various configurations of electronic systems, having the role of controlling the output voltage even under conditions of varying load current and input voltage. More and more applications require the reduction of the *THD* factor of the current consumed from the power supply and a power factor as high as possible. The requirements imposed by ensuring a good power quality, led to sustained researches for the development of some converter structures with power factor control circuits [1]-[8].

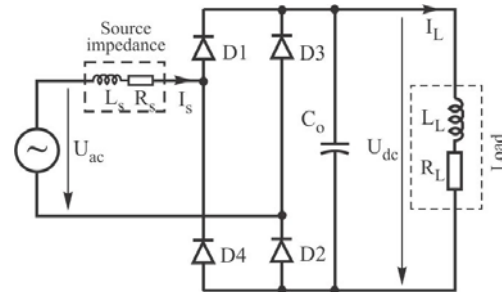


Fig. 1. Schematic of a single-phase uncontrolled bridge rectifier.

The current absorbed by most electronic equipment is non-sinusoidal, discontinuous, with appreciable peaks. This current has a rich content of harmonics, which flows through the mains and the equipment that produced it. Fig. 1 illustrates the diagram of a single-phase uncontrolled bridge rectifier, with filtering capacitor on the DC side, which is suggestive in support of the previous statement.

The configuration illustrated in Fig. 1 was modeled and simulated in Matlab / Simulink. The harmonics contained in the spectrum of the current absorbed from the network circulate both through the rectifier and through the power supply to which the rectifier is connected. The shape of the current absorbed from the power supply, together with that of the supply voltage, are shown in Fig. 2.

The waveforms illustrated in Fig. 2 correspond to the following circuit parameters: $U_{ac} = 100$ V (RMS), $R_s = 0.01 \Omega$, $L_s = 1 \cdot 10^{-6}$ H, $C_o = 1000 \cdot 10^{-6}$ [F], $R_L = 50 \Omega$, $L_L = 1 \cdot 10^{-4}$ [H], $U_{dc} = 131.2$ V.

By Matlab / Simulink modeling of the Fig. 1 circuit, it was possible to graphically represent the harmonic spectrum and determine the *THD* factor for the current absorbed from the power supply.

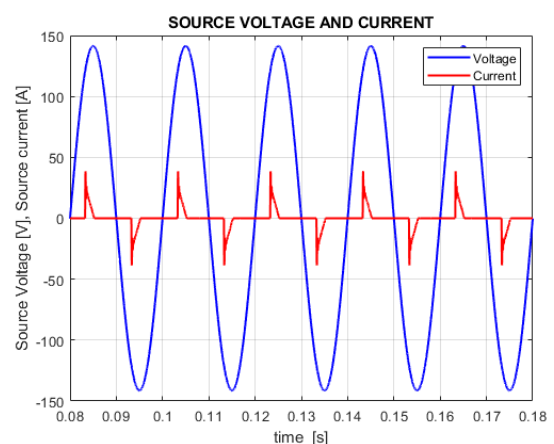


Fig. 2. The evolution in time of the power supply voltage and the current absorbed from the power supply by an uncontrolled bridge rectifier.

Fig. 3 shows the spectrum of harmonics determined by simulating the operation of the single-phase uncontrolled bridge rectifier.

Following the simulations, the parameters were also determined: the fundamental amplitude of the supply current $A_I = 9.2$ A, $THD = 1.614$ and the power factor $PF = 0.445$.

From the above, it can be concluded that a conventional single-phase full-wave rectifier (uncontrolled) which is provided with filtering capacitor at the output has the following characteristics:

- The absorbed current is non-sinusoidal (Fig. 2), with a rich content of harmonics, especially in the field of harmonics with a rank close to fundamental: 3, 5, 7, 9, as illustrated in Fig. 3.
- It has a low power factor, which reduces the rectifier efficiency.
- The presence of harmonics increases the operating temperature of the transmission lines and other equipment connected to the mains (power supply).
- Reduces the capacity of the power supply to provide maximum power to the load [4].

II. SCALAR CONTROL TECHNIQUE

Due to the previously mentioned disadvantages, Power Factor Correction (PFC) techniques have been developed, with the role of bringing this important parameter for consumers and power networks to values as close as possible to the unit.

PFC rectifiers have been developed in two basic configurations [2], [8]:

1. Using a fully controlled rectification stage, in which each semiconductor device is controlled according to an algorithm established by a certain power factor control technique.
2. Using an uncontrolled rectifier stage, followed by a controlled buck / boost configuration, in which case the control algorithm applies only to the power contactor belonging to the configuration following the uncontrolled rectifier.

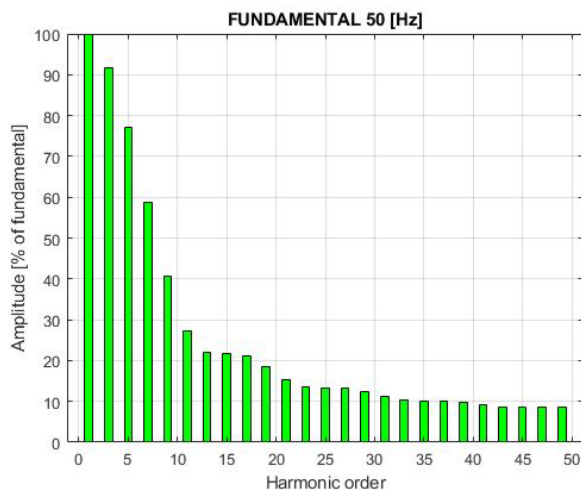


Fig. 3. The harmonic spectrum of the current absorbed from the power supply by a single-phase uncontrolled bridge rectifier.

The first configuration requires the switching operation of a number of four semiconductor devices, while the second configuration requires the switching operation of a single semiconductor device. The choice of one of the two solutions is made primarily based on the converter efficiency at the required power and the characteristics of the semiconductor devices at the required switching frequency.

The scalar control technique can be applied to both variants of PFC rectifiers. The principle diagram of a PFC rectifier from the first category is shown in Fig. 4 [2]. Examining the scheme in Fig. 4 it can be stated that, in the situation where in the analysis of the circuit, it is taken into account own inductance of the power supply L_s , the circuit works as a direct boost converter [2].

In Fig. 5 shows the configuration of a PFC boost converter, with scalar control according to the average current value [8].

III. MODELING THE SINGLE PHASE RECTIFIER WITH PFC SYSTEM

The diagram of the single-phase PFC rectifier with controlled rectification stage to be modeled is shown in Fig. 4. As it can be seen, there are two cascading feedback loops. The external loop (after the output voltage) provides the value of the reference current I_{ref} for the internal feedback loop (according to the current absorbed from the power supply). In steady state, the reference current is a constant quantity.

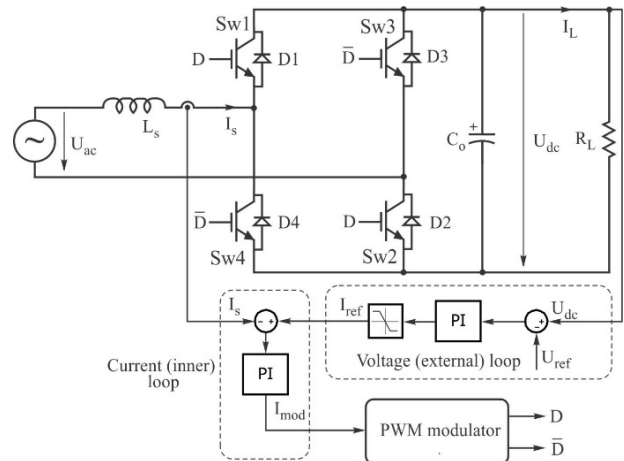


Fig. 4. Configuration of a single-phase rectifier with power factor correction by scalar control technique, with fully controlled bridge [2].

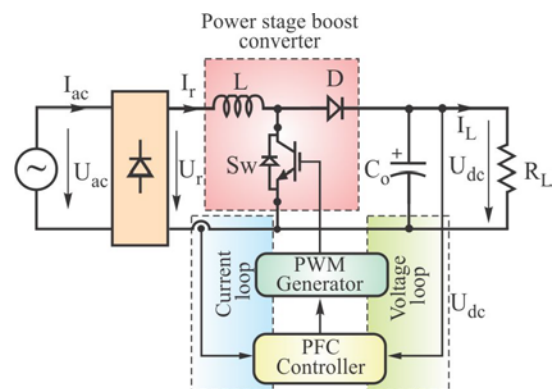


Fig. 5. The principle of PFC control of the boost converter.

In the second feedback loop, the input current is compared with the reference current in order to obtain the modulating current I_{mod} .

The PWM modulator contains a triangular wave generator. Switching moments occur by comparing the triangular wave with the modulating current, as it can be seen in Fig. 6. The principle of generating PWM control signals is similar to the SPWM technique used to control voltage-frequency static converters that drive asynchronous motors in variable speed drive schemes.

The circuit configuration shown in Fig. 4, was modeled in the Matlab / Simulink environment, in order to study the possibilities of improving the power factor and determining the amplitude of the fundamental as well as the THD factor.

The achieved model is shown in Fig. 7.

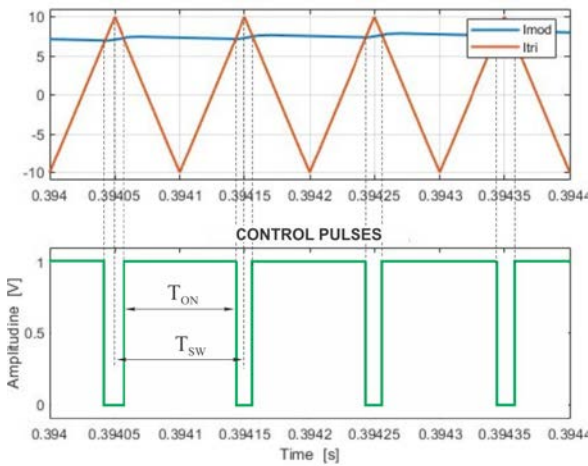


Fig. 6. Control pulses generation (operating cycle).

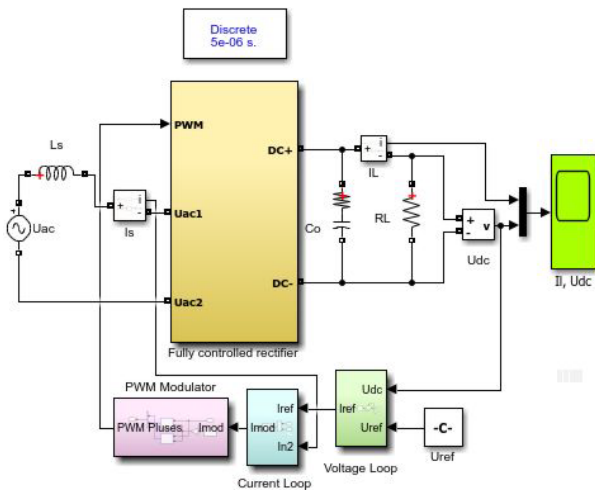


Fig. 7. The rectifier model of the scheme in Fig. 4.

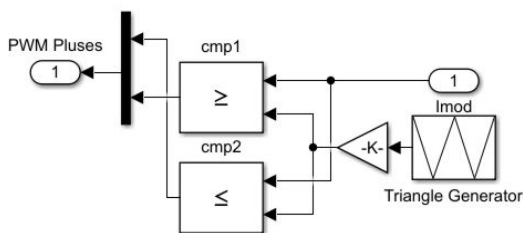


Fig. 8. PWM modulator structure.

The fully controlled single-phase rectifier was implemented with IGBT transistors. This solution was preferred because the switching frequency is not very high, in which case the use of MOSFET transistors would have been recommended. In Fig. 8, the structure of the PWM modulator block is shown. The structure contains a triangular wave generator and two comparators that have the role of detecting the moments of intersection between the modulating current and the triangular wave (according to Fig. 6), thus generating PWM control pulses for IGBT transistors in the rectifier bridge.

The evolution in time of the current absorbed from the power supply, together with the supply voltage, is shown in Fig. 9. The waveforms in Fig. 9 were obtained with the following circuit parameters: $U_{ac} = 100$ V peak value, $U_{ref} = 120$ V, $R_L = 45\Omega$, the frequency of the triangular carrier wave $f_{tr} = 10^4$ Hz. The harmonic content of the absorbed current is shown in Fig. 10.

1. Harmonics close to the fundamental (low frequency), have amplitudes related to the fundamental, extremely small (less than 2%), as illustrated in Fig. 10. The harmonic of rank 200, corresponding to the carrier frequency of the triangular generator (10 kHz), has a relative to fundamental amplitude of about 3%, as can be seen from Fig. 11, in which the relative to fundamental amplitude of the first 210 harmonics were represented.

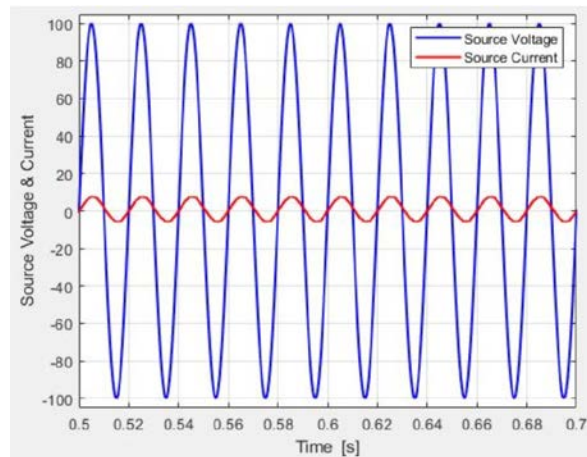


Fig. 9. The evolution in time of the current absorbed from the power supply together with the supply voltage after compensation.

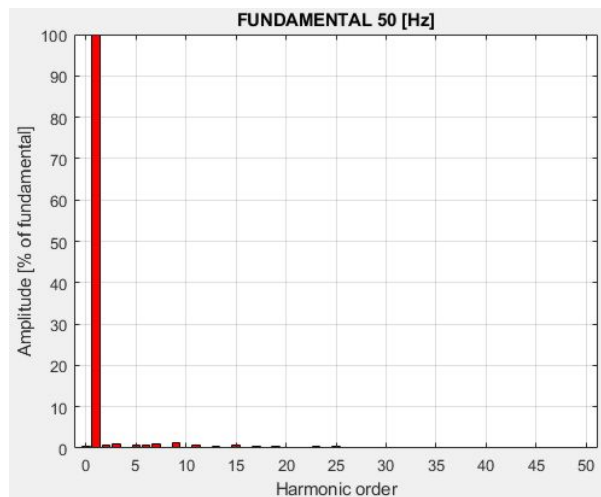


Fig. 10. Harmonic spectrum of the current absorbed from the power supply after compensation.

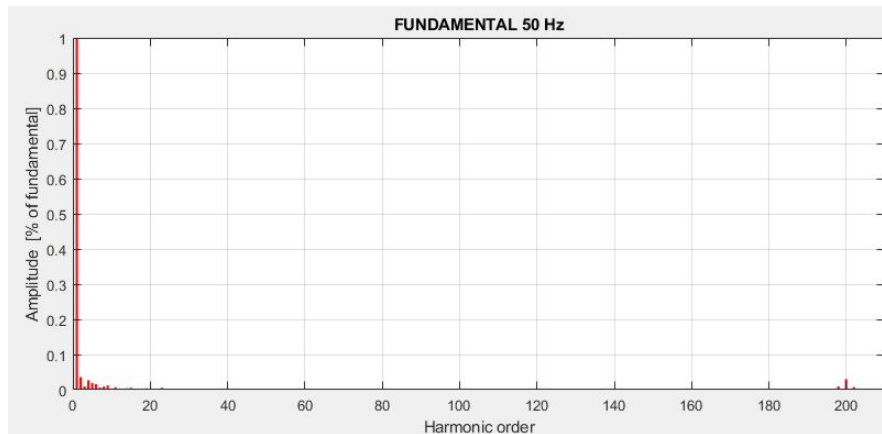


Fig. 11. Spectrum of absorbed current from the power supply (first 210 harmonics relative to the fundamental).

From this point of view, it would be desirable for the frequency of this generator to be as high as possible, but practically it is limited by the switching performance of the electronic devices in the rectifier bridge. Related to these performances, the efficiency of the converter that uses this carrier frequency in order to generate the PWM control pulses can be analysed.

2. The amplitude of the fundamental increased to the value $A_I = 6.65$ A, which is higher than in the case of the uncontrolled rectifier even if the RMS value of the supply voltage is 70,992 V, and THD is of about 0.03.

3. The value of the power factor is $PF = 0.99$, approaching considerably the unit.

IV. MODELING THE BOOST CONVERTER WITH PFC SYSTEM

The configuration shown in Fig. 4 can be considered a boost converter in a single stage (direct boost). In addition to the qualities highlighted by modeling and simulation, such a rectifier has the disadvantage of a number of four static controlled switches, which operate at a switching frequency much higher than the fundamental frequency. At medium and low powers, the switching losses of static switches do not greatly affect the efficiency of the converter. Instead, at high and very high powers, the switching losses begin to affect the efficiency of the converter. For this reason, two-stage PFC rectifiers, such as the boost converter, are preferred. It has a rectifier stage with uncontrolled power semiconductor devices (diode rectifier) followed by a stage with with a single controlled device that is part of the PFC structure (Fig. 5). Thus, instead of four high frequency switching controlled contactors, there is a single high frequency switching controlled contactor. In this way, the switching losses will be reduced by about a quarter compared to the first case.

For the implementation of the scalar method in this case, two reaction loops are used as in the previous case: a reaction loop according to the output voltage and a reaction loop according to the current absorbed from the power supply.

PFCs with the implementation of feedback loops are used to ensure stable operation and acceptable dynamic behavior, regardless of the load variation mode [3].

The scalar control method according to the average value of the current leads to a better waveform of the

absorbed current. The current error amplifier used in Fig. 12 filters the measured rectified current. The output of this error amplifier controls the PWM modulator. The current loop tends to reduce the error between the mean value of the rectified current I_r , and its reference.

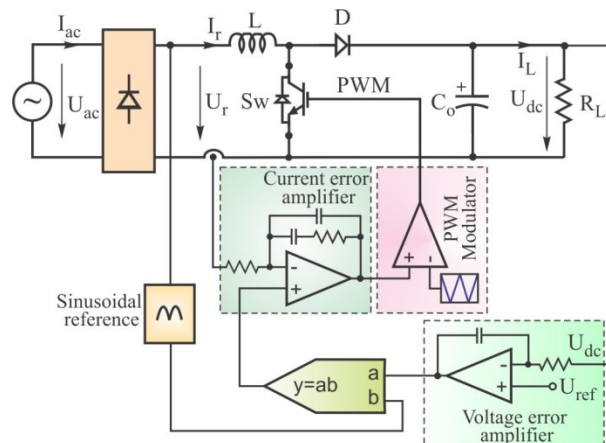


Fig. 12. Block diagram of the PFC boost converter controlled by the average current value ([3]).

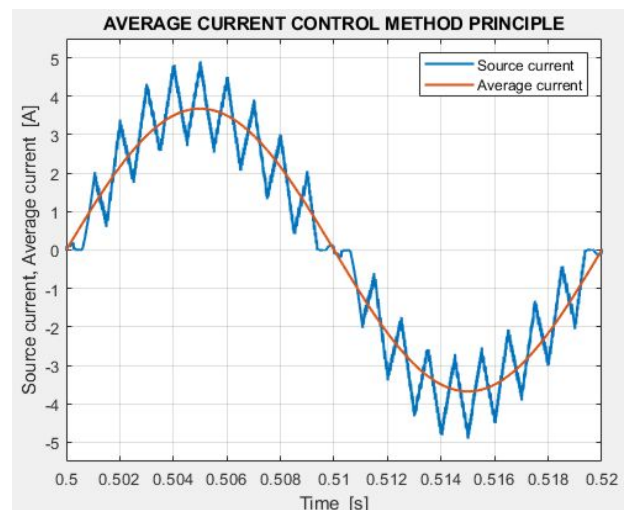


Fig. 13. Waveforms for control by average current value.

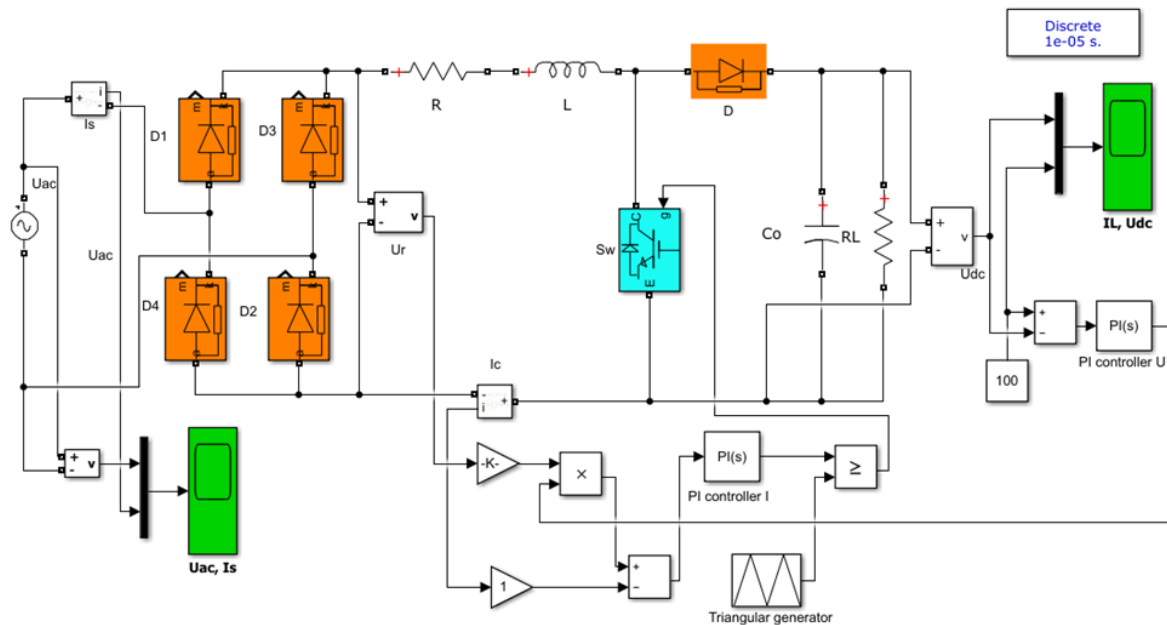


Fig. 14. The Matlab / Simulink model of the circuit shown in Fig. 5. The average current control method avoids the complications of the peak current control method by using a high gain integrative amplifier in the current feedback loop [3].

The waveforms illustrating the application of this method can be seen in Fig. 13.

The method has the following important advantages [3]:

- The switching frequency is constant;
- It does not require compensation ramp;
- There is lower sensitivity to telecommunication noises, due to current filtering.

In addition to these advantages, the method also highlights some disadvantages, such as [3]:

- The need to measure the current flowing through the inductance L ;
- It is necessary to use a current amplifier, whose compensation circuit must be designed so as to take into account the operating conditions of the converter.

For the study of the configuration of the PFC boost converter controlled by the average current method, the Matlab / Simulink model of the circuit in Fig. 5 has been conceived. The structure of this model is presented in Fig. 14.

The parameters for which the study was done by simulation on the above model of this PFC boost converter are: $U_{ac} = 40$ V (RMS), $L = 3$ mH, $C_o = 10,000$ μ F, $U_{ref} = 100$ V, $R_L = 100$ Ω . The resistor R in the model is the ohmic resistance of the inductance L . The frequency of the triangular wave generator is $f_{tr} = 10$ kHz. With these parameters, the shape of the current absorbed from the power supply is shown in Fig. 15.

Following the Fourier analysis of this current, it was possible to graphically represent the harmonic spectrum of this current, which is presented in Fig. 16.

The amplitude of the fundamental is, in this case, $A_1 = 3.714$ A. Harmonics of order higher than 50 are insignificant, up to around 200, a value that corresponds to the triangular carrier frequency (10 kHz).

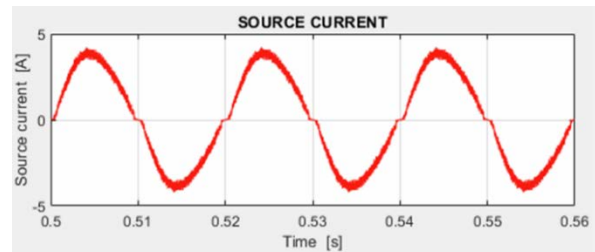


Fig. 15. The evolution over time of the current absorbed from the power supply by the PFC boost converter.

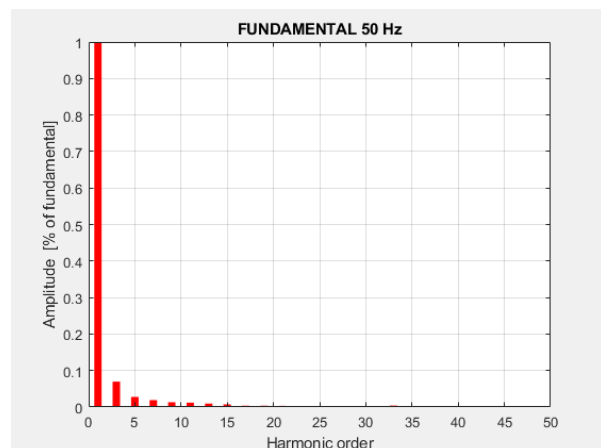


Fig. 16. Harmonic spectrum of the current in Fig. 15.

Following the simulation study on the model in Fig. 14, the following values were determined: $PF = 0.9925$ and $THD = 0.095$. The higher THD factor value in this case is explained by the fact that the amplitude of the higher order harmonics is higher in the case of the boost converter, compared to the direct converter.

In order to highlight the importance of tuning the reaction loops, Fig. 17 illustrates the voltage U_{dc} obtained

at the output of the rectifier, in comparison with the imposed reference voltage.

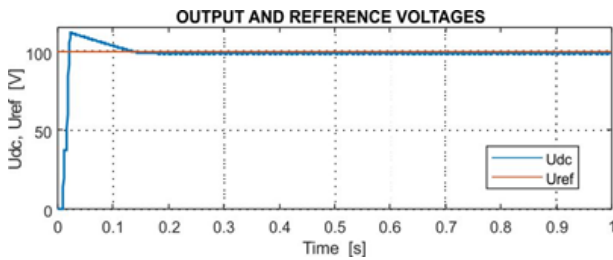


Fig. 17. U_{dc} and U_{ref} voltages.

According to this figure, the parameters of the feedback loops also determine the duration of the transient regime of the output voltage until reaching the prescribed value (in this case, the duration of the transient regime is about 0.15 s). During this transient regime, the output voltage is higher than the prescribed value.

V. CONCLUSION

The comparative results of the study of the scalar control techniques applied to the single-phase rectifiers provided with PFC structures, can be summarized in Table I.

TABLE I
COMPARISON BETWEEN DIFFERENT PARAMETERS

	Power Factor	THD	Current shape
Single Phase rectifier without PFC control	0.445	1.614	Pulsating
Single Phase full bridge PFC controlled	0.99	0.03	Sinusoidal
Single phase boost PFC controlled rectifier	0.9925	0.095	Sinusoidal

By applying scalar control methods for power factor correction, it is possible for the value of the power factor to approach the unit, and in cases where the feedback loops are designed correctly, it can even reach the value of 1. Both scalar control variants are relatively simple to be implemented.

The first variant does not require the measurement of the input voltage U_{ac} , it requires the measurement of only the current flowing through the inductance of the power supply. The control method can also be applied to three-phase rectifiers. Following the study on the model, it was found that the method has the disadvantage of a certain degree of instability in various operating conditions.

The second method of scalar control, applied to a classic boost converter structure has the advantage of better stability when changing the operating parameters (especially the load value), of adjusting the U_{dc} output voltage level according to the prescribed reference values, a spectrum of harmonics and a power factor comparable to those obtained by using the first method.

The disadvantage of implementing the second method is that the input voltage and current values in the boost converter circuit must be measured.

These drawbacks are offset by the fact that the switching losses of static switch are lower than in the first case, because instead of four contactors (which make up the rectifier bridge), only one switching device is used, the one that belongs to the boost structure, that is to the second stage of the converter.

Source of research funding in this article: Research program of the Electrical Engineering Department financed by the University of Craiova.

Received on July 09, 2020

Editorial Approval on November 19, 2020

REFERENCES

- [1] K. Jezernik, "Power control strategy for unity power factor," *2010 IEEE International Symposium on Industrial Electronics*, Bari, 2010, pp. 998-1003, doi: 10.1109/ISIE.2010.5636952.
- [2] A.G. Vishal Anand, Neeraj Gupta, V. Rammarayanan, "Unity power factor rectifier using scalar control technique," *International Conference on Power System Technology - POWERCON 2004*, Singapore 21-24 November 2004.
- [3] L.Rossetto, G.Spiazzi, P.Tenti, "Control techniques for power factor correction converters," *Proc. PEMC'94-9*.
- [4] M. Mahesh, "Performance improvement of ac-dc power factor correction converters for distributed power system," *Thesis, Degree of Doctor of Philosophy Under the supervision of Prof. Anup Kumar Panda, NIT, Rourkela*, Oct 2011.
- [5] W. Cheng, J. Song, H. Li and Y. Guo, "Time-varying compensation for peak current-controlled PFC boost converter," *IEEE Transactions on Power Electronics*, vol. 30, no. 6, pp. 3431-3437, 2015.
- [6] F. Musavi, M. Edington, W. Eberle and W. Dunford, "Control loop design for a PFC boost converter with ripple steering," *IEEE Transactions on Industry Applications*, vol. 49, no. 1, pp. 118-126, 2013.
- [7] K. Mahmud and Lei Tao, "Power factor correction by PFC boost topology using average current control method," *2013 IEEE Global High Tech Congress on Electronics*, 2013.
- [8] G.M. Samarth, D. Bhanabhagvanwala, "PFC boost topology using average current control method," *International Journal of Innovative and Emerging Research in Engineering*, Volume 3, Issue 5, 2016.